Improving radar interferometry for monitoring fault-related surface deformation

Miguel Caro Cuenca

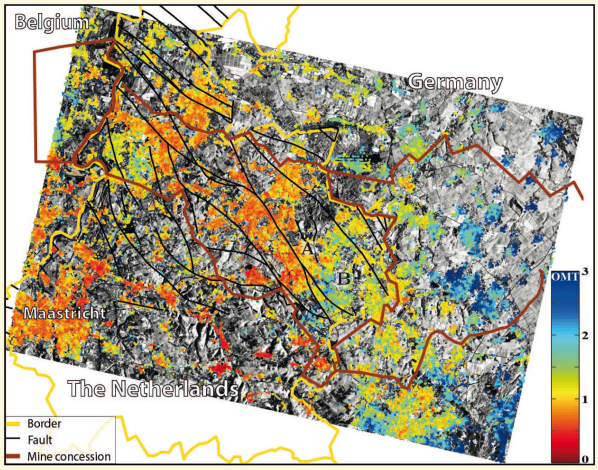

NCG KNAW

Nederlandse Commissie voor Geodesie Netherlands Geodetic Commission 81

Improving radar interferometry for
monitoring fault-related surface deformation

Improving radar interferometry for monitoring fault-related surface deformation

Applications for the Roer Valley Graben and coal mine induced displacements in the southern Netherlands

Miguel Caro Cuenca

Publications on Geodesy 81

NCG Nederlandse Commissie voor Geodesie Netherlands Geodetic Commission

Delft, January 2013

Improving radar interferometry for monitoring fault-related surface deformation. Applications for the Roer Valley Graben and coal mine induced displacements in the southern Netherlands
Miguel Caro Cuenca
Publications on Geodesy 81
ISBN: 978 90 6132 341 9
ISSN 0165 1706

Published by: NCG, Nederlandse Commissie voor Geodesie, Netherlands Geodetic Commission, Delft, the Netherlands

NCG, Nederlandse Commissie voor Geodesie, Netherlands Geodetic Commission
P.O. Box 5030, 2600 GA Delft, the Netherlands
T: +31 (0)15 278 21 03
F: +31 (0)15 278 17 75
E: info@ncg.knaw.nl
W: www.ncg.knaw.nl

The NCG, Nederlandse Commissie voor Geodesie, Netherlands Geodetic Commission is part of the Royal Netherlands Academy of Arts and Sciences (KNAW).

To my wife Indira, and my daughters Lucía and Sonia

In memory of my grandparents

Contents

Preface iii

Acknowledgements v

Summary vii

Samenvatting (summary in Dutch) x

Nomenclature xi

1 Introduction 1

1.1 Background and motivation 1

1.2 Research Objectives 2

1.3 Thesis Roadmap 4

2 Ground Deformation in the Southern Netherlands 5

2.1 Introduction 5

2.2 The Roer Valley Rift System 5

2.3 The Dutch coal mine industry and its effect on surface deformation 13

2.4 Summary 21

3 Time Series InSAR Analysis: The Persistent Scatterer Interferometry Approach 23

3.1 Introduction 23

3.2 InSAR principles 23

3.3 Overview of Persistent Scatterer Interferometry (PSI) 33

3.4 DePSI 35

3.5 Phase unwrapping 41

3.6 Potential improvements to the reference technique 48

4 Improvements to Persistent Scatterer Interferometry 49
4.1 Introduction . . . 49
4.2 Improvements to PSI algorithms . . . 49
4.3 Improvements specific to the reference technique, DePSI . . . 66
4.4 Long term processes monitoring with PSI . . . 70
4.5 Summary and conclusions . . . 74

5 Surface Deformation in the Roer Valley Rift System Observed by PSI 77
5.1 Introduction . . . 77
5.2 Rates in the Roer Valley Rift System area estimated with PSI . . . 78
5.3 Ground water levels variations as a cause for surface displacements in the Roer Valley Graben . . . 89
5.4 Fault mapping from rate estimations . . . 90
5.5 Summary and conclusions . . . 93

6 Surface Deformation in the Dutch Coal Field Observed by PSI 97
6.1 Introduction . . . 97
6.2 Surface displacements observed by PSI . . . 99
6.3 Spatio-temporal evolution of mine water recharge from surface displacements 107
6.4 Model of underground volume change . . . 108
6.5 Summary and conclusions . . . 111

7 Conclusions and Recommendations 115
7.1 Scientific contribution . . . 115
7.2 Recommendations . . . 118

A Used software tools 121

B Used SAR data 123

About the Author 139

Index 141

Preface

This book summarizes five years work that focused on the study and use of radar interferometry (InSAR) to monitor fault-related displacements in the southern Netherlands. I have tried to compile a self-contained book in the sense that it does not only describe the contributions of this research but also provides with background information on the areas where the contribution may be considered of scientific interest. Hence, when describing surface processes affecting the southern Netherlands, namely tectonic motion in the Roer Valley Graben and mine-abandonment, I put spatial emphasis on the scientific areas where InSAR could contribute the most. On the one hand, I compiled different studied that estimated slip rates in the Roer Valley Graben with the intention to show discrepancies between short time and geological time scales estimates. On the other, I attempted to highlight the complexity of the deformation signal affecting the mines of south Limburg and the difficulty of monitoring such signal with current geodetic techniques.

Since my personal interest were also inclined towards the technique itself, InSAR, I focused on describing it along with its time series application. I used the algorithm that had been previously developed in the Delft University of Technology known as DePSI (or Delft implementation of Persistent Scatterer Interferometry). At the moment when I arrived to Delft (2006), the technique was already in a mature state and had been applied with excellent results to study different phenomena, e.g., gas production in the Netherlands. However, I decided to study it in-depth aiming at detecting potential areas of optimization. For example, I examined the causes that made DePSI to reject pixels that were in principle very stable. One of the causes was a non-optimal solution space that was needed for phase unwrapping and built based on prior knowledge. The solution space needed to be optimized. This idea brought me to produce a new algorithm for phase unwrapping. With this work, I hope to have contributed to improve InSAR time series techniques and to have provided with a new perspective on surface displacements in the southern Netherlands.

Prospective Audience

This book is intended to be of some value for two different group of readers. On the one hand, students, engineers and scientist with interest on time series InSAR techniques, and may wish to learn more about these methods or even develop their own software. On the other, scientists who wish to apply time series InSAR to study fault-related motion. These last group includes hydrologists, geologists, geodesists and geophysicists.

Acknowledgements

I owe a great debt to many persons who helped during my PhD. First of all I would like to thank my promotor Prof. dr. ir. Ramon Hanssen for his supervision. I have greatly benefit from his meticulous view and sharp comments. Working with him has improved my skills enormously.

I thank very much Dr. Andrew Hooper for his generosity in sharing his knowledge. I had the opportunity to discuss with him many of the ideas of this research and always received a very valuable feed-back.

I would like to thank Mahmut Arikan, for his friendship and his inexhaustible energy to help me in different technical subjects. I am also very thankful to Sami Samiei-Esfahany. With Sami, I always had interesting discussions not only on my research but many other topics. We expended very fruitful hours of conversation in front of a white board.

I appreciated very much the team-spirit of Joana Esteves Martins, Pooja Mahapatra, Prabu Dheenthayalan, Ling Chang, Manu Delgado Blasco, Qiang Wang and Anneleen Oyen (Anneleen also helped me with the Dutch translation). Together they created a very enjoyable working environment.

There is also a very long list of (former) colleagues to whom I am very thankful : Dr. Liu Guang, Gertjan van Zwieten, Freek van Leijen, Dr. Gini Ketelaar, Dr. Zbigniew Perski, David Bekaert, Shizhuo Liu, Petar Marinkovic, Peter Buist, Peter de Bakker, Dr. Gabrielle Giorgi, Dr. ir. AliReza Amiri-Simkooei, Dr. ir. Sandra Verhagen, Dr. ir. Hans van der Marel, Dr. Christian Tiberius and Prof. dr. ir. Peter Teunnisen . I am also very thankful to all members of my defense committee, the manuscript of this book has definitely improved with their valuable comments.

I appreciated very much the excellent administrative work of Ria Scholtes, Rebeca Domingo, File Koot-Stomp, Danko Roozemond and Lidwien de Jong.

I am also thankful to my friends outside work with whom I enjoyed very much my free time: Luís, Tatiana, Carlos, Maurys, Érika and Eduardo.

I would like to express my sincerest gratitude to my parents and brothers and sisters in Spain: Ascensión, Miguel, Jesús, María del Mar, María Teresa and Rocío, for their love and support. I also express my deepest appreciation to my family-in-law in Venezuela and Australia.

Most of all I would like to thank my wife, Indira, for her understanding and love during the past few years. Her support and encouragement was in the end what made this dissertation possible. To my daughters, Lucía and Sonia, with all their love they make me so happy.

Summary

Improving radar interferometry for monitoring fault-related surface deformation

Applications for the Roer Valley Graben and coal mine induced displacements in the southern Netherlands

Radar interferometry (InSAR) is a valuable tool to measure surface motion. Applying time series techniques such as Persistent Scatterer Interferometry (PSI), InSAR is able to provide surface displacements maps with mm-precision. However, InSAR can still be further optimized, e.g. by exploiting spatial characteristics of the signal of interest. This study addresses surface deformation associated with geological faults. In principle, this signal is generally spatially smooth but with significant-to-large gradients at fault locations.

We first focus on optimizing InSAR time series analysis, in particular the PSI method, for this specific class of ground deformation processes. Secondly, we apply the improved technique to study fault-related motion in the southern Netherlands, with special interest in detecting neotectonic motion in the Roer Valley Graben and deformation in the abandoned mines of South Limburg.

The proposed optimization adapts PSI to analyze in an iterative manner the signal of interest to estimate spatially the probability density function of displacements. Since the signal is expected to change quickly near faults, we do not restrict this distribution to be unimodal but we allow it to have any shape. Finally, we use the determined distribution to constrain, through Bayesian inference, phase unwrapping (the operation of unfolding the phase outside its natural range of $(-\pi, \pi]$ radians). We demonstrate a substantial benefit of the Bayesian approach as we show a decrease in the number of unwrapping errors. This thesis also suggests a method that analyzes interferometric phases to estimate noise variance. It is built upon the assumption that coherence can be spatially correlated. The estimated stochastic parameters are used in phase unwrapping by assigning lower weights to noisy observations.

The improved methodology is applied to study fault-related motion in the southern Netherlands, exploiting data from three satellite missions: ERS-1, ERS-2 and Envisat. In particular, we focus on two main areas: the Roer Valley Graben and the abandoned mines of south Limburg.

In the Roer Valley Graben area, a deformation signal associated with geological faults is detected. However, we do not observe any significant indication to atribute a tectonic origin to this signal for two main reasons. First, during large part of the studied period the most of the graben uplifts with respect to adjacent horsts at rates of $\sim$1 mm/yr, behaving

opposite to predicted by tectonics. Second, the deformation signal in this area appears to be largely related to water pumping. For example, we observe an uplift signal of about +4 mm/yr that matches in time and space with the cease of pumping in the Erkelenz Coal District, which is located in the Peel horst, adjacent to the Roer Valley Graben.

Concerning the mines of South Limburg, we detect strong surface displacements (uplift) which appear to be centered on the old mines and constrained by tectonic faults. The signal is variable in space and time, with uplift rates up to 20 cm in 18 years, and relatively large gradients across faults ($\sim$5 cm/km), in the same time span. Laterally the uplift signal propagates towards the west in this period. The comparison of surface displacements with rising groundwater levels reveal a strong correlation between the two, suggesting the groundwater to be the cause of the uplift.

Assuming that rising ground water levels in the abandoned mines are responsible for the uplift, we estimate the relation between the groundwater and the associated uplift. The skeletal storage coefficient, which directly depends on porosity, is on average $0.5 \pm 0.1 \cdot 10^{-3}$, implying that 1 m of water level increase produces 0.5 mm uplift. As we expect that the water may rise many tens of meters, especially in the western side, this may result in several additional centimeters of future uplift.

Essentially, the surface displacements that we observe in the southern Netherlands seem to be mainly caused by fluctuations in groundwater flow, which appear to be constrained by faults.

Samenvatting (Summary in Dutch)

Verbetering van radar interferometrie voor het inspecteren van breukgebonden bodembewegingen

Toepassing op de Roerdalslenk en koolmijngerelateerde deformaties in Zuid-Nederland

Radar interferometrie (InSAR) is een erkende techniek voor het meten van bewegingen van het aardoppervlak. Door het toepassen van tijdreekstechnieken zoals Persistent Scatterer Interferometrie (PSI) is het mogelijk door middel van InSAR bodembewegingen tot op de millimeter nauwkeurig in kaart te brengen. Maar InSAR kan nog verder worden geoptimaliseerd door onder meer het onderzoeken van de ruimtelijke eigenschappen van het signaal. Deze studie onderzoekt de vervormingen van het aardoppervlak gerelateerd aan geologische breuklijnen. Over het algemeen is dit signaal ruimtelijk heel vlak maar kan significante tot grote gradienten bevatten op de locaties van de breuklijnen. We richten ons eerst op het optimaliseren van de InSAR tijdreeksanalyse, met in het bijzonder de PSI methode, toegepast op deze soort van bodembeweging. Vervolgens passen we de verbeterde techniek toe voor het onderzoeken van breuklijngebonden bewegingen in het zuiden van Nederland, met in het bijzonder het detecteren van neotektonische bewegingen in de Roerdalslenk en vervormingen in de voormalige mijngebieden van Zuid-Limburg. De optimalisatie die hier wordt voorgesteld past de PSI methode zodanig aan dat het signaal op een iteratieve manier wordt geanalyseerd om de kansdichtheid van de deformaties te schatten. Aangezien we verwachten dat het signaal sterk varieert in de nabijheid van een breuklijn, gaan we de kansverdeling niet beperken tot een unimodale verdeling maar staan we elke kansverdeling toe. Uiteindelijk gebruiken we de nieuwe kansverdeling om de phase unwrapping (het als het ware ontvouwen van de fractionele fase buiten zijn natuurlijke marges van $(\pi, \pi]$ radialen) te beheersen door middel van Bayesiaanse interferentie. We tonen een essentieel voordeel van de Bayesiaanse benadering aan met een daling van het aantal fouten in de phase unwrapping. In deze thesis wordt ook een methode voorgesteld die de interferometrische fase analiseert om de variatie in de ruis te schatten. De geschatte stochastische parameters worden gebruikt in de phase unwrapping door het toewijzen van een lagere weegfactor aan waarnemingen met veel ruis. De aangepaste methode is toegepast om de breuklijngebonden bodembewegingen in het zuiden van Nederland te onderzoeken. Er wordt data van drie satellietmissies gebruikt: ERS-1, ERS-2, en Envisat. We concentreren ons hoofdzakelijk op twee gebieden: de Roerdalslenk en de voormalige mijngebieden van Zuid-Limburg.

In de Roerdalslenk detecteren we bodembewegingen in de nabijheid van geologische breuklijnen. Hiervoor kan echter geen significante verklaring gevonden worden in de tektoniek

omwille van twee redenen. Ten eerste, gedurende een groot deel van de bestudeerde periode stijgt het merendeel van de slenken ten opzichte van de horsten met een snelheid van $\sim$1 mm/jaar, wat het tegenovergestelde is van wat voorspeld wordt door de tektoniek. Ten tweede is de bodembeweging in dit gebied erg gerelateerd aan het pompen van grondwater. Zo observeren we bijvoorbeeld een bodemstijging van 4 mm/jaar die zowel in tijd als ruimte overkeenkomt met het staken van grondwater pompactiviteiten in het Erkelenz koolmijngebied, dat gelegen is op de Peelhorst naast de Roerdalslenk. Betreffende de mijnen in Zuid-Limburg detecteren we sterke bodemstijgingen midden op de oude mijnschachten. Opmerkelijk is dat de bodemstijging stopt aan de tektonische breuklijnen. Het signaal varieert tot een maximum van 20 cm in een tijdsspanne van 18 jaren met relatief grote gradienten over de breuklijnen ($\sim$5 cm/km). We ontdekken ook dat tijdens deze periode de bodemstijging westwaards migreerde. Als we vervolgens de bodembewegingen vergelijken met het stijgende grondwaterpeil, vinden we een sterke overeenkomst tussen beiden, wat er sterk op wijst dat het grondwater de bodemstijging veroorzaakt. Als we aannemen dat het stijgende grondwaterpeil in de verlaten mijngangen en -schachten verantwoordelijk is voor de bodemstijging, kunnen we de relatie tussen het grondwater en de bodemstijging schatten. De opslagcoefficient, die afhankelijk is van de porositeit, heeft gemiddelde een waarde van $0.5 \pm 0.1\dot{1}0^3$, wat betekent dat een stijging van het waterpeil van 1 m resulteert in een bodemstijging van 0.5 mm. Aangezien het water enkele tientallen meters kan stijgen, voornamelijk in de westkant, kan dit leiden tot een bodemstijging van enkele centimeters. Over het algemeen kunnen de bodembewegingen in het zuiden van Nederland verklaard worden door schommelingen in de stroming van het grondwater gebonden aan de ligging van de breuken.

Nomenclature

List of acronyms

APS	Atmospheric Phase Screen
BLUE	Best Linear Unbiased Estimation
CB	Campine Block
cdf	Cumulative Density Function
DEM	Digital Elevation Model
DePSI	Delft implementation of PSI
DIA	Detection, Identification and Adaptation
Envisat	ENVironment SATellite
ERS1/2	European Remote Sensing Satellite 1 and 2
ESA	European Space Agency
FFZ	Feldbiss Fault Zone
GPS	Global Positioning System
InSAR	SAR INterferometry
LAMBDA	Least-squares AMBiguity Decorrelation Adjustment
LOS	Line Of Sight
NSC	Non-Spatially Correlated (signal)
OMT	Overall Model Test
PB	Peel Block
PBFZ	Peel Boundary Fault Zone
pdf	Probability Density Function
PS	Persistent Scatterer
PSI	Persistent Scatterer Interferometry
RMS	Root Mean Square
ROB	Royal Observatory of Belgium
RVG	Roer Valley Graben
RVRS	Roer Valley Rift System
SAR	Synthetic Aperture Radar
SB	Small Baseline
SCR	Signal to Clutter Ratio
SLC	Single Look Complex
SRTM	Shuttle Radar Topography Mission

STC	Spatio-Temporal Consistency
STUN	Spatio-Temporal Unwrapping Network (algorithm)
TanDEM-X	TerraSAR-X add-on for Digital Elevation Measurement
TerraSAR-X	German radar satellite
TFZ	Tegelen Fault Zone
UTC	Coordinated Universal Time
vc	Variance-Covariance (Matrix)
VCE	Variance-Covariance Estimation
VG	Venlo Graben

List of symbols

cm	centimeter
Hz	Hertz
km	kilometer
m	meter
mm	millimeter
rad	radians
yr	year

$\hat{.}$	Estimated value
$\mathbb{W}\{.\}$	Wrapping operation
$\sum$	Sum
$\{.\}^{-1}$	Inversion
$\{.\}^{T}$	Transposition
$\{.\}_{lk}$	Arc spanning PS l and k
$D\{.\}$	Dispersion
$E\{.\}$	Expectation

α	Level of significance for statistical test, (also used to denote angle determining the slave position w.r.t to master)
$\breve{a}$	Estimated ambiguities
$\breve{z}$	Estimated decorrelated ambiguities
χ^2	Bound of the search space for integer least-squares method
A	Design matrix
a_{lk}^{i}	Ambiguity of arc lk in interferogram i
a_{lk}	Ambiguity vector of arc lk
B	Design matrix for the temporal model when ambiguities are included,(also used to denote baseline)
$k_{\frac{\alpha}{2}}$	Critical value for a double tailed distribution and level of significance α

Q_x	Variance-Covariance matrix of the unknowns
Q_y	Variance-Covariance matrix of the observations
$Q_{\check{z}}$	Variance-Covariance matrix of $\check{z}$
$Q_{\check{a}}$	Variance-Covariance matrix of $\check{a}$
R_y	Cofactor matrix
u	Number of unknowns
x	Unknowns
y	Observations
Z	Decorrelating matrix
z	Z-transformed ambiguity

Φ	Unwrapped interferometric phase
ϕ	Wrapped interferometric phase
ϕ_k^i	Wrapped interferometric phase of PS k in interferogram i
$\phi^i_{\text{filtered},k}$	Wrapped interferometric phase of PS k in interferogram i filtered in space
$\phi^i_{\text{noise},k}$	Noise phase of PS k in interferogram i
ϕ^i_{lk}	Wrapped interferometric phase of arc lk in interferogram i
Φ_{atm}	Unwrapped interferometric phase caused by atmospheric delay difference
Φ_{defo}	Unwrapped interferometric phase caused by ground motion
Φ_{noise}	Unwrapped interferometric phase caused by noise
Φ_{orb}	Unwrapped interferometric phase shift due to orbital inaccuracies
Φ_{ref}	Unwrapped interferometric phase contribution of a reference body
Φ_{scat}	Unwrapped interferometric phase due to a change in the scattering properties
Φ_{subpx}	Unwrapped interferometric phase produced by a difference in location between the assumed phase center and the real phase center
Φ_{topo}	Unwrapped interferometric phase contribution of topography

D_{season}	Amplitude of a seasonal signal
ΔV	Volume change in a strain source
Δh_{water}	Water level change
Δp	Pressure change in a strain source
ΔV_0	Maximum volume change of a strain source
Δz	Vertical expansion of the rock
ν	Poisson's ratio
D	Depth of strain source
D_i	Coefficients describing a seasonal signal with $i = 1, 2$
dp	Differential pressure change in a strain source

dz	Change in the vertical dimension of a strain source
H	Initial height (size in the vertical direction) of a strain source
p	Pressure in a strain source
$p(r,t)$	Pore pressure distribution at time t and at radial distance r from location of maximum pore pressure change
R	Radial distance to the strain source
r	Radial distance r from location of maximum pore pressure change
r_c	Characteristic radius of the reservoir
S_{area}	Horizontal extension (with length dimensions) of a strain source
S_{ke}	Storage coefficient
V	Initial volume of a strain source

f_{DC}	Doppler centroid
α	Angle determining the slave position w.r.t to master,(also used to denote level of significance for statistical test)
Δf_{DC}	Doppler centroid difference
Δh_{lk}	Residual topographic difference between PS l and PS k
Δy	Offset between two time series
η	Subpixel position in range
γ	Phase coherence
γ_{lk}	Phase coherence of arc lk
λ	Wavelength
τ	Period of a seasonal signal
θ	Look angle
θ^o	Look angle for the reference body
θ_{h}	Satellite heading
θ_{s}	Squint angle
θ_i	Local incidence angle
ξ	Subpixel position in azimuth
A_{MS}	Interferogram amplitude
B	Baseline, (also used to denote a design matrix)
$B^i_{\parallel}$	Parallel baseline for interferogram i
$B^i_{\perp}$	Perpendicular baseline for interferogram i
B^i_{temp}	Temporal baseline of interferogram i
$B^o_{\parallel}$	Parallel baseline for the reference body
$B^o_{\perp}$	Perpendicular baseline for the reference body
$B_{\parallel}$	Parallel baseline
$B_{\perp}$	Perpendicular baseline
B_{temp}	Temporal baseline
c_{lk}	Constant factor affecting time series of arc lk also referred to as master atmosphere

d	Displacement; vector of parameters describing displacement behavior in time
D_A	Amplitude dispersion
d_E	East components of displacement vector
d_N	North components of displacement vector
d_{total}	Vector of total displacement
d_U	Up components of displacement vector
e	Vector of residuals
e_{lk}^i	Residual for arc lk in interferogram i
$f(t)$	Function describing displacements as a function of time t
h	Height
$h_{2\pi}$	Height ambiguity
$h_{\mathrm{NSC},k}$	Non-spatially correlated heights of PS k w.r.t its surroundings
h_k	Height difference PS k w.r.t it surroundings; height threshold used in indicator kriging
h_{lk}	Height difference between PS l and PS k
I	Interferogram
M	Master SLC image
N	Number of interferograms; number of observations
n_i	Number of PS inside block i
$N_{\mathrm{sat}i}$	Number of interferograms formed from the acquisition of satellite i
$PS_{\mathrm{sat}i}$	A set of PS detected by satellite i
$Q_{y_{\mathrm{sat}i}}$	Variance covariance matrix of observations $y_{\mathrm{sat}i}$
R_i	Distance between the position of the satellite in orbit i and a target on ground
S	Slave SLC image
t	Generic time variable
t_0	Temporal offset of a seasonal signal
t_i	Specific time i
$t_{\mathrm{sat}i}$	Vector of acquisition times for satellite i
v	Displacement rate
v_{sat}	Satellite velocity vector
$v_{\mathrm{block}i}$	Average displacement rates of PS inside block i
$v_{\mathrm{NSC},k}$	Non-spatially correlated rate of PS k w.r.t its surroundings
v_{lk}	Displacement rate difference between PS l and PS k
$y_{\mathrm{sat}i}$	Vector of observations of satellite i

$(\hat{\sigma}_k^i)^2$	Estimated variance of PS k
$(\hat{\sigma}_{\mathrm{space},k}^i)^2$	Spatial estimate of variance of PS k in interferogram i
$(\hat{\sigma}_{lk}^i)^2$	Estimated variance of arc lk
$\hat{\mu}_{\mathrm{noise},k}^i$	Sample mean of PS k in interferogram i calculated spatially
$\hat{\mu}_{\mathrm{noise},k}$	Sample mean of noise of PS k estimated over time

$\hat{\sigma}^2_{\text{time},k}$	Temporal estimate of variance of PS k
σ	Standard deviation
σ^2	Variance
$\sigma_{\text{block}i}$	Standard deviation of displacement rates of PS inside block i
σ^2_{lk}	Variance of arc lk
$\varsigma(X)$	cdf of parameter X
$\wp(X)$	pdf of parameter X
$I(p_0, h_w)$	Indicator of height threshold h_w at position p_0
p_0	Position
T_σ	Threshold for maximum variance difference to group PS that resemble each other

Chapter 1

Introduction

1.1 Background and motivation

In the last few decades, satellite radar interferometry (InSAR) (Massonnet et al., 1994; Bamler and Hartl, 1998; Hanssen, 2001), has evolved into a geodetic tool of recognized importance and widespread use. The initial limitations of the technique, namely decorrelation (noise caused by changes in the scattering mechanisms of a resolution cell and/or satellite viewing angle) and atmospheric signals, were overcome thanks to the development of interferometric time series methods in the late 1990's. Interferometric time series techniques are now able to provide surface displacements maps over vast areas at a high resolution and precision. Persistent scatterer interferometry (PSI) is one of the most relevant InSAR time series methods. The technique analyzes a stack of radar images to detect scattering objects that are not (or just slightly) affected by noise. These objects are known as persistent scatterers (PS), when their scattering properties do not change significantly with time and viewing angle. The low noise nature of PS facilitates posterior estimations. Likewise, atmospheric signals can also be reduced with a low-pass time filter, assuming atmospheric delays are not correlated in time.

The original PSI algorithm was proposed by Ferretti et al. (1999), building upon earlier studies (Usai, 1997; Usai and Hanssen, 1997) that recognized the value of long term coherent pixels.

PSI methods have evolved since then. The algorithms of Ferretti et al. (2001); Kampes (2006); Hooper (2006); Crosetto et al. (2008) and Ketelaar (2009) are some examples. Currently, the technique is applied to study a large variety of ground deformation phenomena that include, among others, volcanism (see, e.g., Hooper et al. (2007), Paganelli and Hooper (2008) and Sturkell et al. (2010)), water pumping (e.g., Bell et al. (2008) and Dehghani et al. (2009)), and gas extraction (e.g., Ketelaar (2009)).

This dissertation focuses to improve PSI to study land deformation that is associated to tectonic faults, with especial interest on Neotectonics and coal mine induced displacements in the southern Netherlands.

Neotectonic motion in the southern Netherlands is produced by the Roer Valley Rift System. Continuous seismicity, (several earthquakes of magnitude $\sim$5 have been recorded since 1932) and geomorphological studies (see, e.g., Michon and van Balen (2005)) prove that the Roer Valley Rift System is active. Despite being the focus of many different studies (see e.g., Houtgast and van Balen (2000); Vanneste and Verbeeck (2001); Michon and van Balen (2005); van Balen et al. (2005) and Demoulin (2006)), the rift behavior,

specially, slip rates, are still cause of debate. There exist large discrepancies between slip rates estimated at short (10-100 yr) and geological (10^5-10^6 yr) time scales. For example, leveling measurements whose results have covered the last few decades suggest a slip rate of ∼1 mm/yr (Groenewoud et al., 1991; Demoulin, 2006). Meanwhile, techniques that give an average rate over millions of years (e.g., trenching), estimate one, and even two, orders of magnitude lower (Vanneste and Verbeeck, 2001; Houtgast et al., 2003, 2005).
One of the major difficulties to analyze these differences resides in the limited extent and low density of observations provided by techniques applied to this area. PSI, which is able to provide with high density of observations over vast areas, is expected to bring a new insight to the deformation that occurred in the Roer Valley Rift System during the last two decades. Large coverage is needed to study this rift system not only because of its large dimensions (50×150 km^2) but also to better understand the influence of the proximate mining industry.

In fact, the mining industry can also have a significant impact on ground deformation. In the Netherlands, most of the coal mines are found in the province of Limburg, to the south of the Roer Valley Rift System. These coal fields were exploited throughout centuries until they closed in the 1970's. The long term extraction produced a subsidence of several meters (Pöttgens, 1985; Rosner, 2011). Currently, most of the mines are closed, but they can still produce surface displacements, albeit being abandoned. Pöttgens (1985) observed land uplift in the southern Netherlands after the mines were abandoned in 1974. He explained the displacements as being caused by pore pressure increase due to mine water rebound. In the Dutch coal field, surface displacements have been measured mostly with leveling. Although leveling is a well-established technique, it has the aforementioned disadvantages: its limited extent and low density of observations. Therefore, we also expect that for the case of mining induced motion, PSI will contribute to a better comprehension of this signal, e.g., the influence of near faults on the displacement field.

1.2 Research Objectives

This dissertation aims first at optimizing PSI methods to improve the precision of deformation estimations in order to mitigate the difficulties that we anticipate to have when studying fault-related displacements in the southern Netherlands. On the one hand, slip rates in the Roer Valley Rift System are expected to be low, i.e. in the order of 1 mm/yr or less. On the other, we presume that the mining industry has produced a complex deformation field in space and time due to the network of entangled galleries, which could be hard to be correctly estimated if common error sources (e.g. unwrapping errors) are not reduced.
Delft implementation of PSI, DePSI, is the reference technique used in this research. This algorithm is based on the Spatial Temporal Unwrapping Network (STUN) algorithm (Kampes, 2006); however extended by van Leijen et al. (2006) and Ketelaar (2009).

The optimized PSI algorithm will be used to study the neotectonic activity of the Roer Valley Rift System and the effect of the Dutch coal industry on surface deformation.

These objectives are formulated as the next research question:

- **How to improve PSI for an optimal study of fault-related motion and what do we learn from the application of the improved technique to the southern Netherlands concerning the Roer Valley Graben and the influence of the coal mine industry on surface deformation?**

For simplification, the initial research question is broken down in three parts. The first one concerns the optimization of the technique:

1. *How to optimize the PSI technique to study fault-related displacements?*

   As mentioned above, the signals of interest are complex to study. Reducing error sources of PSI techniques, namely, phase unwrapping errors, can therefore help to obtain more precise estimates. Due to its cyclical nature, phase is only known as the 2π-modulus of the absolute (or *unwrapped*) phase. The process of estimating the absolute phase from its wrapped value, is known as phase unwrapping. Errors in phase unwrapping are the most serious threat to surface displacements estimation. Other types of errors sources can also be mitigated. We will also explore the reference algorithm, DePSI, to study different areas of improvement concerning specifically this implementation. In this case, we plan to modify the algorithm workflow to optimize the estimation of spatially correlated noise, such as atmospheric delay and orbital errors, which can also hamper estimations. We also attempt to improve the density of PS that are reliable unwrapped, because we expect that high density of observations will aid to study the complexity of the deformation signals in the Dutch mining area. Finally, since the phenomena of interest last longer than satellite lifetime, we also examine a method for long term monitoring using PSI.

   In summary, the improvement of PSI techniques concerns the following bullet points,

   - Improving current phase unwrapping algorithms.
   - Optimization of the reference technique, DePSI, namely the algorithm workflow to improve both, estimation of spatially correlated noise and the density of reliable observations.
   - Developing a method for applying PSI for long term monitoring.

2. *What do we learn about the Roer Valley Rift System from the displacements measured by PSI?*

   The second subquestion relates to the tectonic motion of the southern Netherlands. In this case, we aim specifically at

   - Estimating deformation rates in the Roer Valley Rift System area.
   - Analyzing the observed deformation with the goal of understanding the driving mechanism(s) governing this signal.
   - Analyzing the cause of the differences between the slip rates measured at short (10-100 yr) and geological time scales.
   - Analyzing the added value of PSI when applied to study the Roer Valley Rift System.

3. *What do we learn about the influence of coal mine industry in surface deformation in the southern Netherlands from the displacements measured by PSI?*

   The third subquestion relates to the Dutch coal mine industry and how it affects surface deformation in the southern Netherlands. In this case, we focus on the following:

   - The estimation of total surface deformation in the Dutch coal field for the period 1992-2010.
   - The analysis of the causes of the observed deformation.

- The spatio-temporal evolution of the observed signal, describing the influence of tectonic faults on the deformation field.
- The added value of PSI when applied to monitoring the Dutch coal field.

1.3 Thesis Roadmap

The current chapter states the motivation and the goals of this study.
Chapter 2 is dedicated to the ground dynamics of the area of interest. It describes the phenomena of interest, namely tectonic motion and mining industry in the southern Netherlands.
Chapter 3 provides an overview of existing PSI methods with special attention to the DePSI implementation.
Chapter 4 is primarily concerned with the major limitations of the current PSI algorithms and investigates how to overcome them, taking into that our phenomena of interest are tectonic motion and displacement caused by the mining industry.

Chapter 5 describes and analyzes the motion detected by PSI in the Roer Valley Rift System area.
Chapter 6 discusses the results of applying PSI to the abandoned coal mines in south Limburg.
Finally, chapter 7 summarizes the most important findings and conclusions of this research. It also provides suggestions for future work.

Chapter 2

Ground Deformation in the Southern Netherlands

2.1 Introduction

The application of radar interferometry (InSAR) to study fault-related motion in the southern Netherlands is one of the major goals of this thesis. In particular, we have special interest in detecting neotectonic motion in the Roer Valley Graben and deformation in the abandoned mines of South Limburg.

This chapter is dedicated to describe these mechanisms of land deformation. Section 2.2 gives an overview of the tectonic setting of the Roer Valley Rift System. Especial attention is paid to slip rates that were estimated in previous studies, because of the high discrepancies between estimations. The differences can reach one or two orders of magnitude. We explore the benefits of applying InSAR time series analysis to the Roer Valley Rift System in section 2.2.3.
Section 2.3 summarizes the effect of the coal extraction on surface deformation in the southern Netherlands. We focus on the consequences of its abandonment. In this case, we also comment on the expected benefits of using InSAR to study this area in section 2.3.3.

2.2 The Roer Valley Rift System

The Roer Valley Rift System is located in the southern Netherlands, in a NW-SE orientation with a total extent of about 50×150 km^2, see fig. 2.1 (Zijerveld et al., 1992; Houtgast and van Balen, 2000; Michon et al., 2003; Houtgast et al., 2005; van Balen et al., 2005).
Neotectonics—the current tectonic period—in the Roer Valley Rift System started in the late Early Miocene ($\sim$20 Myr ago) and is expressed as extension of the rift in NE-SW direction (Ziegler, 1992; Houtgast and van Balen, 2000; van Balen et al., 2005; Cloetingh et al., 2005). Neotectonic faulting mode of the rift system is (nearly) normal, which is in agreement with the direction of the rift extension (van Balen et al., 2005).

The Roer Valley Rift System consists primarily of three distinct parts, see fig. 2.1. The Peel and the Campine blocks located respectively north and south of the Roer Valley Graben, which is the main subsiding structure. Then, the principal faults systems are the Peel Boundary Fault Zone and the Feldbiss Fault Zone, which separate respectively the Peel Block and the Campine Block from the Roer Valley Graben. Apart from these structures, we also find the Venlo Graben located north and separated from the Peel Block by the

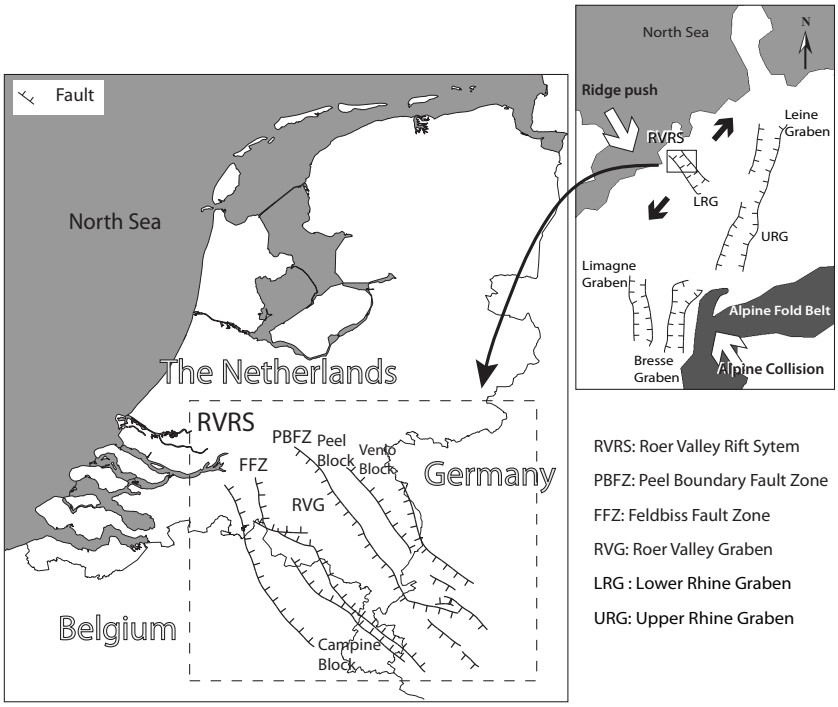

Fig. 2.1. Tectonic setting of Roer Valley Rift System as a part of the Cenozoic mega-rift System and main forces related to the extension of the rift, after Ziegler (1992) and Houtgast et al. (2003). The extension of the Roer Valley Rift System is explained by the NW-SE compression related to the Alpine collision and the North Atlantic ridge push (Gölke et al., 1996; Michon et al., 2003; Dezes et al., 2004).

Tegelen Fault Zone (Michon and van Balen, 2005; van Balen et al., 2005).

Continuous although moderate seismicity evidences the present-day tectonic activity of the Roer Valley Rift System. Figure 2.2 shows the earthquakes recorded by Royal Observatory of Belgium (ROB) (Camelbeeck et al., 2007). Compared to other areas in Europe, seismicity in northwest Europe, in particular, in the Roer Valley Graben area appears to be significant. In the case of the Roer Valley Graben, eleven earthquakes with magnitude of at least 5.0 were recorded since 1350 (Camelbeeck et al., 2007). During the last decades the earthquakes with the greatest magnitude occurred in Uden (The Netherlands) in 1932 of magnitude 5, in Roermond (The Netherlands) in 1992 of magnitude 5.9 and in Aachen (Germany) in 2002 of magnitude 4.9 (van Eck et al., 1993; Michon and van Balen, 2005). Their location can be found in fig. 2.2 from these dates.

The activity of the Roer Valley Rift System is also expressed in the topography (Houtgast and van Balen, 2000; van Balen et al., 2005). The Peel and Campine blocks are higher compared with the graben and the Venlo Block. The height differences are however small (∼20 m) as can be seen in the profile of fig. 2.3A (van Balen et al., 2005), suggesting that the slip of the graben is a slow process. Tectonic motion is also observed from the change in depth of the stratigraphic layers. This is shown in the deep seismic line of fig. 2.3B,

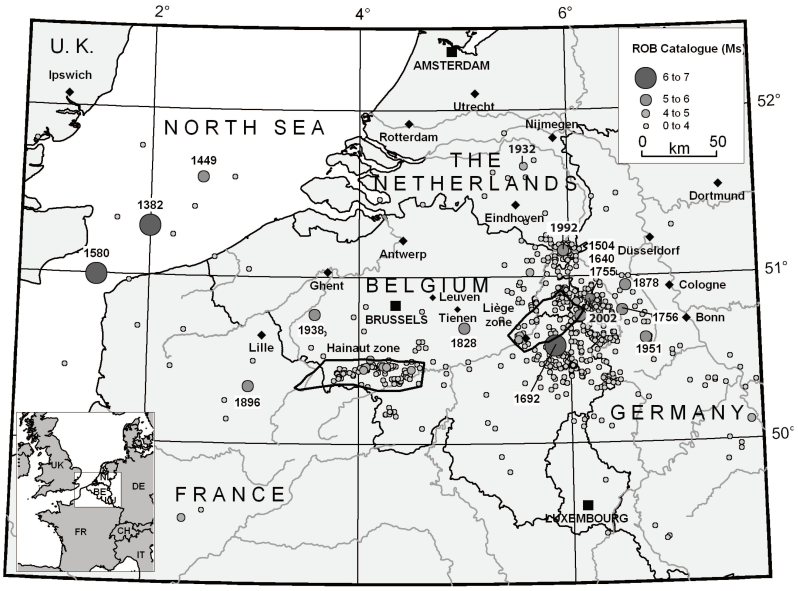

Fig. 2.2. Earthquake location in north-western Europe. High magnitude earthquakes also display the year, from Camelbeeck et al. (2007).

(Geluk et al., 1994), where stratigraphic layers appear deeper in the Roer Valley Graben than in adjacent blocks.

2.2.1 Tectonic Setting

The Roer Valley Rift System forms the northern extend of the Lower Rhine Graben, which is part of the Cenozoic mega-rift system, see fig. 2.1 (Ziegler, 1992; Houtgast et al., 2003; Cloetingh et al., 2006). In its western transect, the Cenozoic rift system extends from the shores of the North Sea to the Atlantic coast of north Africa. The inset graph of figure 2.1 shows the main graben structures forming the Cenozoic rift system. The Limagne and the Bresse grabens are found in south-west Europe. The Bresse Graben is structurally connected to the Upper Rhine Graben, which bifurcates into the Leine Graben with NE direction and to the Lower Rhine Graben to the NW direction (Ziegler, 1992; Cloetingh et al., 2006).

The present-day NW-SE stress field in western Europe is interpreted as a being caused by a combination of forces related to the continued convergence of Africa-Arabia with Europe, and consequent Alpine collision, in addition to the North Atlantic Ridge push (Gölke et al., 1996; Michon et al., 2003; Dezes et al., 2004).

Due to the NW-SE compression, the Upper Rhine Graben is subject to sinistral transtension (a combination of strike-slip and normal faulting), which may facilitate rifting in the Lower Rhine Graben and in the Roer Valley Graben (Michon et al., 2003; Dezes et al., 2004), see fig. 2.1.

Under the current stress fields, the structures that concentrate most of the deformation are the Upper Rhine and the Roer Valley grabens (Michon et al., 2003).

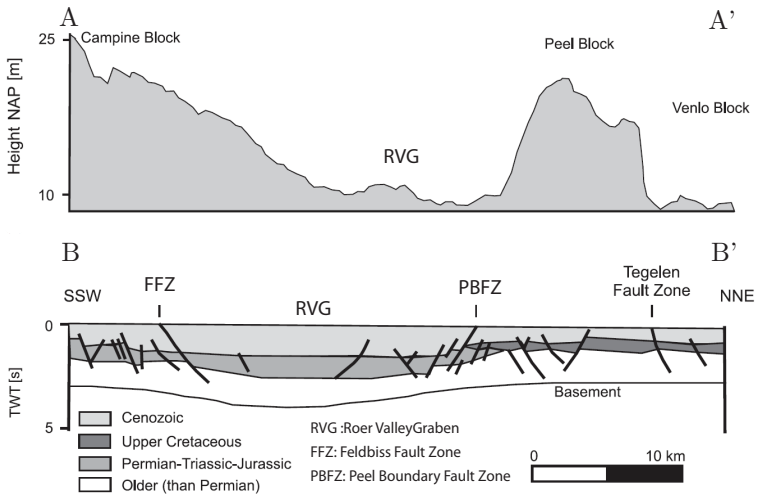

Fig. 2.3. A–A' Topographic profile across the Roer Valley Graben (RVG). B–B' Deep seismic line, located in the center of the rift perpendicular to the main fault systems, see location fig. 2.4. The Peel Boundary Fault System (PBFZ) and the Feldbiss Fault System (FFZ) are also shown, from van Balen et al. (2005) and Geluk et al. (1994)

In addition to that, glacial unloading of northern Europe seems also to influence the behavior of the Roer Valley Rift System. Paleoseismological data show an increase on the fault activity of the Roer Valley Graben that occurred around 10,000-15,000 yr BP and matched in time and extend with post glacial rebound models (Houtgast et al., 2005).

2.2.2 Neotectonic displacement rates

Seismic and geomorphological data demonstrate that the Roer Valley Rift System is active. However, there is not a general agreement on Neotectonic subsidence rates. Neotectonic subsidence rates estimated with techniques covering short time scales are one, and sometimes two, orders of magnitude higher than those estimated on geological time scale, see tab. 2.1. In this dissertation, the term *short time scale* is used to refer to scales in the order of decades (10–100 yr), meanwhile *geological scales* are long periods in the order of 10^5–10^7 yr.

Previous studies explained these discrepancies to be produced by either a variable rifting motion or errors in short time scale measurements. On the one hand, tectonic motions that accelerate in few decades are largely averaged when observed on geological time scales (Houtgast and van Balen, 2000; Michon et al., 2003; van Balen et al., 2005; Demoulin, 2006). In contrast to that, the second possible cause of the high rates observed in the Roer Valley Graben on short time scales can have a non tectonic origin, and could be due to inaccurate measurements and a non-tectonic signal, e.g., a man-induced displacement, that is misinterpreted as being tectonic (van den Berg et al., 1994; Vanneste and Verbeeck, 2001; Camelbeeck et al., 2002, 2007).

An overview of estimated tectonic rates is given in the following sections, where the dependence of estimated slip rates with the time scale becomes more apparent. For techniques

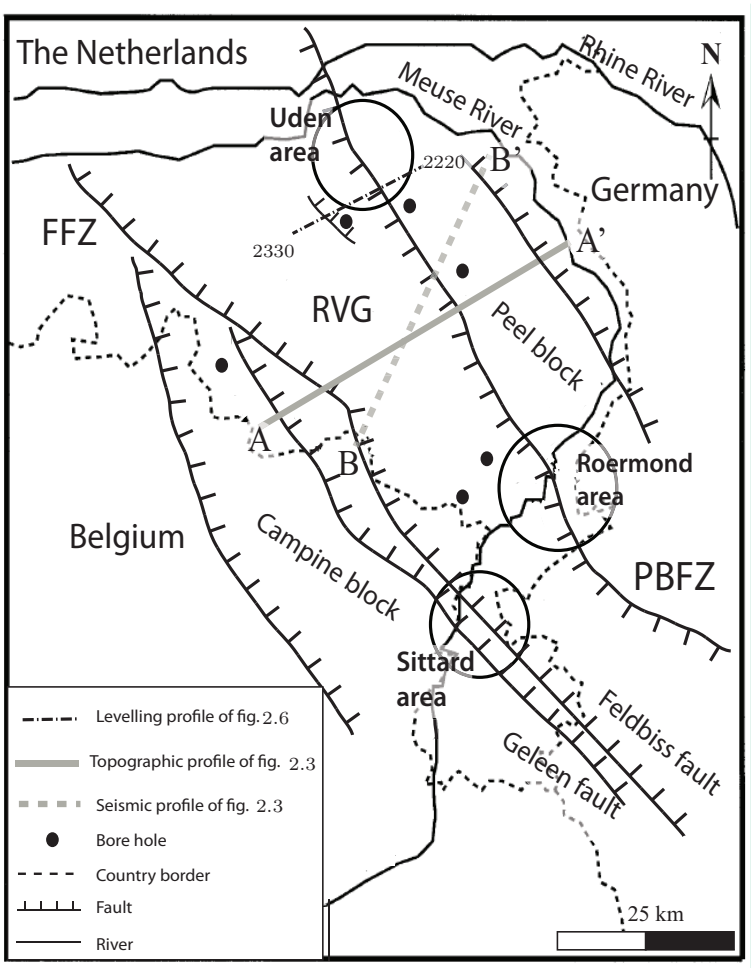

Fig. 2.4. Location of the measurements taken in the Roer Valley Rift System that are discussed in the text, after Houtgast and van Balen (2000). The leveling, topographic and seismic profiles are shown in figs. 2.6, 2.3A and 2.3B, respectively. The areas marked with a circle, Uden, Roermond and Sittard, were also studied using different techniques, e.g., trenching. Main fault zones (Peel Boundary Fault zone, PBFZ and Feldbiss Fault Zone, FFZ) are also indicated

measuring on geological time scales, we summarize the results of borehole analysis, trenching and analysis of high-precision Digital Elevation Models (DEM). For the short time scale case, we discuss the estimates obtained from leveling measurements.

Table 2.1. Estimated rates of Roer Valley Graben with respect to adjacent blocks. The values were computed in previous studies using boreholes, leveling, trenches and DEM (first column). A rough location of the measurements (w.r.t the graben) is also indicated, (Geluk et al., 1994; Houtgast and van Balen, 2000; Houtgast et al., 2003, 2005; Vanneste and Verbeeck, 2001; Michon and van Balen, 2005; Groenewoud et al., 1991; Lorenz et al., 1991; Demoulin, 2006)

Technique	Average rate [mm/yr]	Measurement location	Time scale
Borehole	-0.06	Whole graben	Geological
Trench	-0.05 to -0.20	Southeast	Geological
Trench	-0.02 to -0.04 (max -0.13)	South	Geological
DEM	-0.06	South	Geological
Leveling	-0.60 to -1.38	South	Decades
DEM	-0.18	North	Geological
Leveling	~ -1.0 (max ~ -5.0)	North	Decades

Rates at geological time scales (10^5–10^7 yr)

Borehole analysis

Tectonic rates are estimated with borehole analysis by identifying several layers at a given depth and estimating their age, e.g., with analysis of pollen content (Geluk et al., 1994). Relative rates between grabens and horsts are determined by comparing corresponding boreholes.

The analysis of the observations obtained with this technique for the Roer Valley Graben reveals a moderate tectonic subsidence of the graben with respect to adjacent blocks (Geluk et al., 1994; Houtgast and van Balen, 2000).

For the period $\sim 650 \cdot 10^3$ yr BP until present the average estimated subsidence rates of the Roer Valley Graben with respect to the Campine and Peel blocks, is -0.06 mm/yr and -0.05 mm/yr, respectively (Houtgast and van Balen, 2000). The location of the boreholes used in the studies of Houtgast and van Balen (2000) are shown in fig. 2.4.

Trenching

Trenching consist of analyzing how the depth of different lithostratigraphic layers, e.g., fluvial deposits, change with time across faults. In the Roer Valley Graben, several trenches have been studied in different areas. The analysis of the trench dug across the Geleen fault near Sittard, see location in fig. 2.4, shows graben slip rates to range between -0.02 to -0.04 mm/yr (Houtgast et al., 2003). Similar rates are estimated in a nearby trench excavated in the Feldbiss fault, also in the Sittard area. In this case, the Roer Valley Graben slips at -0.03 mm/yr with respect to the Campine Block (Houtgast et al., 2005) .

Southeast to this area, across the Peel Boundary Fault Zone, estimated slip rates are higher with values that are in the range of -0.05 to -0.20 mm/yr (Vanneste and Verbeeck, 2001).

Digital Elevation Model

Topography obtained from precise digital elevation models (DEM) can also be used to infer slip rates, from the age of the surface layers and by measuring the height difference between graben and horst.

This method was applied in the areas of Sittard, Roermond and Uden (Michon and van Balen, 2005), see location in fig. 2.4, using a precise DEM obtained with laser altimetry. The topographic offsets and the analysis of the age of fluvial terraces reveal the graben to slip in these three areas.

In Sittard, the estimated slip rate is -0.060 mm/yr with respect to the Campine Block. Graben slip rates across the Peel Boundary Fault are slightly higher with -0.065 mm/yr and -0.184 mm/yr in the Roermond and Uden areas, respectively.

Rates at short time scales (10–100 yr)

Estimates of slip rates at short time scales are obtained in the Roer Valley Rift System with leveling measurements (Groenewoud et al., 1991; van den Berg et al., 1994; Demoulin, 2006).

The Dutch Ministry of Infrastructure and Environment performs every $\sim$20 years leveling campaigns across the whole Netherlands. The Survey Department of Rijkswaterstaat of this ministry is responsible of the surveys, maintaining the network of benchmarks, and publishing estimated heights. The adjustment of the leveling networks result in heights with respect to the Normaal Amsterdams Peil (NAP), which is the Dutch vertical datum, (Rietveld, 1984).

The adjusted surveys that were carried out during the time periods 1926-1940 (second), 1950-1959 (third) and 1979-1987 (forth primary leveling campaigns), show an average subsidence of the graben with respect to the Peel Block in the order of -0.6 mm/yr after spatial interpolation (Groenewoud et al., 1991; Lorenz et al., 1991; van den Berg et al., 1994). Maximum estimated rates are around -1 mm/r, for the graben with respect to adjacent horsts. It has been suggested, (van den Berg et al., 1994), that this signal could be partially caused by nearby mining industry see fig 2.8. Apart from that, other non-tectonic sources of deformation seems to affect the graben. The rates estimated for the Roer Valley Graben correlates with the thickness of the Quaternary layer, which ranges from 0 to 500 m deep (Groenewoud et al., 1991; Lorenz et al., 1991). Previous works suggested that part of the originally observed subsidence could be related to sediment compaction not only tectonics (Groenewoud et al., 1991; Lorenz et al., 1991; Kooi et al., 1998).

The effect of sediment compaction down to 2 km is estimated by Kooi et al. (1998) along with the influence of glacio-isostatic adjustments (movements of the viscous lithosphere related to loading or unloading of material at the surface). Kooi et al. (1998) determines the tectonic rates after removing the modeled compaction and glacio-isostatic effects. To avoid the influence of shallow deformation processes, Kooi et al. (1998) employs only underground founded benchmarks, $\sim$30 m deep, of the primary and secondary leveling surveys. The total number of underground observations is 58 for the whole Netherlands.

Figure 2.5 displays the spatially interpolated results of the estimations before (A) and after (B) removing deep compaction and isostatic adjustment effects. The comparison of the two figures reveals that the overall pattern of the subsidence of the Roer Valley Graben does not change very much after subtracting the estimated non-tectonic effects. On average, the

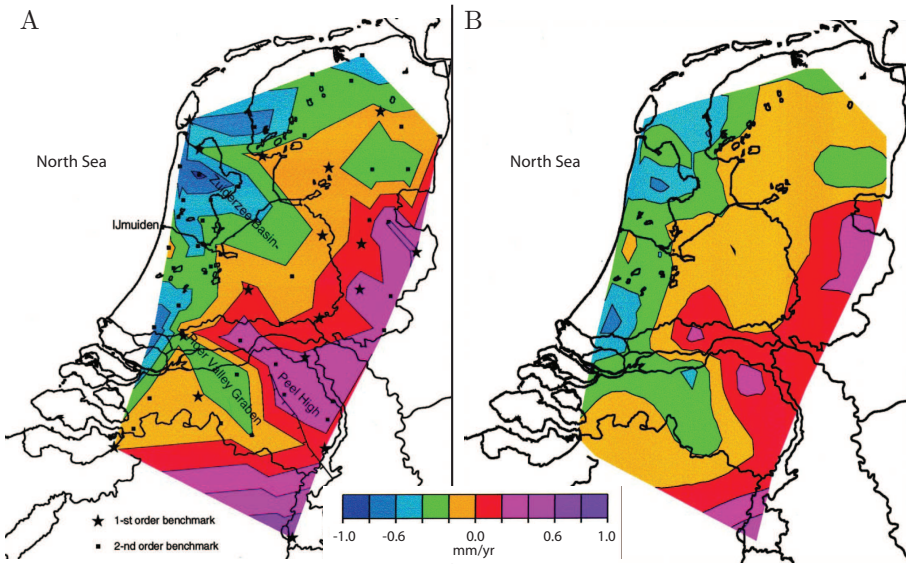

Fig. 2.5. (A) Vertical displacement rates (mm/yr) in the Netherlands obtained by least-squares kinematic adjustment of first- and second-order underground benchmarks. (B) After removing the effect of isostacy and deep (down to 2 km) compaction, from Kooi et al. (1998)

final values obtained for the subsidence rates of Roer Valley Graben with respect to the adjacent blocks is around −0.5 mm/yr.

Apart from these estimations at large scale, single profile lines have been analyzed in previous studies (Groenewoud et al., 1991; Lorenz et al., 1991; Demoulin, 2006). Figure 2.6 shows a leveling profile across the Peel Boundary Fault Zone in the Uden area, see location in fig. 2.4. The profile was performed at the second, third and forth primary surveys and adjusted using a kinematic least squares approach (Groenewoud et al., 1991; Lorenz et al., 1991). At the fault location, the estimations shows the graben to have subsided −10 cm between the third and second campaign and −6 cm between the fourth and the third. The corresponding rates are around −5 mm/yr and −3 mm/yr, respectively. At a distance far from the fault area, the Roer Valley Graben subsides at -1 mm/yr with respect to the Peel Block.

In the Sittard area, leveling profiles, which were carried out independently from the Dutch Survey Department of Rijkswaterstaat, reveal similar values for the Feldibss fault (Demoulin, 2006). The results show the graben to subside at a rate of −0.6 mm/yr from 2001 to 2004. For an earlier period spanning from 1985 to 2001, the estimated rate is −1.38 mm/yr, (Demoulin, 2006). For both periods, the observations manifested correlation with ground water variations. These effects were estimated and removed before calculating slip rates (Demoulin, 2006).

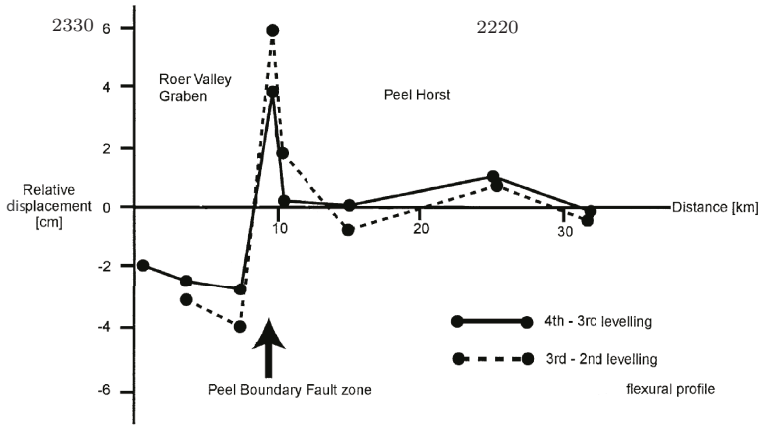

Fig. 2.6. Leveling profile across the Peel Boundary Fault Zone in the Uden area, see fig. 2.4, from Houtgast and van Balen (2000) modified after Groenewoud et al. (1991). Profile location is indicated in fig. 2.4.

2.2.3 Benefits of the application of InSAR time series to the Roer Valley Rift System

Studying the behavior of the Roer Valley Rift System is a complex task. Although the rift is active, the seismicity is moderate. Tectonic rates are expected to be low (-0.01 to -1 mm/yr), as shown in previous studies. Therefore, the tectonic signal could be difficult to capture. Furthermore, observations can also be polluted with deformation signals other than tectonics.

The techniques that have been applied so far have a very limited extend, which reduces the comprehension of the observed phenomenon and could lead to misinterpretations. The main advantages of InSAR time series compare to other geodetic techniques are its high spatial density of measurements, large coverage and high revisiting time. Even more, the archives provided by the satellites ERS1/2 and Envisat over the Netherlands allow us to examine the deformation in the Roer Valley Graben area from 1992 to 2010.
From the application of InSAR time series analysis, namely PSI, to the southern Netherlands we anticipate to benefit in different aspects. We expect to learn more about the nature of the motion observed in the area of Roer Valley Rift System, whether it is purely tectonics (only caused by rifting) or mixed with other signals. Almost two decades of measurements, divided into two data sets (one provided by ERS1/2 and the other by Envisat), are employed to estimate rates across the main faults. The satellite footprint of 100×100 km^2 assures that most of the graben is covered, which will improve our understanding of the deformation signal as a whole.

2.3 The Dutch coal mine industry and its effect on surface deformation

The Netherlands has a long history in coal mining, (see, e.g., Messing (1988)). The largest Dutch coal reserves are found in the province of Limburg, fig. 2.8. In this province, coal mining started in the 14th century. The initial exploitation was simple opencast mining, but soon after was conducted from galleries and later from shafts (TNO, 1999). Although the exploitation was performed for centuries, the extraction did not take an industrial scale

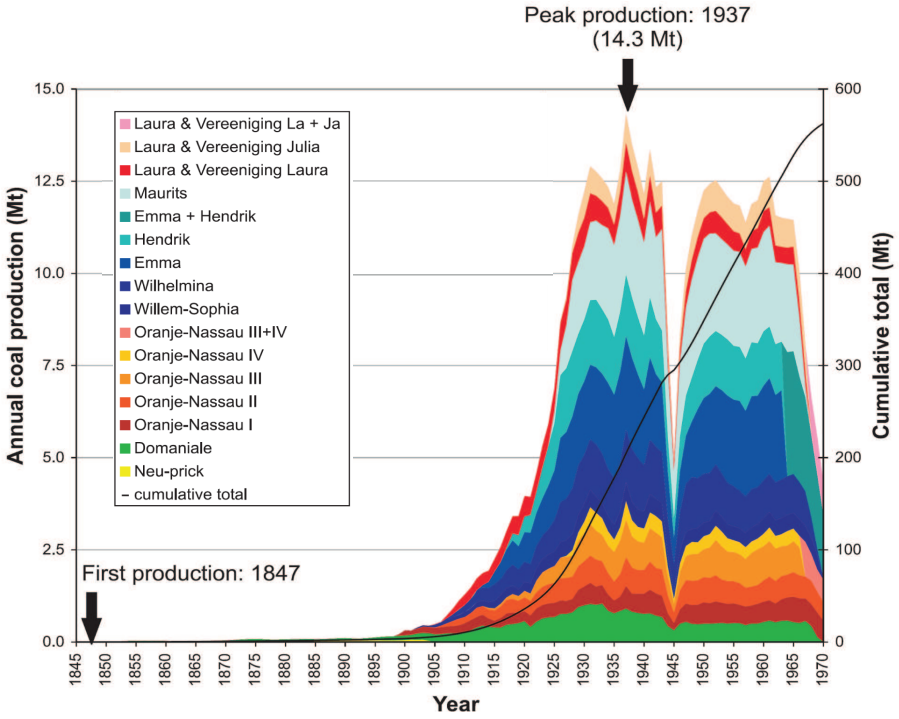

Fig. 2.7. Net annual coal production from 1847 to 1970 of the mines in South-Limburg indicated in fig. 2.8 (after Bergen et al. (2007) from data of Westen (1971)). Production completely ceased in 1974. The colors reflect the production of different mine concessions, see location in fig. 2.9.

until the beginning of the twentieth century. Figure 2.7 shows the net annual production of coal from 1847 till 1970 (Bergen et al., 2007).
The period of the most intensive exploitation occurred from 1925 to 1965 with an annual average of 12 million tons, with the exception of the time during World War II (Bergen et al., 2007). The mine concessions with highest production rates were Maurits and Emma, see location in fig. 2.9. They were also the largest mines in the Dutch field.

Adjacent countries also exploited the coal. Figure 2.8 displays the location of the Dutch, German and Belgian coal fields in the southern Netherlands and adjacent areas; the location of the Roer Valley Graben is also indicated for clarity. In Germany, coal was mainly produced in the districts of Aachen and Erkelenz. Transnational coal mining was conducted along the Dutch-German border with coal districts being communicated with a series of underground galleries (Heitfeld et al., 2002).

The long-term intensive extraction resulted in a ground subsidence of several meters (Pöttgens, 1985). Subsidence in mining areas is produced by two different causes: mineral extraction and water pumping. The actual extraction of coal reduces support of the upper layers producing the consequent subsidence. As the coal is extracted, the roof layer that separates the rock mass above from the coal seams, breaks and collapses on top of the stowing material. If no stowing is applied, the roof layer collapses directly on the floor filling the

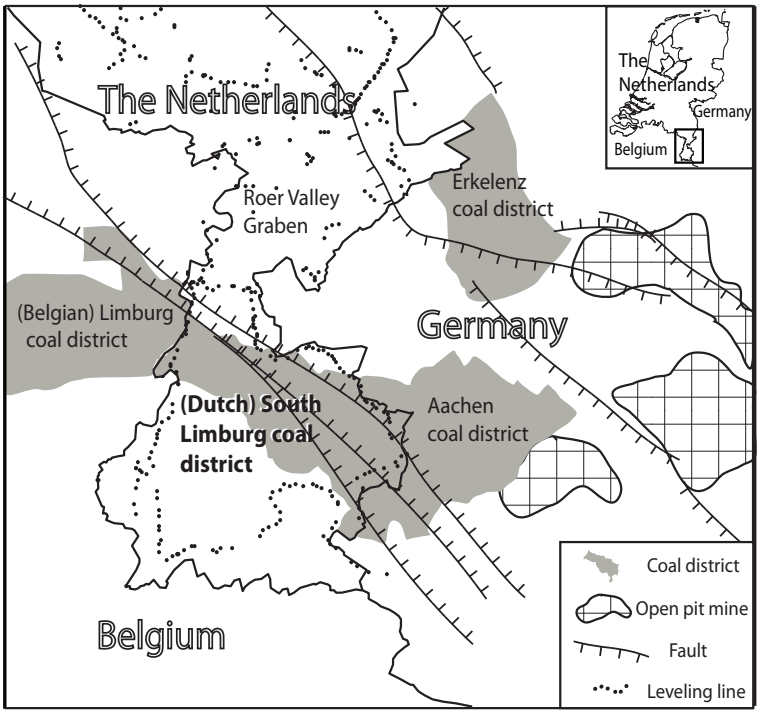

Fig. 2.8. Coal fields in the southern Netherlands and adjacent borders, after TNO (1999); Heitfeld et al. (2002); Devleeschouwer et al. (2008). Lignite mines are open pit mines found to the south-east of Limburg, in Germany. Reliable leveling benchmarks that were measured at least three times during the period 1992-2009 are also displayed (Rijkswaterstaat, 2011), although different leveling networks have been deployed locally in this area (Rosner, 2011), not shown in the figure.

mine opening with rock debris. As a result the above layers deflect downwardly, producing at the surface displacements that are nearly vertical with an area of influence limited by an angle ($\sim 45^o$)(Kratzsch, 1983; Bekendam and Pöttgens, 1995).

In addition to that, since coal extraction requires dry working environment, water is continuously drained. Water pumping reduces rock pore pressure, with the consequent decrease in volume of the rocks, which translates as subsidence in the surface.

Figure 2.10A shows the total surface deformation estimated from leveling measurements during the period from 1915 to 1974 (Pöttgens, 1985). Maximum values are up to $\sim$10 m.

In the seventies, the exploitation became less economically interesting and the production started to decline, see fig. 2.7. By 1974, all Dutch mines were closed. The German and Belgian underground mines stopped in the 1980's and 1990's. Currently for this area, only the open cast lignite (brown coal) mines, which are located in Germany, see fig. 2.8, remain active. The production of brown in the Germany boosted in the 1960's after the three main companies merged into one. In the last decade, production rates have been in the order of 90 million tonnes of lignite per year, reaching depths of up to 400 m (Herrmann et al.,

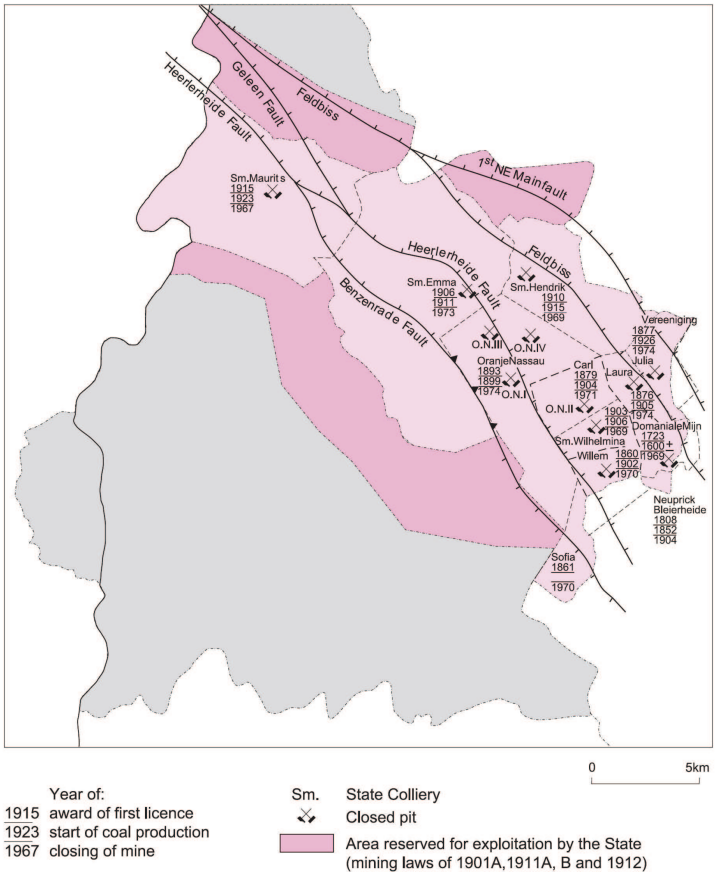

Fig. 2.9. Mine concessions in the coal district of Limburg, see fig. 2.8, after TNO (1999).

2009).

Soon after the Dutch mines were closed in 1974, pumping halted almost completely and water levels started to increase. To protect from flooding the German mines that were still active at this time, a system of subsurface water barriers (dams) was installed by sealing most of galleries connecting the mine concessions (Bekendam and Pöttgens, 1995; Rosner, 2011). These galleries were initially used for safety as evacuation corridors (Wings, pers.comm. 2011).

The underground dam system divided the coal field into a series of compartments that served as *water basins* and corresponded to the original concessions. The independent water pumping that was performed during the coal extraction caused the, so-called, water basins to have different initial water depths. The water basins were connected through overflowing galleries that directed the flow towards the only remaining pump in the field, which was located in the shaft of Beerenbosch II, see fig. 2.11.
Figure 2.11 shows the water level of the basins measured in 1994, just before the pumping completely ceased (Heitfeld et al., 2002, 2007). Major faults are also depicted to show

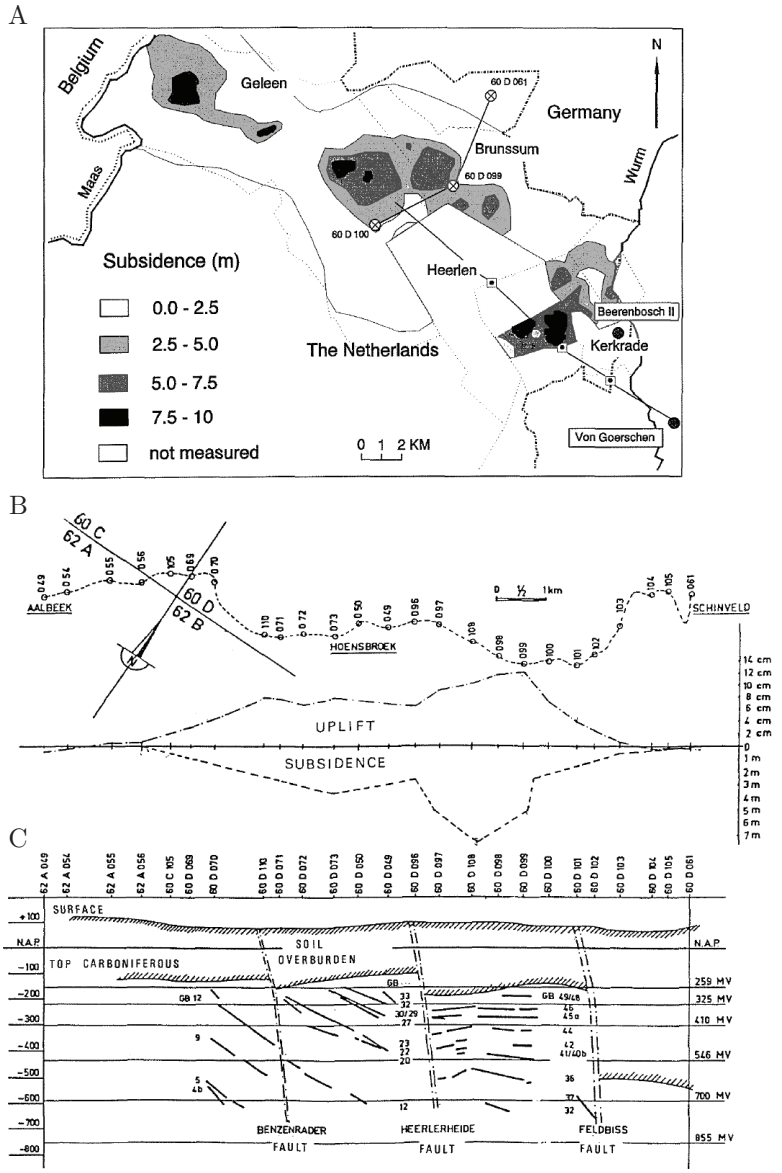

Fig. 2.10. A) Subsidence map estimated from leveling measurements (Pöttgens, 1985). B) Profile 60D100–60D099–60D061 (see A) showing the cumulative subsidence from 1915 to 1974 and the total uplift from 1974 to 1984 (Pöttgens, 1985). C) Coal seams and fault location corresponding to previous profile (Pöttgens, 1985).

how they bound aforementioned water basins. The inset diagram (A–A') in fig. 2.11 shows the overflowing levels and the water regime when the pump in Beerenbosch II was active, (Bekendam and Pöttgens, 1995).

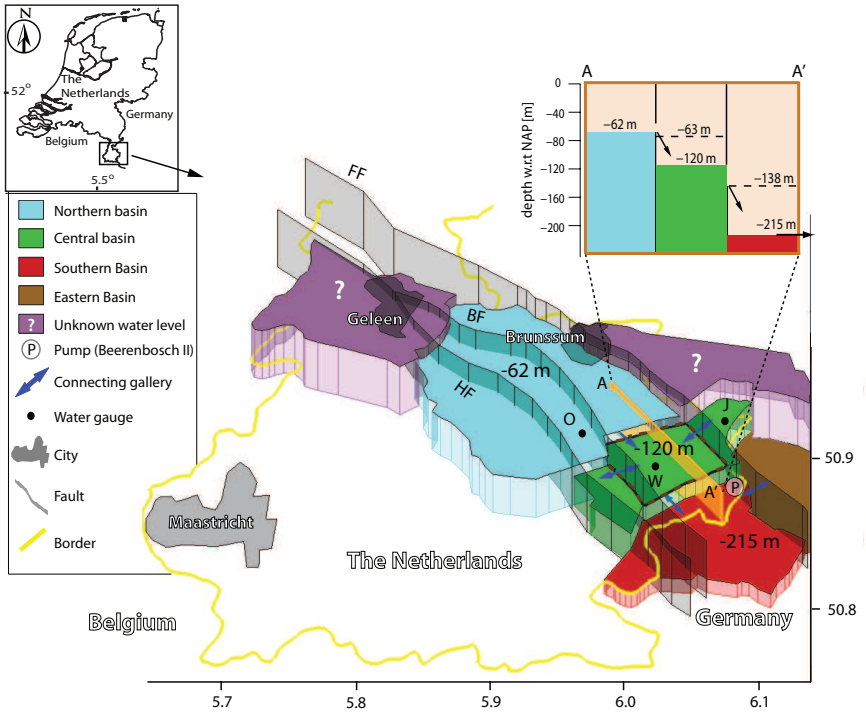

Fig. 2.11. Water levels in the mining area in 1994. The values are with respect to NAP. The dam system put in place to protect the active mines created a system of water basins (Heitfeld et al., 2002). Some water levels are unknown and are displayed with a question mark (?). The inset figure A–A' the water regime when the pump in Beerenbosch II (showed with a encircled P) was active, (Bekendam and Pöttgens, 1995).

The cease of pumping in 1994 led to a rapid increase in water levels. Soon after the pump was dismantled, the water levels in Beerenbosch II reached a depth of −138 m NAP (the local topography is about 100 m NAP), and started to overflow towards the central basin (Heitfeld et al., 2002; SoDM, 2007; Rosner, 2011).

2.3.1 Surface deformation after mine closure

Abandoned mines can still contribute to surface deformation due to two different mechanisms: residual subsidence and water rebound. Residual subsidence is a delayed reaction to the extraction that can manifest after the cease of mining. The causes of the delay depend on the mechanical properties of the rock, the extraction method and its depth (Blodgett and Kuipers, 2002). On the other hand, water rebound is consequence of the cease of water pumping after mine abandonment. The raising waters make the land to uplift due to rock expansion caused by pore pressure increase (Pöttgens, 1985; Bekendam and Pöttgens, 1995; Heitfeld et al., 2006; Devleeschouwer et al., 2008; Rosner, 2011).

In the case of the Dutch coal mines, only the water rebound effect have been reported (Pöttgens, 1985; Bekendam and Pöttgens, 1995), residual subsidence have not been detected. Not anticipated at the moment when the mines were abandoned, first indications of uplift were observed for an incidental leveling line in 1978, four years after closure of the last mine (Pöttgens, pers.comm. 2008). Leveling campaigns have been carried out since then.

From these leveling observations, Pöttgens (1985) also found high correlation between uplift and previous subsidence, which suggest that part of the initial subsidence was caused by water pumping performed during the extraction. Figure 2.10B compares the total subsidence with the uplift obtained from 1974 to 1984, after (Pöttgens, 1985). The general pattern of the uplift matches very well the subsidence, although the maximum ground heave does not correspond to the maximum in subsidence. The measurements also show a maximum uplift of 22 cm near Brunssum.

Pöttgens (1985) explained the uplift due to pore pressure increased induced by water rebound; this is further discussed in the following section.

2.3.2 Modeling water rebound: The strain source concept

Modeling the effect of water rebound helps to predict surface displacements and to understand the mechanical properties of the subsurface and water dynamics. Although, the geometry of mines is usually more complicated than aquifers or other systems where flow models are applied (Wolkersdorfer, 2008), simple experimental models have proved also to be valuable (Pöttgens, 1985). In the Netherlands, the uplift caused by water rebound in the abandoned mines has been modeled with the strain source concept[1] (Pöttgens, 1985). Strain sources were first introduced by Geertsma (1973) to explain the relationship between gas reservoir compaction and surface subsidence, assuming a uniform elastic half-space. It is also worth notting that the concept of strain source is similar to the approaches of Anderson (1936) and Mogi (1958). The shape of the reservoir is then taking into account in the model by using a field of strain sources and integrating them spatially.

Pöttgens (1985) employed the strain sources to study surface uplift in the Dutch coal mines. As explained in the introduction, he suggested that the rising waters produced an increase of pore pressure in the disturbed rock. The consequent rock volume increase translated into surface uplift. Furthermore, during coal extraction, the porosity of the rock is considerably increased making the rock prone to ingress water (Pöttgens, 1985; Bekendam and Pöttgens, 1995).

Geertsma (1973) proposed that the vertical displacement, d_U, produced by a strain source of small but finite volume V at the depth D due to pore pressure change Δp, could be calculated from

$$d_U(R,0) = -\frac{1}{\pi} d_m (1-\nu) \frac{D}{(R^2+D^2)^{\frac{3}{2}}} \Delta p V, \tag{2.1}$$

where R is the radial distance to the strain source, 0 corresponds to the ground level surface, and ν is Poisson's ratio. The term d_m is the uniaxial dilation coefficient, which was

[1] The term *nucleus of strain* is here renamed as *strain source*.

originally defined by Geertsma and van Opstal (1973) as uniaxial compression coefficient and renamed by Pöttgens (1985). This is given by

$$d_m = \frac{1}{H}\frac{dz}{dp}, \tag{2.2}$$

where p is the pressure and H is the initial height (vertical size) of the strain source.

Assuming that volume increase primarily occurs in the vertical dimension, eq. (2.2) can also be written as

$$d_m = \frac{1}{V}\frac{\Delta V}{\Delta p}, \tag{2.3}$$

where V is the volume of the reservoir equal to the assumed fixed horizontal extension of the reservoir times the vertical dimension.

Thus, eq. (2.1) can also be expressed as

$$d_U(R,0) = -\frac{1}{\pi}(1-\nu)\frac{D}{(R^2+D^2)^{\frac{3}{2}}}\Delta V, \tag{2.4}$$

where ΔV is the volume change of the strain source. The total vertical deformation at the surface produced by a field of strain sources is calculated by summing the contribution of each source (Geertsma and van Opstal, 1973).

A parameter equivalent to d_m is the storage coefficient S_{ke}. Since storage coefficient is usually employed in hydrological studies, e.g., aquifer characterization (Hoffmann, 2003; Bell et al., 2008), we prefer to employ it, S_{ke} , to describe the response of the fractured rock to water level fluctuations.

The storage coefficient gives a first approximation of the relationship between water level increase and rock dilatation (Hoffmann, 2003). When small changes in the effective stress happen, as it is usually the case when they are caused by changes in hydraulic heads, this relationship is linear:

$$S_{ke} \approx \frac{\Delta z}{\Delta h_{\text{water}}}. \tag{2.5}$$

The storage coefficient S_{ke} states the vertical expansion of the rock Δz for a certain water level change Δh_{water}.

2.3.3 Benefits of the application of InSAR to study the abandoned coal fields of the southern Netherlands

South Limburg is one of the largest abandoned mining regions in Europe. This industry have influenced the surrounding environment, particularly underground water levels, over large distances. Jointly with the Aachen coal district in Germany, they affected the water levels within an area of 400 km^2 (Wolkersdorfer, 2008). As we discussed above, underground water levels started to increase after the mines in these areas were completely abandoned in 1994. In some areas the water levels have increase around 200 m. Although, the effect of ground water rebound is being monitored (Heitfeld et al., 2002; Rosner, 2011), combining measurements obtained from water gauges and leveling, most of the efforts have been allocated in the German-Dutch border. Our knowledge of the deformation field is therefore limited, leaving the west side of the Dutch mines with the biggest uncertainties.

Furthermore, the current applied techniques (leveling and water gauges) have the disadvantage of being limited in extend and spatially sparse. Figure 2.8 shows the location of reliable leveling benchmarks in Limburg belonging to the Dutch network(Rijkswaterstaat, 2011), which mostly measured the area near the Dutch borders. Other leveling networks with increase density are deployed locally to study surface displacements in Limburg (Rosner, 2011); however, they mostly cover the east side of the Dutch mines. The density of observations, coverage and measurement frequency are significantly lower than the ones provided by InSAR. In the case of water levels gauges the spatial density is even lower because the technique needs physical access to galleries. Five water gauges are currently installed in the Dutch coal field (Heitfeld et al., 2002).

InSAR can therefore improve the analysis of the deformation signal. We expect that the detailed data provided by InSAR for the whole Dutch coal field will contribute to improve our understanding of the deformation signal in the area, including its spatio-temporal behavior and the relationship with groundwater.

Furthermore, we also expect a high density of observations to be provided by InSAR which will enhance the monitoring of the effect of tectonic faults on the deformation. Tectonic faults deserve a major attention as they can produce severe infrastructure damage when they are in the proximity of abandoned mines (Donnelly, 2000; Donnelly and Rees, 2001). For example, water rebound in the old mines of Erkelenz (see location in fig. 2.8) seems to have induced fault reactivation in the city of Wassenberg in the year 2000 (Heitfeld et al., 2006). Deformation of 8 cm across tectonic faults over a distance of less than 50 m was reported for this city and produced sever damage in at least 9 buildings, (Heitfeld et al., 2006). Until now, fault reactivation has not been reported for our area of interest, the mines in Limburg; however, we expect tectonic faults to play a major role in the deformation field as they bound both mine concessions and the artificial water basins formed after their abandonment. Although an in-depth risk assessment due to water rebound is beyond the scope of this research, we anticipate that the result of our analysis will point out areas that may be prone to infrastructure damage.

2.4 Summary

This chapter described two sources of ground motion that are associated geological faults: Roer Valley Rift System and the mining industry in the southern Netherlands. The chapter gave a general overview of the two phenomena focusing on the areas where their studies could benefit from InSAR. In the case of Roer Valley Rift System, we saw that temporal behavior of the rift was unclear, mainly because the large differences found in slip rates when measured in short and geological time scales, see e.g. Michon et al. (2003); van Balen et al. (2005); Demoulin (2006); Vanneste and Verbeeck (2001); Camelbeeck et al. (2007). We expect the results provided by InSAR to help in the clarification the cause of these differences.

Concerning the mining industry, previous studies, (see e.g., Pöttgens (1985); Bekendam and Pöttgens (1995); Heitfeld et al. (2006); Rosner (2011)), explained surface displacements to be related to water level increase. In this dissertation, we attempt to bring further previous studies by providing an in-depth analysis of the displacement field. With time series InSAR, we anticipate to gain in the density of observations, which can also improve deformation monitoring and our understanding of the deformation field and how it is controlled by near tectonic faults. We also expect to be able to better understand water dynamics, which have been suggested to be the main cause of deformation, and the response of the mined ground to water level changes.

Chapter 3

Time Series InSAR Analysis: The Persistent Scatterer Interferometry Approach

3.1 Introduction

This chapter is dedicated to Persistent Scatterer Interferometry (PSI) techniques. Since, PSI methods apply time series analysis to Interferometric Synthetic Aperture Radars (InSAR) observations, we start reviewing the main principles of InSAR to continue with concepts that are the foundations of most PSI methods. PSI methods are described in the framework of DePSI (the Delft implementation of PSI) which is the reference technique of this research. We describe the PSI algorithm with particular interest in temporal phase unwrapping, which is probably the most relevant step in the majority of PSI methods.

3.2 InSAR principles

Synthetic Aperture Radars (SAR) are imaging radars that use the sensor motion to increase artificially the antenna size. This translates into an improvement of the resolution in the direction of motion (azimuth direction) of three orders of magnitude with the respect to the resolution provided by a real size antenna. The improvement of the resolution in the perpendicular (range) direction is achieved by pulse compression methods. The reader is referred to Stimson (1998) and Cumming and Wong (2005) for further reference on SAR.

SAR images are composed of a regular grid of pixels that store both real and imaginary parts of received echoes, from which amplitude and phase can be calculated.

InSAR techniques use the phase differences between two radar images acquired over the same area to generate maps of, e.g. surface displacements or topography (Massonnet et al., 1994; Bamler and Hartl, 1998; Hanssen, 2001). These two images are usually referred to as *master* and *slave* and their complex product, from which phase differences are extracted, as *interferogram*.
Interferograms cannot be directly computed from SAR images, because they are acquired from slightly different locations. This means that the slave image must be first coregistered (Gabriel and Goldstein, 1988; Prati and Rocca, 1990; Samson, 1996) and then resampled to the master geometry (Hanssen and Bamler, 1999; Hanssen, 2001).

The coregistration process computes an initial offset between master and slave from orbital information. Then, this value is more accurately calculated by searching for the location that maximizes the correlation between the amplitude images. This is performed with a

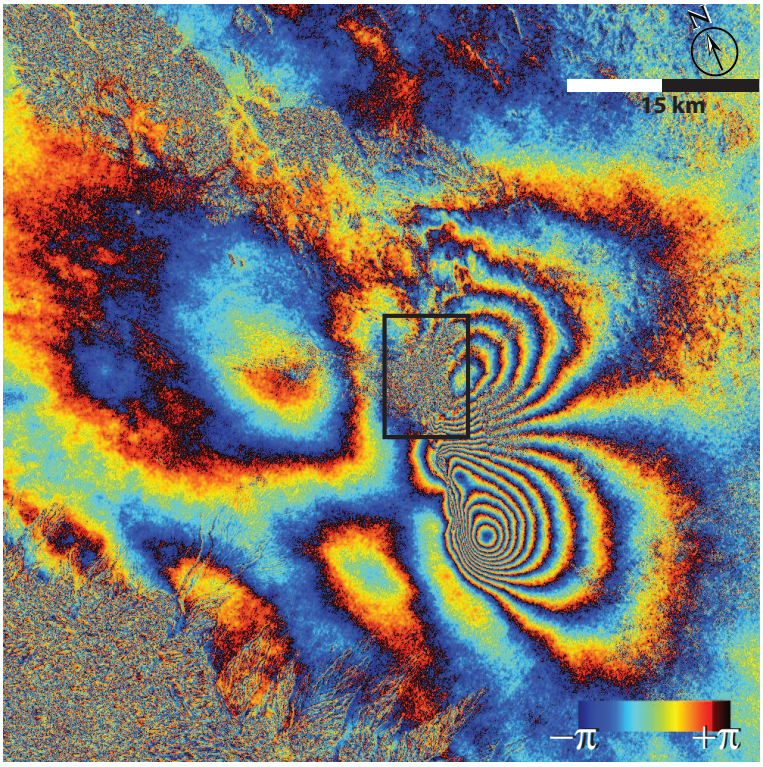

Fig. 3.1. SAR interferogram observing the Bam earthquake, Iran (December 2003). Phases are wrapped, i.e. phases are only known as the 2π modulus of the absolute phases. One fringe—color cycle—represents 28 mm of the deformation associated to the 2003 Bam earthquake projected on the satellite line-of-sight.

set of uniformly distributed windows and referred to as coarse coregistration.

InSAR requires coregistration at a subpixel level to ensure coherent interferograms. Therefore, the estimated coarse offset is further improved by using oversampled windows—also uniformly distributed—and searching again for the location that maximizes the correlation between master and slave amplitude images. The output of this process is a fine (precise) offset value per window location. A mapping function, which usually is a second degree polynomial, is determined using the fine offsets as observations. Finally, with the mapping function, the whole slave image is resampled to the master geometry.

An interferogram I is formed by multiplying the master image M with the complex conjugate of the resampled slave S:

$$I = M \cdot S^* = A_M e^{j\phi_M} A_S e^{-j\phi_S} = A_{MS} e^{j\phi} \tag{3.1}$$

with the superscript $*$ denoting complex conjugate and where the terms A_M and A_S are the amplitude of the master and slave, respectively and ϕ_M ϕ_S their phases. A_{MS}, the

interferogram amplitude, is equal to $A_M A_S$ and the interferometric phase ϕ represents the phase difference between master and slave images. This operation is performed for each pixel.

Figure 3.1 shows an example of the phase of an interferogram. Although there are different contributions to interferometric phases, the color fringes of fig. 3.1 mostly represent surface displacements associated to the earthquake that occurred in Bam (Iran) in December 2003 (Talebian et al., 2004; Fialko et al., 2005).

3.2.1 Contributions to the interferometric phase

Interferometric phases can be written as a summation of different contributions, (Hanssen, 2001; Kampes, 2006):

$$\phi = \mathbb{W}\{\Phi_{\text{ref}} + \Phi_{\text{topo}} + \Phi_{\text{defo}} + \Phi_{\text{subpx}} + \Phi_{\text{orb}} + \Phi_{\text{atm}} + \Phi_{\text{scat}} + \Phi_{\text{noise}}\}, \tag{3.2}$$

where

- $\mathbb{W}$ is the wrapping operator,
- Φ_{ref} is the contribution of a reference body from which heights are measured, e.g., the ellipsoid WGS84,
- Φ_{topo} accounts for the height of a pixel with respect to the reference frame,
- Φ_{defo} is due to ground motion between master and slave times,
- Φ_{subpx} is produced by a difference in location between the assumed phase center, which is usually taken in the upper corner of the resolution cell and the real phase center,
- Φ_{orb} is the phase shift due to orbital inaccuracies,
- Φ_{atm} is the atmospheric delay difference between master and slave images, and it is also referred to as atmospheric phase screen (APS),
- Φ_{scat} is due to a change in the scattering properties of the pixel in question,
- Φ_{noise} refers to the phase noise and includes terms such as system noise.

These terms are further described in the following subsections.

The wrapping operator

Interferometric phases are wrapped. This means that phase values are only known as the 2π-modulus of the absolute (or *unwrapped*) phase Φ. The absolute value Φ is estimated from the integer number of cycles a such that

$$\Phi = \phi + 2\pi a, \text{ with } \phi \in [-\pi, \pi),\ \Phi \in \mathbb{R} \text{ and } a \in \mathbb{Z}. \tag{3.3}$$

In the interferogram of fig. 3.1, the color fringes represent wrapped phase cycles that appear due to the cyclical nature of the observed phases.

Although the wrap operation, $\phi = \mathbb{W}\{\Phi\}$, is straight forward, the inverse, i.e. the estimation of the number of cycles a, cannot be solved unless some information is added to the problem, e.g. assuming additional conditions. This operation, unfolding the phase outside its natural interval, is usually referred to as phase unwrapping. Phase unwrapping, which is probably the most important operation in InSAR, is discussed in depth in section 3.5 with especial interest in time series methods.

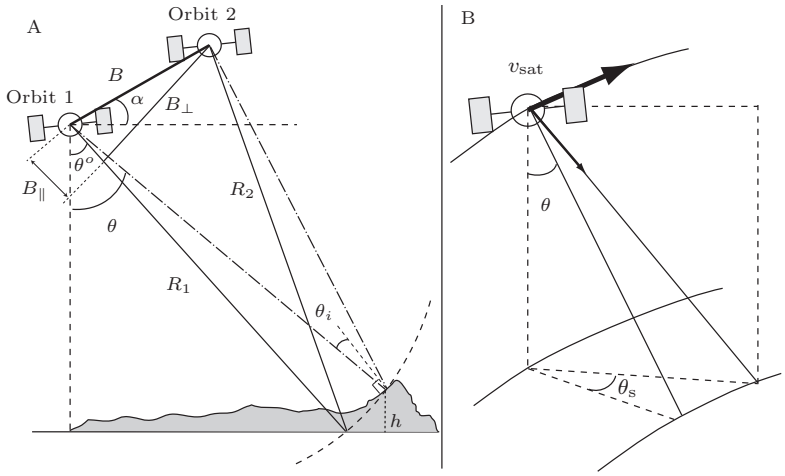

Fig. 3.2. (A) InSAR acquisition geometry for a target at a height h w.r.t. a reference body, where θ is the look angle, and θ^o is the look angle for the reference body, and θ_i is the local incidence angle. The baseline is represented with B, $B_\parallel$ is the parallel baseline and $B_\perp$ the perpendicular baseline. R_1 is the distance between the position of the satellite in orbit 1 and a target on ground, the same for R_2 and orbit 2. (B) 3-D view of satellite geometry. The squint angle is represented with θ_s, the look angle with θ, and satellite velocity vector with v_{sat}

Reference phase

The reference phase Φ_{ref} is the expected interferometric phase for a reference body, such as the ellipsoid WGS84. The reference phase is defined as (Hanssen, 2001)

$$\Phi_{\text{ref}} = \frac{4\pi}{\lambda} B \sin(\theta^o - \alpha), \tag{3.4}$$

where B is distance, or baseline, between sensors position, θ^o is the look angle for the reference surface, see fig. 3.2A. The angle α depends on the relative position between master and slave acquisitions, as shown in fig. 3.2A.

The term $B \sin(\theta^o - \alpha)$ is the parallel baseline (for the reference surface) usually denoted as $B^o_\parallel$. For a generic look angle θ this is written as

$$B_\parallel = B \sin(\theta - \alpha). \tag{3.5}$$

These values $B_\parallel$ and $B^o_\parallel$ differ very slightly for a point at some elevation.

It is worth notting that the definition of Φ_{ref} given in eq. (3.4) is independent of the chosen reference body; although in fig. 3.2A it is drawn flat.

Topography

The topographic phase Φ_{topo} for a point with a height h with respect to a reference ellipsoid is approximated with (Hanssen, 2001; Usai, 2001)

$$\Phi_{\text{topo}} \approx \frac{-4\pi B_{\perp}^{o}}{\lambda R_1 \sin\theta^{o}} h, \text{ with } B_{\perp}^{o} << R_1 \tag{3.6}$$

where the wavelength of the transmitted signal is denoted by λ and R_1 is the distance between the satellite and the observed point on Earth. The perpendicular baseline $B_{\perp}$ is the effective distance between two sensor positions, measured perpendicular to the look direction θ,

$$B_{\perp} = B\cos(\theta - \alpha). \tag{3.7}$$

The *naught* versions $B_{\perp}^{o}$ and θ^{o} indicate their respective values for a reference body. This geometry is depicted in fig. 3.2A.

The approximation used in eq. (3.6), also referred to as *far field approximation*, assumes that the distance from the sensor to the ground R_1 is much larger than the satellite baseline $B_{\perp}$. For spaceborne radar, this is a reasonable approximation because R_1 is in the order of hundreds of kilometers and B is usually not larger than a few hundred meters.

The height equivalent to a full phase cycle is referred to as height ambiguity:

$$h_{2\pi} = 2\pi \frac{\lambda R_1 \sin\theta^{o}}{-4\pi B_{\perp}^{o}} = -\frac{\lambda R_1 \sin\theta^{o}}{2B_{\perp}^{o}}. \tag{3.8}$$

This implies that for C-band satellites (λ ∼0.056 m and $\theta \sim 23^{o}$) and 100 m perpendicular baseline, the height ambiguity is around 100 m. If the baseline doubles (200 m), the height ambiguity halves (50 m), and vice-versa.

Surface displacements

The interferometric phase Φ_{defo} caused by a surface displacement that occurs between master and slave acquisitions can be written as (Hanssen, 2001)

$$\Phi_{\text{defo}} = \frac{-4\pi d}{\lambda}, \tag{3.9}$$

where d is the surface displacement projected on the satellite line-of-sight, see fig. 3.3A.

In the interferogram shown in fig. 3.1 most of the phase fringes are caused by surface displacements associated to the Bam earthquake. The sensor, Envisat had a wavelength λ ∼56 mm; hence, each color cycle of this interferogram represent 28 mm deformation observed on the line-of-sight.

Deformation observed by InSAR depends on the look angle (θ) and satellite heading on ground (θ_h). For a generic displacement vector with components d_U, d_N and d_E in the Up, North and East directions, respectively, the projected line-of-sight deformation is given by

$$d = d_U\cos\theta + d_N\sin\theta\sin\theta_h + d_E\sin\theta\cos\theta_h, \tag{3.10}$$

see fig. 3.3B.

For the European satellites, ERS1/2 and Envisat, the look and heading angles are $\theta \approx 23^{o}$ and $\theta_h \approx 10^{o}$, respectively. This means that these satellites are mostly sensitive to vertical displacements and almost insensitive to the North component.

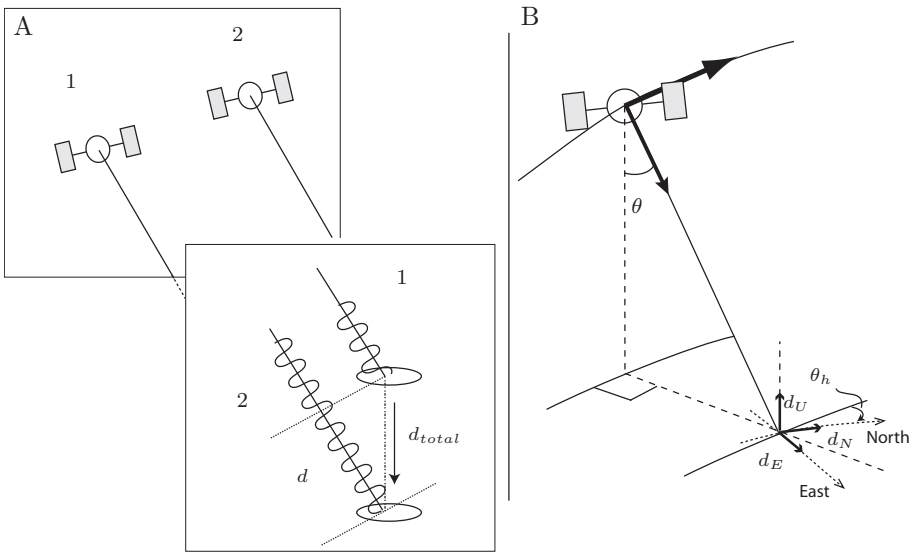

Fig. 3.3. (A) Surface displacements as observed by the satellite sensor; d is the projection on the satellite LOS of the total displacement d_{total}, having only an Up component, i.e. vertical. (Satellite flying direction is perpendicular to the paper plane.) (B) 3-D view of a displacement vector in the satellite geometry. The heading direction is represented with θ_{h} measured clockwise. The displacement vector between acquisitions 1 and 2 is represented with three components d_U, d_N and d_E in Up, North and East directions, respectively.

In time series analysis, surface displacements are usually assumed to be a function of the time difference between master and slave images, i.e., the temporal baseline B_{temp}. If this relationship is linear eq. (3.9) becomes

$$\Phi_{\mathrm{defo}} = \frac{-4\pi}{\lambda} B_{\mathrm{temp}} v, \tag{3.11}$$

where v represents the deformation rate.

Subpixel position

The term Φ_{subpx} is caused by the difference between the assumed and the true phase center of a resolution cell (Kampes, 2006; Perissin and Rocca, 2006; Marinkovic et al., 2008). This difference is also referred to as subpixel position. The phase center of a pixel is assumed to be in its upper left corner. However, if the reflections in the resolution cell are dominated by a single scatterer the phase center is given by the position of the scatterer inside the resolution cell.

The interferometric phases produced by subpixel position of ξ in azimuth and of η in range are given by (Kampes, 2006; Perissin and Rocca, 2006; Marinkovic et al., 2008),

$$\Phi^{azim}_{\mathrm{subpx}} = \frac{2\pi}{v_{\mathrm{sat}}} \Delta f_{DC} \xi, \tag{3.12}$$

$$\Phi_{\text{subpx}}^{range} = \frac{-4\pi}{\lambda}\frac{B_\perp}{R_1}\cos\theta\eta, \tag{3.13}$$

respectively.

The term R_1 is the distance from the satellite to the reference surface, and as before, $B_\perp$ and θ are the perpendicular baseline and the look angle. In addition to that, v_{sat} is the velocity of the satellite and Δf_{DC} the Doppler centroid difference between the acquisitions forming the interferogram (Bamler and Runge, 1991).

The Doppler frequency is the change in frequency due to the relative motion between satellite and target. In particular, the Doppler centroid f_{DC} is defined as the Doppler frequency at which the target passes through the center of the antenna beam,

$$f_{DC} = \frac{2v_{\text{sat}}\sin\theta_{\text{s}}\sin\theta}{\lambda}, \tag{3.14}$$

the squint angle θ_{s} gives the pointing direction of the antenna and is measured with respect to the axis perpendicular to flight direction, see geometry in fig. 3.2B.

Equations (3.6) and (3.13) show that the topographic and the range subpixel position components, they both depend linearly on the perpendicular baseline; therefore, they cannot be individually estimated. Since the contribution of the subpixel position in range is usually smaller than the topographic contribution, the term η is often neglected. For example, the contribution to the phase of 10 m topography will be approximately 2.5 times higher than 10 m in the subpixel position in range. In the rest of this study, we will use subpixel position to refer only to the azimuthal component.

Orbital errors

The term Φ_{orb} in eq. (3.2) is produced by orbital inaccuracies. Precise orbital information is required in InSAR processing to determine the baseline vector. Equation (3.4) implies that errors in the state vectors can affect directly the calculation of reference phase Φ_{ref}.

Inaccurate reference phase can be wrongly interpreted as other large scale signals such as deformation or atmosphere. A common approach for eliminating the residual reference phase due to orbital errors approximates this contribution as a spatial plane and subtracts it from interferometric phases, (Biggs et al., 2007; Bähr and Hanssen, 2010). Any other long wavelength signal will be also subtracted with this method.

In addition to that, erroneous orbits can also propagate to errors in the estimated height (Hanssen, 2001), because the contribution of topography also depends on the relative position between master and slave, see eq. (3.6).

Atmospheric delay

The term Φ_{atm} is the atmospheric delay difference between master and slave images. The atmospheric signal, mainly caused by variations in the ionosphere (50-2500 km height) and the troposphere (from 0-25 km height), usually is a strong contribution to the phase and limits the ability of conventional InSAR to measure surface displacements. Atmospheric delay can be divided into two categories depending on its spatial variability: long (>50 km) and short (<10 km) wavelength signals. The long wavelength part can be attributed to the ionosphere and changes in the troposphere concerning the temperature and pressure (Hanssen, 2001; Puysségur et al., 2007; González and Fernandéz, 2011). Long wavelength atmospheric signals have an impact in the interferograms similar to orbital errors. In fact, they cannot be disentangled and they are usually jointly removed from interferograms by

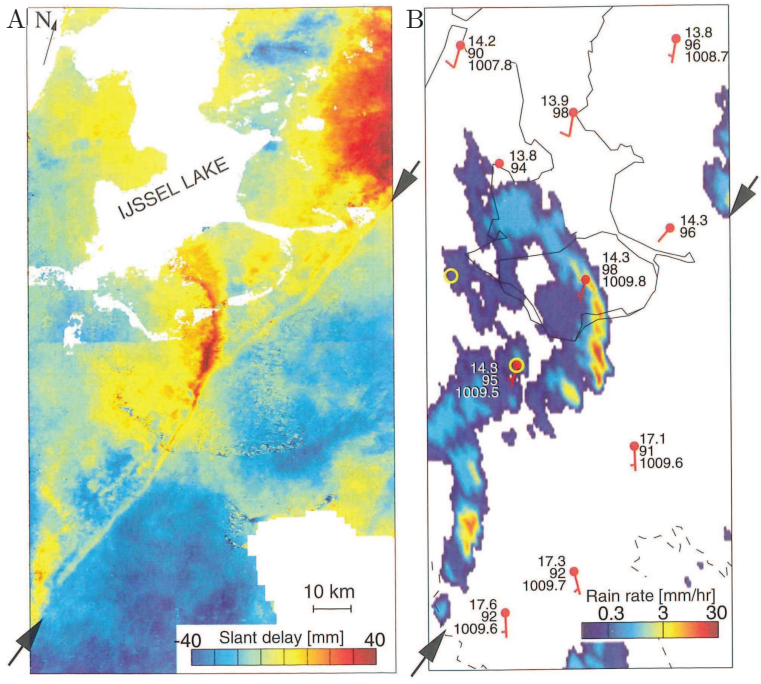

Fig. 3.4. The atmospheric delay observed with InSAR is compared with the weather radar data (from Hanssen (2001)). (A) SAR Interferogram acquired over the northern Netherlands (3 and 4 Oct 1995 21:41 UTC). White spaces represent areas with no data or very low coherence. The boundary of a cold front is marked with black arrows. (B) Weather radar image from 4 Oct 1995 21:45 UTC .

fitting a spatial plane to the phases. Hence, in this dissertation we use the term atmospheric signal (delay) to refer only to the short wavelength component.

The short wavelength atmospheric signal observed in interferograms is caused by variations of the water vapor (Hanssen, 2001; Puysségur et al., 2007). This spatial behavior can be described with the spectral power which corresponds with the [-2/3, -8/3, -5/3] power law, for short (0.01 km–0.5 km), medium (0.5 km–2.0 km) and large distance (> 2.0 km), respectively (Hanssen, 2001). In any case, the correlation of the atmosphere at distance greater than 2.0 km is expected to be low(Hanssen, 2001). In addition to that, if the area contains significant topography, there is further variation that depends on the elevation usually linearly, referred to as vertical stratification (Hanssen, 2001; González and Fernandéz, 2011).

An example of an interferogram displaying atmospheric variation caused by water vapor differences is shown in fig. 3.4A, (Hanssen, 2001). The SAR images were acquired in the so-called ERS tandem mode with only one day time difference. Figure. 3.4B displays the weather data acquired almost at the same time as the slave image (Hanssen, 2001). Comparing figs. 3.4A and B, we see that the cold front measured with the weather data is also visible in the interferogram.

Scattering variations

The term Φ_{scat} represents the changes in the scattering mechanisms of a resolution cell. These changes produce random variations in the signal travel path, which translate into loss of correlation between master and slave. Consequently, the noise of the interferogram increases.

Coherence is a measure of the correlation between two SAR images. The definition of coherence for a given pixel is given by (Just and Bamler, 1994; Bamler and Hartl, 1998)

$$\gamma = \frac{E\{MS^*\}}{\sqrt{E\{A_M^2\}E\{A_S^2\}}}, \tag{3.15}$$

where we use the same nomenclature as in eq.(3.1) and E refers to the expectation operator. In this definition, the coherence is complex-valued. In practical situations, coherence is calculated under the assumption of ergodicity, exchanging ensemble averages with spatial averages (Bamler and Hartl, 1998). The magnitude of the coherence $|\hat{\gamma}|$ is then estimated using a window of K pixels

$$|\hat{\gamma}| = \frac{|\sum_{k=1}^{K}(M_k S_k^*)|}{\sqrt{\sum_{k=1}^{K}(A_{M,k})^2 \sum_{k=1}^{K}(A_{S,k})^2}}. \tag{3.16}$$

Changes in the scattering mechanisms of a resolution cell reduces coherence. The main sources of decorrelation, i.e., loss of coherence, are usually caused by physical changes in the terrain and changes in the local incidence angle θ_{i}, see geometry in fig. 3.2A, and they are referred to as temporal and geometric decorrelation, respectively (Zebker and Villasenor, 1992; Massonnet and Feigl, 1998; Hanssen, 2001).

Decorrelation can also be caused by changes in the squint angle, θ_s in fig. 3.3, also referred to as Doppler centroid decorrelation. Loss of coherence due to processing errors and system noise is described in the next section. If the term Φ_{scat} totally dominates the phase, see eq. (3.2), the coherence magnitude is near zero and the phase is said to be decorrelated.

Examples of areas affected by decorrelation can be seen in the interferogram of fig. 3.1. The noise of the area marked with a rectangle in fig. 3.1 is probably related to temporal decorrelation. The devastating earthquake that occurred in BAM, Iran, in 2003 destroyed many buildings. The scattering mechanisms of these pixels therefore changed between acquisitions, which caused decorrelation. Other areas in the interferogram were also affected by decorrelation, as can be seen, for example, in the lower-left and the upper-left corners of the figure.

Noise

The term Φ_{noise} represents system and InSAR processing noise, such as thermal noise and noise due to coregistration and interpolation errors. We can measure their contribution in terms of loss of coherence.

Thermal noise is a white noise that is produced by the thermal excitation of the electrons in electronic devices. This sets the upper limit on phase accuracy. The influence of thermal noise reduces the coherence magnitude from ideally 1 to $\sim$0.97 for strong scattering objects, (Hanssen, 2001).

Coregistration errors can be produced by rough topography and large perpendicular baselines (Nitti et al., 2010). Hanssen (2001) showed that a coregistration accuracy of 0.1

resolution cell resulted in a coherence magnitude of approximately 0.96 when for perfect alignment the coherence is 1.

Interpolation errors produced during resampling of slave in the master geometry can also cause loss of correlation (Bamler and Hanssen, 1997). This noise translates into coherence magnitude of around 0.999 (Hanssen, 2001). The total noise introduced by these sources—thermal electronic vibrations, coregistration and interpolation errors —is usually low compared with other decorrelation contributes, namely geometric and temporal decorrelation.

3.2.2 Limitations of conventional InSAR

In conventional InSAR, the interferograms are treated individually. In order to estimate the parameters of interest, interferometric phases must be first unwrapped. Even in an ideal situation where the interferograms are perfectly unwrapped, the model given by eq. (3.2) is rank deficient: the number of unknowns is higher than the number of observations. If interested on estimating elevation or surface displacements only, some of the spurious terms can be removed by planning in advance the satellite configuration or using external information. The rest of the contributions, other than the parameters of interest, are then treated as noise.

For topographic estimations, the ideal satellite configuration is obtained when both acquisitions are acquired simultaneously and the relative position is very accurately known. In this case, most of non-topographic related terms of eq. (3.2) cancel. For example, the terms Φ_{atm} and Φ_{defo} that depend on the differences on atmospheric conditions and surface displacements between observations are equal to zero because the acquisitions are simultaneous. However, apart from missions specifically dedicated to topography estimation, such as SRTM (Farr et al., 2007) or TanDEM-X (Moreira et al., 2004), the time interval between acquisitions usually ranges from 11 days to five weeks, mission dependent.

When studying surface displacements with conventional InSAR, most of the topographic phase is removed using an external digital elevation model (DEM). However, the topographic component is never perfectly subtracted because of DEM inaccuracies or errors in the projection of the height on the satellite geometry. The residual topography is usually in the order of tens of meters, although this is case dependent. The noise introduced by the residual topography can have more or less impact on the estimations depending on the acquisition configuration. For example, for Envisat whose sensor wavelength is 5.6 cm, an incidence angle of 23°, a $B_\perp$ of 100 meters, and 10 meters of residual topography result in a equivalent of 0.3 cm of extra noise for deformation estimation.

Apart from the influence of residual topography, surface displacement estimations can still be affected by other error sources produced by misregistration, erroneous resampling, inaccurate orbital information, decorrelation or atmospheric delay. From the previous list, decorrelation and atmospheric delay are often the error sources that can compromise the most the quality of an interferogram.

Decorrelation noise limits the ability of InSAR to measure deformation and can severely affect phase unwrapping. Phase unwrapping is performed in conventional InSAR by integrating the wrapped 2-D gradients, see section 3.5. This operation naturally requires coherent observations otherwise the integration and the consequent unwrapped phase will be wrongly estimated. Each erroneous cycle introduces a jump of 2π radians equivalent to half the sensor wavelength. For C-band satellites, an error of one phase cycle is equivalent to 2.8 cm of surface displacement error.

In addition to that, atmospheric delay is also another major limiting factor when estimating surface deformation with InSAR. This is due to two main reasons. First, the contribution of the atmosphere to interferometric phases is large, normally in the order of centimeters over 100 km. Second, atmosphere and surface displacement can be difficult to disentangle, because they are both spatially correlated.

Therefore, conventional InSAR is usually employed to study phenomena where the expected deformation is higher than the atmospheric variability and that occurs at short time spans. For example, conventional InSAR is widely used in the analysis of earthquakes, magmatic activities, flow of glaciers, and intensive water extraction, see for reference Massonnet et al. (1994); Mattar et al. (1998); Wright et al. (2001); Hoffmann (2003); Calais et al. (2008).

In summary, conventional InSAR has three major limitations when applied to study surface displacements: rank deficiency, low coherence interferograms and the effect of atmospheric signals. To overcome these limitations time series analysis techniques were developed in the late 90's. In the following sections, we describe one of the most relevant time series analysis methods, known as Persistent Scatterer Interferometry (PSI), with especial focus on the Delft implementation, DePSI.

3.3 Overview of Persistent Scatterer Interferometry (PSI)

PSI methods analyze a *stack*[1] of interferograms to extract the information of interest, such as ground displacements or heights. The interferogram data set is created using one single reference or master image, which is selected by minimizing both temporal and perpendicular baselines to increase coherence.

SAR images are analyzed with the goal of detecting pixels that remain coherent in time, i.e. their radar returns are not (or just slightly) affected by noise. The utility of such pixels to overcome InSAR limitations was originally recognized in the late 90's by Usai (1997), Usai and Hanssen (1997) and Usai (2001). Subsequently, Ferretti et al. (2000) and Ferretti et al. (2001) developed a full framework for extracting information from these coherent pixels, which has been further expanded by, for example, Colesanti et al. (2003), Kampes (2006), van Leijen et al. (2006), Crosetto et al. (2008) or Ketelaar (2009). Other PSI algorithms have also been developed in different directions, see, e.g., Hooper et al. (2004).

Pixels that remain coherent over the whole time series are referred to as persistent scatterers (PS). PS pixels are usually related to resolution cells that are dominated by a single scatterer. Since the radar wave reflected by a pixel is the coherent sum of the scatterers found within a resolution cell, if dominated by one scatterer the radar returns are less likely to suffer from temporal and geometric decorrelation. Their phases appear stable in time. PS are usually man-made objects such as buildings or bridges, but other natural reflectors e.g. rocks can also behave coherently, (Usai, 2001).

The opposite situation, i.e. when there is not a prevalent reflector in the resolution cell, is referred to as distributed scattering. In a distributed scatterer pixel, changes between the reflectors due to relative movement or different look angle give rise to random phase variations and the consequent loss of coherence.

Figures 3.5A and B show an example of a decorrelating distributed scatterer pixel and its corresponding phase. In this case there is not a dominant scatterer and all objects

[1] In this dissertation, the term *stack* refers to *data set*, and does not involve any operation, e.g., a stack of single master interferograms, is a data set of interferograms formed w.r.t. a single master image. Both terms *stack* and *data set* are used interchangeably in this book.

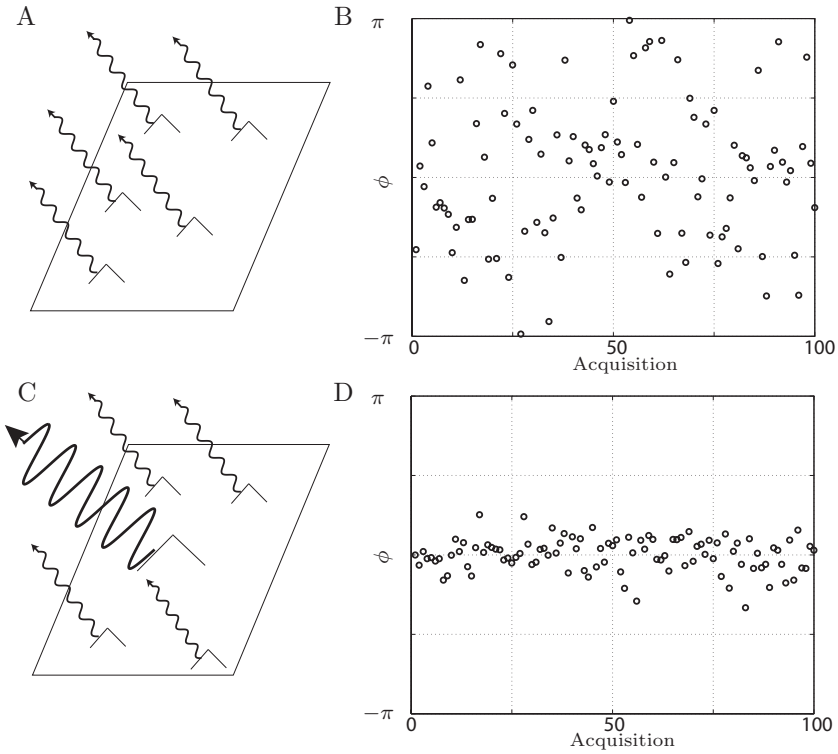

Fig. 3.5. A) Ideal representation of the reflections of a distributed scatterer pixel B) Phase simulation of a distributed scatterer. Decorrelation was simulated by assuming that one scattering object within the resolution cell was stable and the rest changed randomly. C) Ideal representation of the reflections in a resolution cell dominated by one stable scatterer, i.e. a PS pixel. D) The phase was simulated with a stable scatter with amplitude five times higher than the rest (with random phase) scatterers, (modified after Hooper (2006).)

reflect the same amplitude. Decorrelation was simulated by assuming that one scattering object within the resolution cell was stable and the rest changed randomly. The cartoon in fig. 3.5C represents a resolution cell with a dominant reflector, which was simulated with a brightness five times higher than the rest of the scatterers occupying the same resolution cell. Figure 3.5D shows the phase of this pixel, which is clearly more stable than 3.5B.

The temporal analysis of PS pixels constitute the basic principle of PSI methods to overcome conventional InSAR limitations. PSI uses the noiseless nature of PS pixels and their temporal information for parameters estimation, in particular to facilitate phase unwrapping. Atmospheric signal are mitigated by analyzing unwrapped phases in time. Finally, the data stack assures that the number of observations, i.e., unwrapped phases per PS, is larger than the number of unknowns, i.e., displacements and heights; therefore, the system becomes overdetermined and the parameters of interest can be safely estimated.

Apart from PSI, other time series analysis techniques, such as the small baselines (SB)

approach, have been developed. SB methods attempt to diminish decorrelation by selecting those image combinations with short time intervals and small perpendicular distances. SB methods are beyond the scope of this research. For a detailed description, the reader is referred to Berardino et al. (2002) and Mora et al. (2002), and to Hooper (2008) for a combination of PSI and SB methods.

In the following sections, the most relevant steps of PSI algorithms are revisited focusing on the technique used as reference: Delft implementation of PSI (DePSI).

3.4 DePSI

DePSI (van Leijen et al., 2006; Ketelaar, 2009) is the technique employed in this research as reference. This algorithm uses a set of single-master interferograms to estimate deformation time series. The flowchart of fig. 3.6 represents the main processing steps of the algorithm, assuming the interferograms are already computed. The processing chain, which is further elaborated in the following sections, includes PS selection, first order network construction, variance component estimation, first order network phase unwrapping, ramps and atmospheric phase screen (APS) estimation, network densification and the estimation of the parameters of interest. DePSI is based on the spatio-temporal unwrapping network (STUN) algorithm (Kampes, 2006).

3.4.1 PS selection

PS are detected by searching for pixels that are slightly affected by noise throughout the whole time series.

Ferretti et al. (2001) propose the normalized amplitude dispersion D_a to measure phase variability, and thus to detect stable pixels. Ferretti et al. (2001) show that for high signal to noise ratio (SNR) the phase standard deviation σ_ϕ is related to the normalized amplitude dispersion D_a as follows

$$\sigma_\phi \approx \frac{\sigma_a}{\mu_a} = D_a, \tag{3.17}$$

where σ_a and μ_a are standard deviation (square-root of the amplitude dispersion) and the mean value of the amplitude, respectively. Effectively, large variations in the observed amplitude (D_a is high) imply that the reflections inside a resolution cell add up differently in each acquisition. High D_a values therefore indicate a pixel governed by clutter with noisy phase. This is the situation depicted in fig. 3.5B. On the other hand, stable amplitude overtime, low D_a, is produced in a resolution cell that is dominated by one single scatterer with the consequent stability in phase, as shown in fig. 3.5D.

Another method for PS detection is proposed by Adam et al. (2004). This method employs the signal to clutter ratio (SCR) rather than the amplitude dispersion, where the clutter noise is estimated from the surrounding pixels.

The phase variability is related to SCR as follows

$$\sigma_\phi \approx \frac{1}{\sqrt{2\mathrm{SCR}}}. \tag{3.18}$$

Therefore, high SCR is indicative of low-noise pixels.

In the DePSI approach, the selected PS (with D_a or SCR) are divided into two categories:

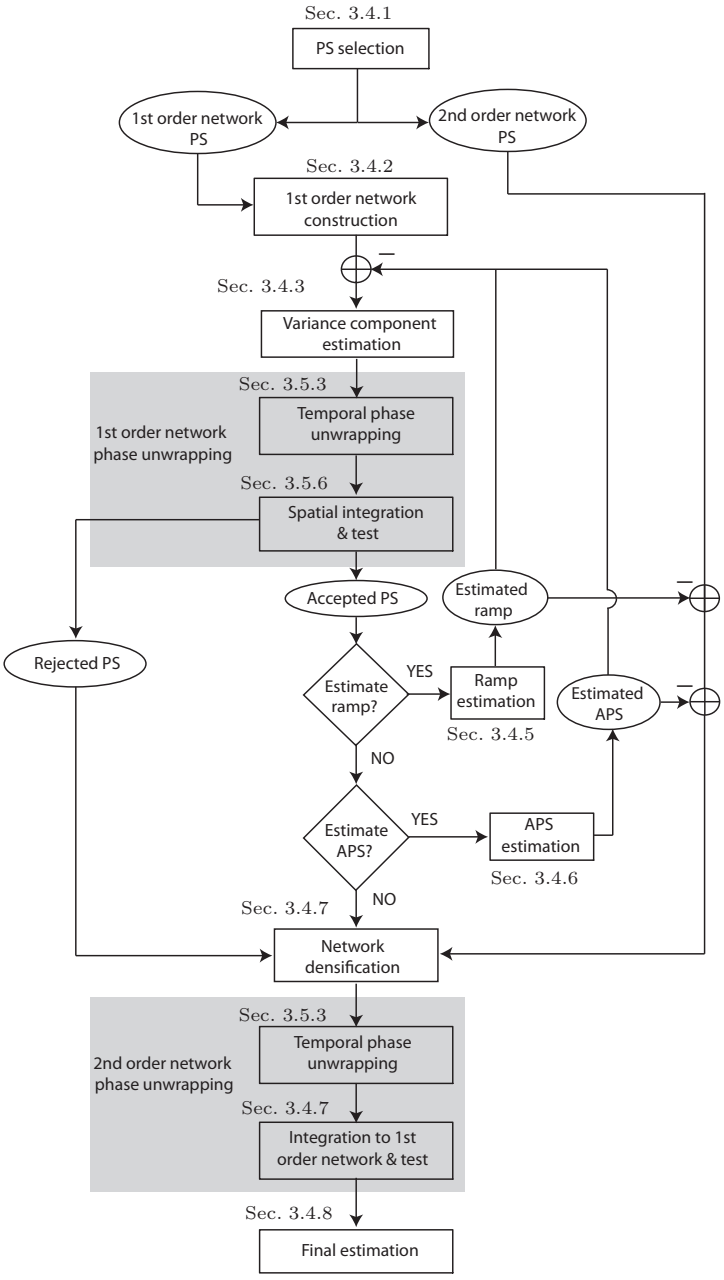

Fig. 3.6. Main processing steps of DePSI. Rectangles represent processes and ovals represent data. Complex processes with more than one output or subprocesses are represented with a gray rectangle.

first and second order network PS. The first order network is formed using very phase-stable pixels and used as reference network for the second order network adjustment and estimation.

For selecting first order network PS, the master image is divided into a uniform grid, of grid size, e.g. 400 m. Then, after detecting the most stable PS of the stack, for example with a amplitude dispersion below 0.25, the most coherent PS per grid cell is categorized as first order network PS. The goal of this strategy is to produce a homogeneous distribution of first order network PS. However, the number of first order network PS is usually limited because the posterior adjustment of this network is a CPU expensive operation.

The second order network includes the rest of detected PS also those with a slightly higher phase variability by relaxing the selection threshold; for example an amplitude dispersion threshold of 0.4 is commonly used. The value of this threshold is case dependent mainly conditioned to the number of available images.

In the PS selection process, DePSI also attempts to remove side-lobe pixels. Side-lobes are reflections that belongs to a neighboring pixel but extents spatially due to the strength of a scatterer. Hence, the inclusion of side-lobes pixels in posterior analysis could lead to erroneous spatial interpretations. DePSI detects them based on distance and temporal correlation to strong scatterers (Perissin, 2006).

3.4.2 First order network construction

After detecting first order network PS, the network is built by interconnecting these PS using, for example, Delaunay triangulation, although other strategies e.g. more redundant networks (Kampes, 2006) have also proved to be efficient. In the redundant network approach, PS are connected uniformly in all directions up to a maximum number of arcs, which forms a spider web–like network. Arcs longer than the expected atmospheric or deformation decorrelation distance (usually from 1 km to 4 km) are rejected.

After the network is built, the phase differences between the PS spanning an arc are used as input for later processing. These observations are also referred to as double differences, because they represent the difference in time, with respect to the master image, and in space, between the PS spanning the arc.

3.4.3 Variance component estimation

The variance component estimation (VCE) method applied in DePSI aims at estimating the noise variance of each interferogram (Kampes, 2006). The estimated variance is then used during phase unwrapping to weight the observations. The VCE process employs the arcs of first order network that have no common PS and are distributed uniformly over the scene. Once these arcs are unwrapped in time and the parameters of interest estimated, the variance is calculated from the least squares residuals $\hat{e} = \Phi - \hat{\Phi}$, (Teunissen, 1988; Amiri-Simkooei, 2007), where Φ and $\hat{\Phi}$ are the observed and modeled phases, respectively. In this method, the variance covariance matrix of the observations Q_Φ is decomposed using the cofactor matrix Q_k:

$$Q_\Phi = \sum_{k=1}^{p} \sigma_k^2 Q_k. \tag{3.19}$$

The cofactor matrix Q_k is built using a priori information. For example, if we assume that the interferograms are uncorrelated, then Q_k is a diagonal matrix.

The estimator of the variance vector of N interferograms $\sigma = [\sigma_1, ..., \sigma_N]^T$ is given by (Amiri-Simkooei, 2007; Kampes, 2006)

$$\hat{\sigma} = R^{-1} r \tag{3.20}$$

The matrices R and r are given by

$$R_{lk} = tr(Q_\Phi^{-1} P_B^\perp Q_k P_B^\perp Q_l) \; ; \; r_k = \hat{e}^T Q_\Phi^{-1} Q_k Q_\Phi^{-1} \hat{e} \tag{3.21}$$

The subscript kl indicates the row k and column l, $P_B^\perp$ is the orthogonal projector :

$$P_B^\perp = I - B(B^T Q_\Phi^{-1})^{-1} B^T Q_\Phi^{-1}, \tag{3.22}$$

being B the design matrix defining the functional model and I the identity matrix.

The dispersion of the estimate $\hat{\sigma}$ is given by (Amiri-Simkooei, 2007; Kampes, 2006)

$$D\{\hat{\sigma}\} = 2R^{-1}. \tag{3.23}$$

The final estimate for the variance component of an interferogram is determined by the mean of all estimated variances of the arcs in this interferogram, which reduces the estimate dispersion (Kampes, 2006).

3.4.4 First order network phase unwrapping

In order to estimate surface displacements, interferometric phases need to be unwrapped, i.e./ the following equation needs to be solved

$$\Phi = \phi + 2\pi a, \text{ with } \phi \in [-\pi, \pi), \Phi \in \mathbb{R} \text{ and } a \in \mathbb{Z}. \tag{3.24}$$

In the reference technique, phase unwrapping is carried out in the spatio–temporal domain, (van Leijen et al., 2006). This means that the arcs forming the first order network are initially unwrapped in time. Then, the number of cycles a estimated during phase unwrapping are tested and adjusted spatially to a common reference point. Arcs that are identified to be outliers are removed from the network, which could leave PS with no connections. Individual PS are also checked by testing simultaneously all arcs connected to it. PS that do not pass the test or are isolated are degraded to the second order network. Spatio–temporal phase unwrapping is discussed in detail in sections 3.5.2, 3.5.3 and 3.5.6.

3.4.5 Phase ramp estimation

An inaccurate location of the satellite translates to an error in the computation of the reference phase, see section 3.2.1. It therefore scales with the distance between the master and slave position. In an interferogram, orbital errors can usually be approximated by a spatial ramp. At this stage of the algorithm, first order network phases are already unwrapped. Thus, the estimation of a spatial ramp in a interferogram can be carried with a traditional least-square approach.

Let us assume that K first order network PS have finally survived the rejection tests, the functional model to estimate a ramp for interferogram i can be expressed as follows

$$\begin{bmatrix} \Phi_1^i \\ \vdots \\ \Phi_K^i \end{bmatrix} = \begin{bmatrix} az_1 & rn_1 & 1 \\ \vdots & & \\ az_K & rn_K & 1 \end{bmatrix} \begin{bmatrix} s_{az}^i \\ s_{rn}^i \\ c \end{bmatrix}, \tag{3.25}$$

where Φ_k^i (with $k = 1, ..., K$ and $i = 1, ..., N$) is the unwrapped and integrated phase of PS k in interferogram i. The design matrix contains az_k and rn_k, which are the azimuth and range coordinates, respectively. The unknowns are the slopes of the ramp in azimuth s_{az}^i and range s_{rn}^i directions and a constant c^i to account for the fact that all arcs are adjusted with respect to the same reference PS.

However, to remove orbital errors using only a spatial ramp carries the risk of subtracting other long wavelength signals that could be related to deformation. Therefore, in DePSI this is an optional step. If it is carried out, the estimated ramp will be removed and phases rewrapped. Then the initial network is rebuilt followed by phase unwrapping.

3.4.6 Atmospheric phase screen estimation

The phase delay caused by a difference between the atmosphere at master and slave is usually referred to as atmospheric phase screen (APS). In this section, the APS of a interferogram i is denoted as Φ_{atmo}^i.

Once the first order network phases are unwrapped and integrated to a common reference, the parameters of interest, such as deformation rates, can be estimated.
Since the distance between the reference and most the PS is probably large, the deformation could be non-linear. Nevertheless, for simplification we assume that the relationship is linear with v the deformation rate of any given PS with respect to the reference point. The master atmosphere is assumed to produce vertical shift to the arcs time series and estimated by adding an constant c in the functional model of each arc. The other parameter we include in the estimations is the residual topography, Δh. The rest is assumed to be noise:

$$\begin{bmatrix} \Phi^1 \\ \Phi^2 \\ \vdots \\ \Phi^N \end{bmatrix} = \frac{-4\pi}{\lambda} \begin{bmatrix} \beta^1 & B_{\text{temp}}^1 & 1 \\ \beta^2 & B_{\text{temp}}^2 & 1 \\ \vdots & & \\ \beta^N & B_{\text{temp}}^N & 1 \end{bmatrix} \begin{bmatrix} \Delta h \\ v \\ c \end{bmatrix} + \begin{bmatrix} e^1 \\ e^2 \\ \vdots \\ e^N \end{bmatrix}, \tag{3.26}$$

where e^i represents the unmodeled phase of interferogram i and the term β^i

$$\beta^i = \frac{B_\perp^i}{R \sin\theta}. \tag{3.27}$$

The unknowns are solved using best linear unbiased estimation (BLUE). This method is similar to the weighted least square approach with the weights equal to the inverse of variance covariance (vc) matrix of the observations (Teunissen, 2000a). The vc matrix can be assumed to be diagonal, i.e. the observations are uncorrelated. The variance of the observations are estimated using the method described in section 3.4.3.
The residuals, which are the differences between observed and estimated phases ($\hat{e}^i = \Phi^i - \hat{\Phi}^i$), are filtered in time using a low-pass filter to obtain the non-modeled deformation. Based on the assumption that atmosphere is uncorrelated in time, it usually decorrelates in

the scale of hours (Perissin and Prati, 2008), the remaining of subtracting the time-filtered residuals $\hat{e}^i_{\text{filter}}$ to the original residuals $\hat{e}^i$ gives the estimate of slave atmosphere plus noise:

$$\hat{\Phi}^{i,\text{slave}}_{\text{atmo}} + \Phi^i_{\text{noise}} = \hat{e}^i - \hat{e}^i_{\text{filter}}. \tag{3.28}$$

Subtracting the estimated master atmosphere to eq. (3.28) we obtain:

$$\hat{\Phi}^i_{\text{atmo}} + \Phi^i_{\text{noise}} = \hat{\Phi}^{i,\text{slave}}_{\text{atmo}} + \Phi^i_{\text{noise}} - \hat{c}. \tag{3.29}$$

The APS of interferogram i, $\hat{\Phi}^i_{\text{atmo}}$, is finally estimated by smooth interpolation of $\hat{\Phi}^i_{\text{atmo}} + \Phi^i_{\text{noise}}$ at the location of all detected PS. This is performed with ordinary kriging (Wackernagel, 1995) which removes the noise term Φ^i_{noise} by including a nugget in the variogram estimation.

The estimated APS is subtracted from the wrapped phases of all detected PS. Since atmospheric noise is reduced, the number unwrapping errors are expected to decrease. After removing the estimated APS the initial operations are repeated. Thus, the first order network is re-built, and the arc phase differences (without the estimated APS) are unwrapped and integrated to a common reference, as explained in previous sections.

3.4.7 Network densification and integration

A second order network is created by connecting the remaining PS to the first order network, which has already been adjusted and tested. Second order network arcs are formed by taking double differences with respect to the closest first order network PS. Each of these arcs are unwrapped in time (a detailed explanation of temporal unwrapping is given in section 3.5.3). The spatial integration is performed by assuming that the solutions of the first order PS are deterministic; therefore, the total number of ambiguity cycles of the second order network are calculated by addition. In order to test the unwrapped solution attributed to a second order network PS, different arcs are created for this PS and unwrapped using other nearby first order PS. The redundant information (e.g., if the PS is connected at three locations we have three solutions) is use to detect incoherent second order PS. Effectively, the integration of the estimated ambiguity cycles should be path-independent. This test can be used to remove inconsistent PS, i.e. PS whose unwrapping solutions are path-dependent.

3.4.8 Final estimation

In the final estimation step, we estimate the parameters of interest. At this stage, first and second order network phases are already unwrapped with respect to a common reference PS. Therefore, the parameters of interest can be estimated using least squares.
Time series of surface displacements are obtained by modeling and removing phase contributions others than deformation, such as, subpixel position and residual topography. Complex deformation models can be estimated and linked to natural phenomena, for example, describing seasonal movements.
The noise of the estimated time series is in principle small. The decorrelation noise can be assumed to be low, because PS are stable pixels. The contribution of the unmodeled atmospheric signals and orbital ramps is expected to be small as well. Previous studies (Marinkovic et al., 2008) have measured a 1-σ precision of $\sim$ 2.8 mm and $\sim$ 1.6 mm for the satellites ERS2 and Envisat, respectively, after applying PSI to a set of a corner reflector

and comparing the results with leveling data. These values were obtained in a controlled experiment and reflect the precision of ideal PS with very reduced atmospheric signals.

However, this is not always the case, and further pixel rejection is sometimes needed to be performed, for example, based on the estimated coherence or variance, or other parameter that reflect the quality of a PS such as the spatio-temporal consistency (STC) (Samiei-Esfahany, 2008; Ketelaar, 2009). STC compares the temporal behavior of a given PS with its surrounding PS. The STC of pixel l with K nearby PS is defined as,

$$\mathrm{STC}_l = \min_{k=1,..,K} \sqrt{\frac{1}{N-1}\sum_{i=1}^{N}(\Phi_l^i - \Phi_k^i)^2}, \tag{3.30}$$

where Φ_l^i and Φ_k^i are the unwrapped phases of PS l and k for interferogram i and N the number of interferograms.

The maximum distance at which PS k are selected depends on the signal of interest, i.e., surface displacements. A minimum distance is also used to avoid including side-lobes in the estimation of the STC. Compared its neighbors, if there exist large differences in the behavior of a PS the estimated STC is large (e.g. 8 rad^2); this PS is assumed to be phase-unstable and is rejected.

3.5 Phase unwrapping

We already discussed in section 3.2.1 that phases are only known as the 2π-modulus of the absolute phase Φ. Phase unwrapping is the process of estimating the number of cycles a the phase is wrapped into. Recalling eq. (3.3), the relationship between unwrapped Φ and wrapped ϕ phases is given by:

$$\Phi = \phi + 2\pi a, \text{ with } \phi \in [-\pi, \pi),\ \Phi \in \mathbb{R} \text{ and } a \in \mathbb{Z}. \tag{3.31}$$

Phase unwrapping is not a trivial operation and cannot be solved unless extra information is included in the problem. For example, PSI techniques usually include a model to describe the temporal behavior of the phases.

3.5.1 Phase unwrapping in conventional InSAR

In conventional InSAR, the interferograms are unwrapped individually. Phase unwrapping is performed by integrating wrapped phase gradients in the spatial dimension under the assumption that the absolute phase difference between neighboring pixels is generally less than π (Goldstein et al., 1988; Ghiglia and Pritt, 1998). This assumption is here referred to as the continuous-phase criterion. The most basic evaluation of the continuous-phase criterion is performed by summing up the wrapped phase differences of neighboring pixels in a closed loop. Non-zero results are called residues, and indicate a violation of the continuous-phase criterion. Lines of gradients greater than π necessarily run between residues of opposite signs (Chen and Zebker, 2000). In order to perform phase unwrapping, residues of opposite signs are connected (unloaded) by minimizing a cost function, e.g. the L^p-norm of the differences between gradients of unwrapped and wrapped phases, (Goldstein et al., 1988; Ghiglia and Pritt, 1998; Costantini, 1998; Chen, 2001). The arcs connecting the residues constitute an obstacle through which phase integration cannot be performed.

3.5.2 Phase unwrapping in PSI

In PSI methodologies, phase unwrapping is usually carried out in the time domain. However, other strategies where phase unwrapping is performed in the spatial domain have also been suggested. The stepwise 3-D algorithm of Hooper and Zebker (2007) unwraps first the data in time. This is not the final result of the unwrapping process but it is used to constrain the solution in the other two dimensions, see also (Hooper, 2010).
Temporal phase unwrapping requires a model describing the time behavior of PS phases. Similarly to the spatial case, the continuous-phase criterion for temporal unwrapping consists of assuming that the absolute differences between model and observations is less than π.
The model parameters are obtained by searching in the solution space for the values that maximize a likelihood function that depends on the differences between modeled and observed phases. In order to avoid high phase variations and to simplify the temporal model, the phase differences between nearby PS are used as observations (Colesanti et al., 2003), forming what we called above arcs or double differences. Once unwrapped, the parameters describing the model and the unwrapped phases are integrated with respect to a reference. To avoid the propagation of errors in the integration a combination of temporal and spatial unwrapping strategies was proposed by Kampes (2006) and van Leijen et al. (2006) and referred to as spatio-temporal unwrapping.
Spatio-temporal unwrapping was briefly described when presenting the reference technique in section 3.4. This is a step-wise method where arcs are first unwrapped in time and then adjusted in space. We discuss methods for temporal unwrapping next, in section 3.5.3. The spatial integration is then discussed in section 3.5.6.

3.5.3 Temporal phase unwrapping

Temporal unwrapping requires a model that describes the phase behavior of an arc in time. The initial model given by eq. (3.2) can be simplified by taking into account the next:

1. The reference phase Φ_{ref} is deterministic and can be easily removed.
2. The contributions of APS and orbital errors are in principle small. APS and orbital errors are spatially correlated and arcs are short. Furthermore, an iterative process can be implemented where APS and orbital errors are estimated and removed using time series analysis as described in sections 3.4.5 and 3.4.6. Unmodeled APS and orbital errors are included in a single noise term, which includes also thermal and decorrelation noise.
3. Most of the topographic phase is removed with an external DEM. The residual topography Δh is however included in the model.
4. We do not include the subpixel position component, whose contribution is usually small and considered as noise, in particular for Doppler centroid differences smaller than 500 MHz (Ketelaar, 2009) .
5. Finally, for short arcs the deformation difference between the PS can be approximated with a linear function of time, because surface displacement are assumed to be spatially correlated.

With these assumptions the functional model used for temporal phase unwrapping includes only differences in residual topography and displacement velocity, denoted with Δh, v, respectively between the PS spanning an arc. In addition to that, we also include a constant

value c in the model to account for the master contribution that is present in all interferograms. Let us denote the arc phases, i.e. double differences, to be unwrapped in time as ϕ^i_{lk} with $i = 1, ..., N$, being N the number of interferograms and where the subscript $\{.\}_{lk}$ is used to indicate that the points spanning the arc are PS k and l.

Thus, the functional model for an arc in an interferogram phase becomes:

$$\phi^i_{lk} = -2\pi a^i_{lk} + \frac{-4\pi}{\lambda}\left(\beta^i \Delta h_{lk} + B^i_{\text{temp}} v_{lk}\right) + c_{lk} + e^i_{lk}, \tag{3.32}$$

where e^i_{lk} represents the unmodeled phase of interferogram i, which includes unmodeled slave atmosphere, unmodeled orbital errors and noise, and its expectation is equal to zero $E\{e^i_{lk}\} = 0$.

Including all observations (phase double differences) obtained for an arc, the complete functional model is given by:

$$E\{\begin{bmatrix} \phi^1_{lk} \\ \phi^2_{lk} \\ \vdots \\ \phi^N_{lk} \end{bmatrix}\} = \begin{bmatrix} -2\pi & & \\ & -2\pi & \\ & & \ddots \\ & & -2\pi \end{bmatrix} \begin{bmatrix} a^1_{lk} \\ a^2_{lk} \\ \vdots \\ a^N_{lk} \end{bmatrix} + \frac{-4\pi}{\lambda} \begin{bmatrix} \beta^1_x & B^1_{\text{temp}} & 1 \\ \beta^2_x & B^2_{\text{temp}} & 1 \\ \vdots & & \\ \beta^N_x & B^N_{\text{temp}} & 1 \end{bmatrix} \begin{bmatrix} \Delta h_{lk} \\ v_{lk} \\ c_{lk} \end{bmatrix}, \tag{3.33}$$

where term β^i_x was already defined in eq. (3.27).

The formulation of eq. (3.32) implies a rank deficiency of 3. Effectively, there are N observations and $N + 3$ unknowns per arc (the ambiguity cycle vector a^i_{lk} of size N, plus three parameters Δh_{lk}, v_{lk}, and c_{lk}). The problem is therefore underdetermined, yielding to an infinite number of solutions. Traditional least squares cannot be used and a search in the solution space must always be performed. Three different approaches for temporal phase unwrapping are discussed in the next sections: ensemble coherence maximization, integer least-squares estimation and bootstrapping estimation.

3.5.4 Ensemble coherence maximization

Ferretti et al. (2001) propose to employ the ensemble coherence maximization (Counselman and Gourevitch, 1981) approach for phase unwrapping. The ensemble coherence of arc xy is given by

$$\gamma_{lk} = \frac{1}{N}\left|\sum_{i=1}^{N} \exp(je^i_{lk})\right|, \tag{3.34}$$

where e^i_{lk} is the residual phase, the difference between the observed and the modeled phase, of the ith interferogram and j the imaginary number $\sqrt{-1}$.

The estimates of the residual topography $\hat{h}_{lk}$ and linear deformation $\hat{v}_{lk}$ are obtained from the arguments that maximize γ_{lk}:

$$\begin{bmatrix} \Delta\hat{h}_{lk} \\ \hat{v}_{lk} \end{bmatrix} = \max_{\Delta h_{lk}, v_{lk}} (\gamma_{lk}). \tag{3.35}$$

Therefore a search in the parameter space is needed to be performed. For example, for a possible solution denoted with the superscript m, $\Delta h_{lk}^m, v_{lk}^m$, the value of the residual in the interferogram i is

$$e_{lk}^{i,m} = \phi_{lk}^i - \begin{bmatrix} \beta_x^1 & B_{\text{temp}}^1 \\ \beta_x^2 & B_{\text{temp}}^2 \\ \vdots & \\ \beta_x^N & B_{\text{temp}}^N \end{bmatrix} \begin{bmatrix} \Delta h_{lk}^m \\ v_{lk}^m \end{bmatrix}. \tag{3.36}$$

It is worth notting that the parameter c_{lk} is not required to be included in the model, because a constant value for all residuals does not change the value of the coherence as defined in eq. 3.34.

The general goal of this method is to estimate the unknown parameters through minimization of the wrapped residuals. The residuals are wrapped during the operation $\exp(je_{lk}^i)$. Therefore, this method does not directly estimate the ambiguity cycle term in eq. (3.33), but a can still be determined from the differences between wrapped and modeled phases.

3.5.5 Integer least-squares estimator

Different studies, (see e.g., Kampes and Hanssen (2004); Teunissen (2006)) have recognized the value of the integer least-squares principle applied to InSAR phase unwrapping. In particular, the approach of Kampes and Hanssen (2004) adapts the Least-squares AMBiguity Decorrelation Adjustment (LAMBDA)method (Teunissen and Tiberius, 1994; Teunissen et al., 1995b), first introduced for the estimation of ambiguity cycles in navigation systems, to the PSI framework.

First, for the sake of clarity, let us simplify the notation by writing eq. (3.33) in a compact form:

$$E\{y_1\} = A_1 a + B_1 b, \tag{3.37}$$

where the subscript referring to an arc is dropped and a new one $\{.\}_1$ is used to distinguish observations $\{.\}_1$ from pseudo-observations $\{.\}_2$, which are defined in the next paragraph; y_1 is the vector of observations, i.e. double differences, a and b are the vector of ambiguities (number of cycles) and the vector of parameters of interest, respectively. A_1 and B_1 are the design matrices represented by:

$$A_1 = \begin{bmatrix} -2\pi & & \\ & -2\pi & \\ & & \ddots \\ & & -2\pi \end{bmatrix}, \tag{3.38}$$

$$B_1 = \begin{bmatrix} \beta_x^1 & B_{\text{temp}}^1 & 1 \\ \beta_x^2 & B_{\text{temp}}^2 & 1 \\ \vdots & & \\ \beta_x^N & B_{\text{temp}}^N & 1 \end{bmatrix}. \tag{3.39}$$

The system of equations given in eq. (3.33) is solved by adding new constrains through the pseudo-observations. Pseudo-observations are the expected value of unknown parameters obtained from prior knowledge, usually taken to be zero. The uncertainty of pseudo-observations (expected deviation from prior knowledge) is included in the stochastic model. With the pseudo-observations the system becomes determined:

$$E\{\begin{bmatrix} y_1 \\ y_2 \end{bmatrix}\} = \begin{bmatrix} A_1 \\ A_2 \end{bmatrix} a + \begin{bmatrix} B_1 \\ B_2 \end{bmatrix} b. \tag{3.40}$$

The vector y_2 contains the pseudo-observations. The matrices A_2 and B_2 are the 3×3 zero and identity matrices, respectively.

In this method, not only the functional model of eq. (3.40) but also the stochastic model is included in the estimations. The last one contains the dispersion of the observations and pseudo-observations:

$$D\{\begin{bmatrix} y_1 \\ y_2 \end{bmatrix}\} = \begin{bmatrix} Q_{y1} & 0 \\ 0 & Q_{y2} \end{bmatrix}. \tag{3.41}$$

The variance-covariance (vc) matrix of the observations Q_{y1} is obtained using variance component estimation approach (Kampes, 2006), see section 3.4.3. On the other hand, Q_{y2} contains the deviations of the pseudo-observations with respect to the expected value, and it is based on prior knowledge.

Let us simplified once again the notation used in eqs. (3.40) and (3.41) becoming

$$E\{y\} = Aa + Bb,\ D\{y\} = Q_y, \tag{3.42}$$

where observations and pseudo-observations are grouped into one single vector y and the matrix A_1 is joined to A_2 to compose matrix A, and B_1 is joined to B_2 giving B.

With the functional and stochastic models described above, the integer least-squares estimator method determines a float (non-integer) solution $\hat{a}$ for the ambiguities by solving the partitioned model of eq. (3.42) (Teunissen, 2000b). To estimate the integer solution, $\breve{a}$, the float solutions $\hat{a}$ are first decorrelated in order to optimize the search space:

$$z = Za,\ \hat{z} = Z\hat{a},\ Q_{\hat{z}} = Z^T Q_{\hat{a}} Z, \tag{3.43}$$

where $Q_{\hat{a}}$ is the vc-matrix of the estimate $\hat{a}$ obtained through BLUE (Teunissen, 2000a) and the superscript T means transposition.

In the simple case where the size of $\hat{a}$ is 2×1, decorrelating the float solution means to transform the search space from elliptical to almost circular shape.

The decorrelating matrix Z is constructed iteratively by alternating application of two basic transformation matrices to the vc-matrix $Q_{\hat{a}}$ until the off diagonal terms of this operation converge to a value close to zero (Odijk, 2002).

The integer decorrelated solution $\breve{z}$ is found by minimizing the differences with the float solution:

$$\min_z \|\hat{z} - z\|^2_{Q_{\hat{z}}}, \tag{3.44}$$

which is identical to minimizing, (Teunissen, 1994)

$$\min_{z_i \in \mathbb{Z}} \left(\frac{\hat{z}_1 - z_1}{\sigma_1^2} + ... + \frac{\hat{z}_{N|N-1} - z_N}{\sigma_{N|N-1}^2} \right). \tag{3.45}$$

The system is solved using a sequential conditional least-squares adjustment (Teunissen, 1994). The ith solution is conditioned on fixing previous ambiguities and the bounds of the search space depends on variance of the ith float solution and its correlation with the previous fixed solution. Thus, the estimate $\hat{z}_{i|I}$ is the least-squares estimate of z_i, conditioned on z_j, $j = 1, ..., i-1$. The search for the integer least-squares ambiguities is performed based on the set of bounds:

$$(\hat{z}_{i|I} - z_i)^2 \leq l_i \sigma_{i|I}^2 \chi^2, \text{ for } i = 1, ..., N \tag{3.46}$$

with

$$l_i = 1 - \frac{\chi_{i-1}^2}{\chi^2}, \text{ subject to } \chi_{i-1}^2 = \sum_{j=1}^{i-1} \frac{(\hat{z}_{j|J} - z_j)^2}{\sigma_{j|J}^2}. \tag{3.47}$$

The parameter χ^2 should be large enough to include initially at least one solution.

Summarizing, starting with the first ambiguity, z_1, a set of possible solutions is obtained for z_1 by finding the integers within the given bounds. For each of these initial solutions, another set of possible solutions is found for z_2 by also bounding the search space. In this case, the bounds are obtained using the variance of the float solution $\hat{z}_2$ and its correlation with $\hat{z}_1$. This operation is repeated for the rest of $\hat{z}_i$. From these combinations of possible integer solutions, the estimate $\breve{z}$ is the value that minimizes $\|\hat{z} - z\|_{Q_{\hat{z}}}^2$.

Once the integer least squares vector $\breve{z}$ is found the original ambiguities are calculated with $\breve{a} = (Z^T)^{-1}\breve{z}$.

From the estimated ambiguities, the phases are unwrapped:

$$\breve{y}_1 = y_1 - A_1 \breve{a}. \tag{3.48}$$

In order to solve for the parameters of interest b_1, the functional and stochastic models are expressed using the unwrapped observations $\breve{y}_1$, (Kampes, 2006):

$$E\{\breve{y}_1\} = B_1 b, \; D\{\breve{y}_1\} = Q_{y_1}. \tag{3.49}$$

The parameters of interest $\breve{b}$ are estimated with BLUE:

$$\breve{b} = Q_{\breve{b}} B_1^T Q_{y1}^{-1} \breve{y}_1 \text{ with } Q_{\breve{b}} = \left(B_1^T Q_{y1}^{-1} B_1 \right)^{-1}. \tag{3.50}$$

Arcs whose residuals norm are larger than a selected threshold can be removed as they indicate large noise or erroneous functional model.

Bootstrap estimator

The search process of the LAMBDA approach is time costly. The bootstrap estimator is a more efficient algorithm that was proposed by Kampes and Hanssen (2004) for interferometric phase unwrapping based on the work of Teunissen et al. (1995a). Being similar to LAMBDA, this approach is however simpler. As before, the float solutions of the ambiguities $\hat{a}$ are first decorrelated with eq. (3.43). Then, the first ambiguity z_1 is rounded to

its nearest integer. Once the integer value of the first ambiguity is determined, the float solution of the rest of the ambiguities are re-estimated on the basis of their correlation with the first ambiguity. Subsequently, the second, now corrected, real-valued ambiguity is rounded to its nearest integer. Then, the remaining float solutions are re-estimated and this continues until all ambiguities are estimated. This gives a vector of initial solutions, $\check{z}^{init}$. The bootstrap estimator is then run N times being N the number of ambiguities to estimate. Each time, the integer $\check{z}_i^{init}$ for $i = 1, ..., N$ is increased or decreased one unit depending on the difference with the float solution $\hat{z}_i$. The final solution $\check{z}$ is the one that provides the minimum value for $\|\hat{z} - z\|^2_{Q_{\hat{z}}}$.

The original ambiguities $\check{a}$ are computed from the decorrelated values $\check{z}$ and the phases unwrapped with eq.(3.48). Then, the parameters $\check{b}$ are obtained with eq. (3.50).

3.5.6 Spatial integration

In the spatial integration we distinguish between first order and second order networks.

Spatial integration for the first order network

In the case of the first order network, the ambiguities $\check{a}$ estimated per arc are used as observations and adjusted to a common reference (van Leijen et al., 2006) using BLUE with a vc-matrix given by $Q_{\check{a}}$.

In principle, if all estimated ambiguities were correct, integration could be simply carried out by summation. In practice, misclosures are found due to incorrect estimations, with the risk that they can propagate when integrating the estimated ambiguities through the network. Therefore, erroneous estimations should be detected and taken care of.
The redundancy of the network is used to detect and remove inconsistent arcs using Detection Identification Adaptation (DIA) alternative hypothesis testing procedure, (Teunissen, 2000b; Kampes, 2006). This procedure is as follows, the network is adjusted using as observations the ambiguity cycles $\check{a}$ that are estimated during phase unwrapping. Then, the network is tested as a whole with the Overall Model Test (OMT).

$$\text{OMT} = \hat{e}_a^T Q_y^{-1} \hat{e}_a, \tag{3.51}$$

where $\hat{e}_a$ is the vector of residuals, i.e., difference between original and spatially adjusted ambiguities $\check{a}$. If the OMT is rejected two types alternative hypothesis are specified to identify the cause. First, the one dimensional alternative hypothesis for (conventional) outlier detection which focuses on rejecting arcs that are spatially inconsistent. Second, the alternative hypothesis checks for incoherent PS, where all arcs connected to a point in question are tested simultaneously. In order to decide what is the cause of rejection of the OMT both tests are compared, (Kampes, 2006).

Spatial integration for the second order network PS

For second order network PS, let us recall what we explained in section 3.4.7. Second order network PS are connected to the closest first order network PS. The phase differences between these two PS are then unwrapped in time. In order to test this solution, different arcs are created, i.e. we calculate double difference of the PS in question with respect to other nearby first order PS. These phase differences are also unwrapped in time. The spatial integration of these independent solutions is performed by assuming that the estimated ambiguities of the first order PS are deterministic; therefore, the total number of ambiguity cycles of the second order network are calculated by addition. The redundant information

can be used to detect incoherent second order PS, because the spatial integration should be path-independent.

3.6 Potential improvements to the reference technique

Although DePSI has proved to be a valuable tool for deformation monitoring, see, e.g., Ketelaar (2009); van Leijen and Hanssen (2008); Caro Cuenca and Hanssen (2008); Yue et al. (2008); Perski et al. (2009), the algorithm can still be improved.

A potential area of improvement resides on the optimal use of spatially correlated information, which is not performed in DePSI nor in most PSI algorithms. In the following bullet points, we identify the following potential areas of improvements mostly related to an optimal use of spatially correlated information:

1. Phase variance estimation: The variance component estimation (VCE) method of the reference technique (Kampes, 2006) calculates a posterior variance from the residuals (observed minus modeled phases) of the initial network. This assumes the same variance for all PS in a given interferogram. A more appropriate approach can calculate variances individually. Based on the fact that loss of coherence does not affect equally all areas in a interferogram, we propose to estimate noise variance spatially. The inverse of the estimated variance is used to weight the observations during phase unwrapping.
2. Phase unwrapping: In many cases the parameters defining the temporal model, such as deformation rates, are spatially correlated. This information can be used in phase unwrapping to better constrained the search space.
3. Spatially correlated noise: Atmospheric delay and orbital errors are spatially correlated noise. In the reference technique they are estimated using the first order network and performing spatial interpolation. Although uniformly distributed, this network is sparse due to computer load limitations. A sparse network therefore decrease the quality of the spatial interpolation. We focus on optimizing the algorithm to improve the density of observations to estimate and subtract spatially correlated noise without increasing computer load.
4. Long term monitoring: Since the goal of this research is also to study processes that last longer than satellite life time, this dissertation explores a method to join PS deformation time series obtained from different satellites.

These improvements that we propose are further developed in chapter 4, where we also test the results and compare them with previous methods.

Chapter 4

Improvements to Persistent Scatterer Interferometry

4.1 Introduction

Chapter 3 was dedicated to Persistent Scatterer Interferometry (PSI) techniques with the focus on the Delft implementation of PSI (DePSI). Here, we explore how to optimize these algorithms mainly by exploiting spatially correlated information.

In previous algorithms (Ferretti et al., 2001; Colesanti et al., 2003; Kampes, 2006), the spatial dimension is mostly used for performing consistency checks of the solutions, to estimate atmospheric signals and to simplify temporal deformation models by taking the phase differences between nearby PS. As we will see in this chapter, other spatial information can be extracted and used to improve the estimations.

Section 4.2.1 investigate how to estimate the phase variance spatially, which is then used to weigh observations during phase unwrapping. In section 4.2.2 we present a new phase unwrapping algorithm that estimates spatially the probability density function (pdf) of unknown parameters defining the temporal model. We use this pdf constrain unwrapped solutions.

In section 4.3, we focus on DePSI, the reference technique and we propose an updated version of the processing chain to improve the estimation of spatially correlated noise (e.g., atmospheric signal) and the final densification step.

Since in this research we study deformation phenomena that last longer than satellite lifetime, section 4.4 is dedicated to a method for joining time series obtained from different satellites with the goal of monitoring long term processes.

4.2 Improvements to PSI algorithms

The optimization that we propose for current PSI algorithms focuses on the estimation of the phase variance and on improving temporal phase unwrapping. We present both in the following sections[1].

[1]This study was published in TGARS, see Caro Cuenca et al. (2011)

4.2.1 Phase variance estimation

The variance of phase observations is very valuable information, in particular, for phase unwrapping, because it can help to reduce unwrapping errors. We propose a method that estimates the precision of a PS spatially in order to take advantage of the situations where the stochastic properties (i.e. variance) of noise sources, such as decorrelation noise and alignment errors, can be estimated spatially.

Decorrelation noise, in particular induced by temporal decorrelation can be higher for PS located in areas that are prone to change. For example, the scattering mechanisms of a PS located in a vegetated area are more likely to be disturbed, e.g., by growing vegetation, than for a PS located in a city. Errors in the master-slave alignment can also be spatially correlated, because the coregistration function that maps the slave image in the master geometry is biased towards areas with high coherence, leaving the areas with lower coherence less well mapped.

The inverse of the estimated variance is then used to weigh the observations during phase unwrapping. The incorporation of the precision in the estimation process was already suggested in DePSI, the reference technique (Kampes, 2006) see section 3.4.3. Here, the difference is that we do not assume that all PS in an interferogram have the same variance and we estimate it individually i.e. one value per PS per interferogram. In other methods, the observations are weighed differently, for example using an estimate of the coherence (De Zan and Rocca, 2005). Under the assumption of ergodicity, De Zan and Rocca (2005) estimate coherence spatially using a window of variable size. No distinction between the pixels inside the window was made. In this work, we categorize them based on their temporal behavior.

The algorithm is summarized in the flow chart of fig. 4.1. In a nutshell, the method that we proposed groups PS based on distance and their stochastic properties. We then say that the pixels of a given group *resemble* each other, because they lie at short distance and their noise variances are similar. The variance of PS k in any interferogram i, $(\hat{\sigma}_k^i)^2$, is calculated from the phase noise estimated for the PS that are found to *resemble* PS k. This operation is repeated per interferogram i.
In more detail, the method is as follows. To obtain stochastic properties, we need first to estimate the noise of each PS. The noise of a PS is estimated with a highpass filter (Hooper et al., 2007), which is implemented as follows. The spatially correlated terms such as atmosphere, surface deformation and residual heights are obtained with bandpass filtering of the complex signal of surrounding PS, using spatial averaging that weights observation depending on distance and estimated coherence (Hooper et al., 2007). The highpass filter is then performed by subtracting the filtered phase $\phi^i_{\text{filtered},k}$ from the original phase ϕ^i_k. The result contains the non-spatially correlated (or non-filtered) surface deformation ($d^i_{\text{NSC},k}$) and residual heights ($h_{\text{NSC},k}$). Recalling the relationship between these contributions and interferometric phases that we gave in section 3.2.1, we find the following

$$\mathbb{W}\{\phi^i_k - \phi^i_{\text{filtered},k}\} = \mathbb{W}\{\frac{-4\pi}{\lambda}\left(\frac{B^i_\perp}{R_k \sin\theta_k} h_{\text{NSC},k} + d^i_{\text{NSC},k}\right) + \phi^i_{\text{noise},k}\}, \qquad (4.1)$$

where

- $\mathbb{W}$ is the wrapping operator.
- λ is the sensor wavelength.
- $B^i_\perp$ is the perpendicular baseline between master and acquisition i.

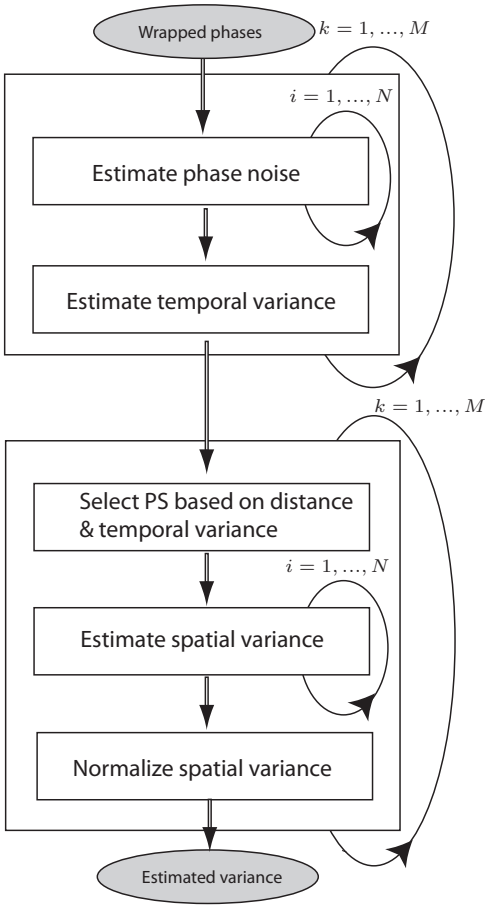

Fig. 4.1. Flow chart of the variance estimation process, where M is the number of PS and N the number of interferograms. First, the noise and the temporal variance is estimated for each PS. Second, the PS are grouped based on distance and similar noise characteristics. Within each group the PS are said to resemble each other. The variance of a given PS is estimated spatially using only the PS resembling each other. The final result is normalized assuming that the mean in time of the spatial variance is equal to the temporal variance. The arrows indicate loops over PS k or interferograms i.

- R_k is the distance from the sensor to PS k.
- $\sin\theta_k$ is the sinus of the look angle θ_k.
- $\phi^i_{\mathrm{noise},k}$ is the noise of interferogram i, which also includes unmodeled phase and is assumed to be small being in the interval of $-\pi$ to π and expectation equal to zero.

Substituting a linear model for non-spatially correlated surface displacements, eq. (4.1) becomes:

$$\mathbb{W}\{\phi^i_k - \phi^i_{\mathrm{filtered},k}\} = \mathbb{W}\{\frac{-4\pi}{\lambda}\left(\frac{B^i_\perp}{R_k \sin\theta_k} h_{\mathrm{NSC},k} + B^i_{\mathrm{temp}} v_{\mathrm{NSC},k}\right) + \phi^i_{\mathrm{noise},k}\}, \qquad (4.2)$$

where B^i_{temp} is the temporal baseline between master and acquisition i and $v_{\text{NSC},k}$ is the rate of non-spatially correlated surface displacements of PS k.

Note that the original method of Hooper et al. (2007) has been slightly modified to include non-spatially correlated displacements in the noise estimation (Schunert et al., 2010).

Although the estimated noise, and therefore the subsequent estimation of the variance, depends on the filter settings, the absolute phase variance is of less importance. The final goal of the algorithm is to weigh observations to aid phase unwrapping. Therefore, the algorithm focuses on estimating the variance factor that gives the relative weight between observations rather than in the absolute phase variance itself.

We can estimate non-spatially correlated residual heights $\hat{h}_{\text{NSC},k}$ and velocities $\hat{v}_{\text{NSC},k}$ using, e.g., coherence maximization methods (Hooper et al., 2007). After removing the corresponding phase components, the remaining phase is our estimate of the noise, $\hat{\phi}^i_{\text{noise},k}$:

$$\hat{\phi}^i_{\text{noise},k} = \mathbb{W}\{\phi^i_k - \phi^i_{\text{filtered},k} - \hat{\phi}^i_{\text{NSC},h} - \hat{\phi}^i_{\text{NSC},d}\}, \tag{4.3}$$

where

$$\hat{\phi}^i_{\text{NSC},h} = \mathbb{W}\{\frac{-4\pi}{\lambda}\frac{B^i_{\perp}}{R_k \sin\theta_k}\hat{h}_{\text{NSC},k}\}, \tag{4.4}$$

and

$$\hat{\phi}^i_{\text{NSC},d} = \mathbb{W}\{\frac{-4\pi}{\lambda}B^i_{\text{temp}}\hat{v}_{\text{NSC},k}\}. \tag{4.5}$$

The value of $\hat{\phi}^i_{\text{noise},k}$ is assumed to be small and to remain within a phase cycle; therefore, it does not need to be unwrapped.

With $\hat{\phi}^i_{\text{noise},k}$ we calculate the temporal variance for each PS, which is used to group nearby PS as explained below. Temporal variability is measured with the variance estimated in time. For PS k this operation is given by

$$\hat{\sigma}^2_{\text{time},k} = \sum_{i=1}^{N}\frac{(\hat{\phi}^i_{\text{noise},k} - \hat{\mu}_{\text{noise},k})^2}{N-1}, \tag{4.6}$$

where N is the number of interferograms and $\hat{\mu}_{\text{noise},k}$ represents the sample mean of $\hat{\phi}^i_{\text{noise},k}$ estimated over time:

$$\hat{\mu}_{\text{noise},k} = \sum_{i=1}^{N}\frac{\hat{\phi}^i_{\text{noise},k}}{N}. \tag{4.7}$$

We can group pixels that resemble each other as follows. We select the PS that lie at short distance with respect to PS k, and whose temporal variance is similar i.e. if the temporal variance difference is smaller than a threshold, T_σ:

$$|\hat{\sigma}^2_{\text{time},k} - \hat{\sigma}^2_{\text{time},l}| < T_\sigma \text{ with } l = 1, ..., m. \tag{4.8}$$

The maximum distance used for selecting PS and the threshold T_σ are obtained assuming that the temporal variance $\hat{\sigma}^2_{\text{time}}$ is stationary at short distances. We estimate a variogram spatially (Wackernagel, 1995) where the observations are $\hat{\sigma}^2_{\text{time}}$ and the location is given by the corresponding PS coordinates. We employ as maximum distance the practical range (three times the actual range of the variogram) that is defined as the distance at which the

covariance function decrease 95% (Wackernagel, 1995). This value is in the order of few km. For the threshold T_σ we take the estimated sill (e.g. 0.06 rad^2).

The PS grouped based on these two criteria are said to resemble each other, and their estimated noise is used to compute the variance spatially. Let us assume that there are m PS resembling PS k. We estimate the variance of PS k in interferogram i, $(\hat{\sigma}_k^i)^2$, with,

$$(\hat{\sigma}^i_{\text{space},k})^2 = \sum_{l=1}^{m} \frac{(\hat{\phi}^i_{\text{noise},l} - \hat{\mu}^i_{\text{noise},k})^2}{m-1} \tag{4.9}$$

where $\hat{\mu}^i_{\text{noise},k}$ represents the sample mean of interferogram i calculated spatially with $l = 1, ..., m$:

$$\hat{\mu}^i_{\text{noise},k} = \sum_{l=1}^{m} \frac{\hat{\phi}^i_{\text{noise},l}}{m}. \tag{4.10}$$

This is repeated for all interferograms to build the vector $\hat{\sigma}^2_{\text{space},k}$ whose length is equal to the number of interferograms:

$$\hat{\sigma}^2_{\text{space},k} = [(\hat{\sigma}^1_{\text{space},k})^2, ..., (\hat{\sigma}^N_{\text{space},k})^2]^T. \tag{4.11}$$

Figure 4.2 shows the histogram of $\hat{\sigma}^2_{\text{time},k}$ obtained from the test area described in section 4.2.4. From the histogram, we can deduce that PS with very high and very low values of $\hat{\sigma}^2_{\text{time},k}$ may not have nearby PS, because their number is very limited. Thus, for PS with low $\hat{\sigma}^2_{\text{time},k}$, the variance is not estimated spatially and $(\hat{\sigma}^i_{\text{space},k})^2$ is taken to be constant for all interferograms and equal to the value of $\hat{\sigma}^2_{\text{time},k}$. In principle, this assumption should not influence phase unwrapping of these PS very much, because they are highly stable in time, i.e., $\hat{\sigma}^2_{\text{time},k}$ is low. On the other hand, for *noisy* PS (high $\hat{\sigma}^2_{\text{time},k}$) with no nearby PS, $(\hat{\sigma}^i_{\text{space},k})^2$ is not calculated at the first instance but computed as the mean of the variances obtained for the rest of the PS.

We correct $\hat{\sigma}^2_{\text{space},k}$ for the noise particular to PS k by assuming that the temporal variance of PS k, $\hat{\sigma}^2_{\text{time},k}$, represents the temporal mean of the variance estimated spatially:

$$(\hat{\sigma}^i_k)^2 = \hat{\sigma}^2_{\text{time},k} \frac{(\hat{\sigma}^i_{\text{space},k})^2}{\sum_{i=1}^{N}((\hat{\sigma}^i_{\text{space},k})^2/N)} \tag{4.12}$$

$(\hat{\sigma}^i_k)^2$ is our final estimate of the variance of PS k in interferogram i, which can also be written in a vector form:

$$\hat{\sigma}^2_k = [(\hat{\sigma}^1_k)^2, ..., (\hat{\sigma}^N_k)^2]^T, \tag{4.13}$$

with N the number of interferograms.

In summary, this method first estimates the noise of each PS. Then it finds PS resembling each other and uses their estimated noise to compute their variance.

Since our observations are the interferometric phases of an arc, we are interested in the variance of the differences of pairs of PS. For a generic arc lk spanning PS k and l, the estimated noise variance $\hat{\sigma}^2_{lk}$ is obtained from the propagation law of variances assuming independence:

$$\hat{\sigma}^2_{lk} = \hat{\sigma}^2_l + \hat{\sigma}^2_k. \tag{4.14}$$

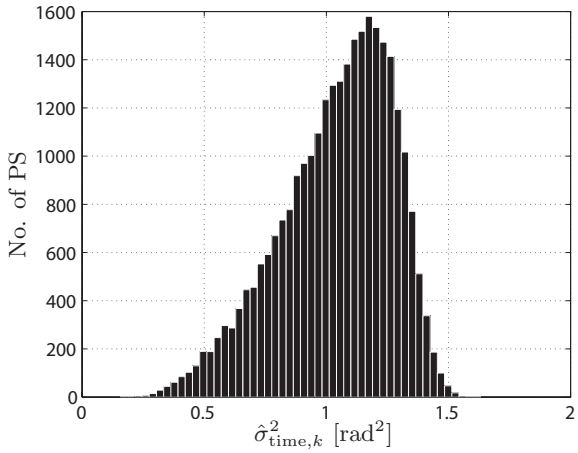

Fig. 4.2. Histogram of the temporal variance $\hat{\sigma}^2_{\text{time},k}$ estimated for the test area described in section 4.2.4.

4.2.2 Phase unwrapping using Bayesian theory

Bayes' rule uses the prior probability of some parameters of interest to estimate the conditional probability of these parameters given a set of observations. The application of Bayesian inference to extract information, namely heights, from interferometric phases was suggested by Eineder and Adam (2005). However, this method requires a priori knowledge of the pdf of the parameters of interest, e.g. heights. A similar approach is here reformulated but with the goal of providing a framework for phase unwrapping of PS time series. The method also estimates the pdf needed to apply Bayes' rule.

Although this is trivially extended to any other model, we start by assuming that the major contributions to the phase of arc lk, ϕ^i_{lk} are:

- The height difference between PS k and l (h_{lk}),
- the displacement difference, which is here modeled as a linear function of time with velocity v_{lk}
- and a constant value c_{lk} to account for the correlation between interferograms, mainly produced because they are computed with respect to the same reference (master) image.

Therefore, ϕ^i_{lk} is given by,

$$\phi^i_{lk} = \mathbb{W}\{\frac{-4\pi}{\lambda}\left(\frac{B^i_\perp}{R\sin\theta}h_{lk} + B^i_{\text{temp}}v_{lk}\right) + c_{lk} + \phi^i_{\text{noise},k}\}, \tag{4.15}$$

with $i = 1, ..., N$ and using the same nomenclature as in eqs. (4.1) and (4.2).

In order to unwrap the phases of arc lk, we search for the values of h_{lk}, v_{lk} and c_{lk} that maximize the conditional probability density function (pdf)

$$\wp(h_{lk}, v_{lk}, c_{lk}|\phi^1_{lk}, ..., \phi^N_{lk}), \tag{4.16}$$

where $\wp$ refers to the pdf and ϕ_{lk}^{i} (with $i = 1, ..., N$) are the interferometric phases of arc lk, also referred to as double differences, of N interferograms. For the sake of clarity, we drop the subscript referring to the arc from now on, and replace it with interferogram number (ϕ_{lk}^{i} becomes ϕ_i). Then, the problem can be stated as follows

$$[\hat{h}, \hat{v}, \hat{c}] = \max_{h,v,c} [\wp(h, v, c|\phi_1, ..., \phi_N)], \tag{4.17}$$

Using Bayes' rule, $\wp(h, v, c|\phi_1, ..., \phi_N)$ becomes:

$$\wp(X|\phi) = \frac{\wp(\phi|X)\wp(X)}{\wp(\phi)}, \tag{4.18}$$

where ϕ is the vector of phase double differences, $\phi = [\phi_1, ..., \phi_N]^T$ and X is the vector of unknowns $X = [h, v, c]^T$.

We ignore the denominator in eq. (4.18), because it does not depend on h, v or c.

The term $\wp(\phi|X)$ represents the pdf of the difference between ϕ and its expected value ϕ_0, which depends on the model parameters $X = [h, v, c]$, see eq. (4.21). Since this difference $e = \mathbb{W}\{\phi - \phi_0\}$ is, in principle, small because it contains mostly thermal noise and slave atmosphere, which is small because phase double differences are taken between nearby PS, we can assume $\wp(\phi|X)$ to be Gaussian distributed:

$$\wp(\phi|X) = C_Q \cdot \exp\left(-\frac{1}{2} e^T Q_\phi^{-1} e\right), \tag{4.19}$$

with

$$C_Q = \frac{1}{\det(2\pi Q_\phi)}. \tag{4.20}$$

Q_ϕ is the variance-covariance (vc) matrix of the observations, i.e. phase double differences, which are assumed to be independent.

Note also that the correlation between interferograms due to the fact that all are with respect to the same master image is not included in the vc-matrix but estimated as the constant term c. Consequently, Q_ϕ is a diagonal matrix whose diagonal elements are the phase variances estimated with our method, described in section 4.2.1. The term ϕ_0 is also a vector $[\phi_1^0, .., \phi_N^0]^T$. Recalling, eq. (4.15), the expected phase ϕ_i^0 for interferogram i is given by:

$$\phi_i^0 = \mathbb{W}\{\frac{-4\pi}{\lambda}\left(\frac{B_\perp^i}{R \sin\theta} h + B_{\text{temp}}^i v\right) + c\}, \text{ with } i = 1, ..., N. \tag{4.21}$$

With the equations above, we therefore define completely $\wp(\phi|X)$ of eq. (4.18). However, the second term numerator of eq. (4.18) $\wp(X)$ needs to be determined. Using a priori information, e.g. from SRTM measurements, we can in principle determine $\wp(X)$ (Eineder and Adam, 2005). However, this type of information is often not available for parameters other than heights. Here, we propose to estimate the pdf of the parameters of interest of an arc lk from the most reliable arcs around it.

Estimation of the pdf

The pdf of the parameters of interest $\wp(X)$ is estimated iteratively. Initially, for a given arc lk we assume $\wp(X)$ to be a boxcar—or rect function—which is constant inside a bounded search space and 0 outside. The search space is limited based on a priori knowledge. Then, we search for the solutions that maximize $\wp(X|\phi)$, see eq. (4.18).

In the second iteration, we build the needed pdf, $\wp(X)$, for each arc from the estimates obtained for nearby arcs. This experimental pdf is determined spatially.

At first instance, we describe the method for only one unknown e.g. heights h. Then, we extend it to include a displacement rate v and a constant c. We use indicator kriging (Wackernagel, 1995) for estimating the pdf of the heights of any given arc. This estimate is denoted as $\hat{\wp}(h)$. The observations of indicator kriging are the estimated heights $\hat{h}$. These values, $\hat{h}$, are compared with a chosen list of thresholds $h_1 < h_2 < ... < h_W$. At a generic arc position p_0, taken as the middle point between the PS spanning the arc, we then evaluate the indicator $I(p_0, h_w)$ for this position and threshold h_w with

$$I(p_0, h_w) = \begin{cases} 1 & \text{if } \hat{h}(p_0) \leq h_w \\ 0 & \text{otherwise} \end{cases} , \tag{4.22}$$

for $w = 1, 2, ..., W$. The indicator $I(p_0, h_w)$ is estimated for all arcs. Then, we determine an indicator variogram from the 0|1 observations. This is used to predict the cumulative density function (cdf), from which the pdf is calculated. First $\hat{I}(p_0, h_w)$ is estimated at position p_0 using ordinary kriging:

$$\hat{I}(p_0, h_w) = \sum_{j=1}^{n} w_{0,j,w} I(p_j, h_w), \tag{4.23}$$

where $w_{0,j,w}$ is the weight of observation $I(p_j, h_w)$ evaluated at p_0 and obtained from the indicator variogram (Wackernagel, 1995). The term n is the maximum number of observations used for the interpolation. Note that $j \neq 0$, i.e. the observation at p_0 is excluded from the pdf estimation.

The cdf estimated at p_0, $\hat{\varsigma}(p_0)$, is then given by

$$\hat{\varsigma}(p_0) = \{\hat{I}(p_0, h_1), \hat{I}(p_0, h_2), ..., \hat{I}(p_0, h_K)\}. \tag{4.24}$$

The derivative of $\hat{\varsigma}$ yields the estimated pdf $\hat{\wp}$. The spacing between the thresholds h_w and h_{w+1} used in eq. (4.22) are usually coarse. The finer step size is solved by 1-D interpolation at the required location. Smoothing of $\hat{\wp}$ may also be needed.

The same operations can be applied to the rest of the unknowns, v and c. Then, $\hat{\wp}(h, v, c)$ is obtained assuming the unknowns are independent:

$$\hat{\wp}(h, v, c) = \hat{\wp}(h)\hat{\wp}(v)\hat{\wp}(c). \tag{4.25}$$

This method determines experimentally the pdf of the parameters of interest, using only the arcs that are reliable unwrapped. A more sophisticated method can also distinguish between the type of reflecting objects (e.g. single and double bounce objects). Then, in the process of determining the experimental pdf, only reliable arcs spanning two PS of the desired category (e.g. single bounce PS) would be considered.

4.2.3 Tests and results of the new methods with simulated data

In the sections above we have presented a method to determine the variance of a PS and the experimental pdf of the parameters governing its temporal model. We have also proposed a method for phase unwrapping that employs Bayesian theory to neglect unlikely solutions through the experimental pdf, and it also uses the estimated variance to weigh the observations, assigning lower weights to those observations that are detected to be noisy. In this section, we test the complete method for phase unwrapping, which therefore means to test simultaneously our estimates of the variance and the experimental pdf.

First we use simulated data, where we compare the simulated (known) solutions with estimated values. Second, we apply the method to actual interferograms and measure the number of accepted arcs after statistical tests. In this section we discuss the results of the simulation. Section 4.2.4 is dedicated to the case where we apply our methods on real data.

For the simulations, we create 20 synthetic interferograms whose phase contains atmosphere, height, and Gaussian distributed noise. To simulate the effect of decorrelation, we simply assign different noise levels to each interferogram.

The total number of pixels was 3136. The interferogram size was equivalent to 200 m in azimuth and 500 m in range direction. All arcs have the same pixel as reference, forming a star-like network. We consider all pixels as PS and did not perform any prior selection.

The atmosphere is simulated as isotropic 2 dimensional fractal surfaces with a power law behavior which corresponds with the [-2/3, -8/3, -5/3] power law, for short, medium and large distance respectively (Hanssen, 2001). The height is simulated assuming a Gaussian pdf (Eineder and Adam, 2005) with standard deviation of 5 meters and zero mean. In the following, we begin by testing our method for variance estimation. Next, we focus on the method for phase unwrapping using Bayesian theory.

Spatial estimation of phase variance with simulated data

To test our method for phase variance estimation, we first unwrap the time series with the Bayesian approach and using as variance our estimated variance, see eq. (4.19). After that, since the actual simulated heights h are known, the number of wrongly unwrapped PS is calculated. We then repeat phase unwrapping but in this case the variance is set equal to 1, i.e., observations are not weighed. We compare the number of unwrapping errors when observations are weighed with $\hat{\sigma}_k^2$ with those when the observations are not weighed. For these two cases, we employ our Bayesian approach for phase unwrapping, which required several iterations for calculating the pdf of the parameters of interest. The results are summarized in tab. 4.1. The number of wrongly unwrapped PS after each iteration (updating the pdf) are always smaller when using the estimated variance than in the case when the observations are not weighed. Even more, four iterations prove to be enough to correct all wrongly unwrapped PS, while in the other case more iterations are needed.

Bayesian phase unwrapping with simulated data

To test our method for phase unwrapping, we create three stacks of 20 interferograms each. Different noise levels are assigned to each stack. The average standard deviation of the stacks are 0.36 rad (low-noise case), 0.47 rad (medium-noise case), and 1.10 rad (high-noise case). As before, unwrapping errors are found by comparing actual heights h with estimated ones $\hat{h}$. For all three interferograms stacks, we start with the same initial pdf. This was a boxcar that is equal to one within the bounds -40 m to $+40$ m and zero outside.

Table 4.1. Number of wrongly unwrapped PS from simulated interferograms. Two cases are compared: when the wrapped phases are weighed with the inverse of the estimated variance $\hat{\sigma}_k^2$, and when the phases are not weighed. The total number of pixels was 3136.

Iteration	weight $=1/\ \hat{\sigma}_k^2$	No weight
0 (pdf=boxcar)	397	790
1 (updated pdf)	34	304
2 (updated pdf)	2	186
3 (updated pdf)	0	139

The results of the test are summarized in tab. 4.2. They show that for the low-noise case only four pixels are wrongly unwrapped and after the first update of the pdf all errors are corrected. More iterations do not alter the results.

For the medium-noise case, the results of tab. 4.2 are complemented with fig. 4.3, where estimated heights are plotted against the corresponding real solution. In these graphs, correctly estimated heights should lay on a line with a slope equal to one, and most of them actually do. Solutions outside the central cluster represent unwrapping errors. Figure 4.3A shows estimated versus real heights when $\hat{\wp}(h)$ is a boxcar. The initial number of 397 wrongly unwrapped PS drop to 34 after a first update of the pdf. This can also be noticed by comparing fig. 4.3A and B. One more iteration reduce again the errors to only two, see fig. 4.3C. Three updates are required to correct them all as shown in fig. 4.3D.

Finally, for high-noise interferograms also major improvements are found after the first iteration. The number of wrongly unwrapped PS reduced from 1129 to 494, see tab. 4.2. Since the total number of pixels was 3136, this demonstrates that the algorithm proves to be efficient even if a third of the estimations are wrong. However, due to high noise, more than four iterations were needed to correct all the wrongly unwrapped PS.

Let us further analyze the results obtained for the medium-noise case. We select a pixel whose height is initially wrongly estimated and corrected after updating the pdf. The initial estimate of this pixel is 40.4 m while the true (simulated) solution is -4.2 m. The corresponding unwrapped phases are plotted against the perpendicular baseline $B_\perp$ in fig. 4.4A. They are shown as black triangles. The solid line represents the modeled phase due to true height (-4.2 m). After estimating $\hat{\wp}(H)$ and including it in the phase unwrapping process, a new height of -4.4 m is obtained, very close to the real value. The corresponding unwrapped phases are shown in fig. 4.4B also as black triangles. The improvement is clear. The differences between the unwrapped and phase due to height are caused by simulated noise and atmosphere.
For the same pixel, we also investigate in fig. 4.5 how the maximum likelihood estimator, see eq. (4.17), performed. In the first run, $\hat{\wp}(h)$ is a boxcar and the solution search is governed by $\wp(h|\phi)$, shown in black in fig. 4.5A. From the graph we see that the most likely value for heights is at 40.4 m, therefore the selected solution. The conditional pdf $\wp(h|\phi)$ also had a local maximum in the neighborhood of the real solution -4.2 m, marked with a dashed rectangle and displayed as a zoom-in. The solution was searched in steps of 1 meter, which produced a discrete $\wp(h|\phi)$. Once a maximum was found, the solution was refined by searching around the maximum in finer steps.

The estimated pdf $\hat{\wp}(h)$ is shown in gray in fig. 4.5A. Then, $\wp(\phi|h)$ is computed applying

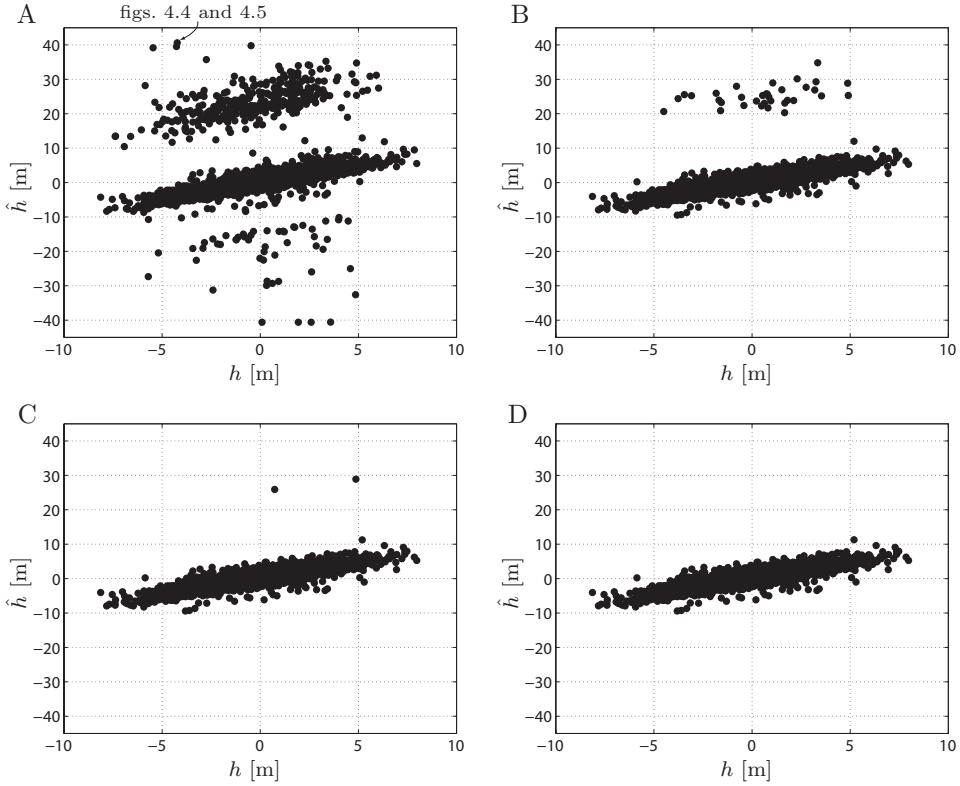

Fig. 4.3. Estimated ($\hat{h}$) versus actual value of the simulated height h for the medium-noise stack. The pixel marked with a thin arrow is further studied in figs. 4.4 and 4.5. (A) Results after first estimation run: the initial pdf $\hat{\wp}(h)$ was a boxcar function. (B) Results after second estimation run: we employed an estimate of the pdf $\hat{\wp}(h)$. (C) Third run, the estimated pdf was updated $\hat{\wp}(h)$. (D) Fourth iteration, $\hat{\wp}(h)$ was updated once more.

Bayes' rule, see eq. (4.18). The resulting $\wp(\phi|h)$ is shown in fig. 4.5B. From this, we obtain the new *corrected* solution of −4.4 m.

Table 4.2. Number of wrongly unwrapped PS for simulations with different noise levels (low, medium and high), see text for explanation. The total number of pixels was 3136.

Iteration	low noise	medium noise	high noise
0 (pdf=boxcar)	4	397	1129
1 (updated pdf)	0	34	494
2 (updated pdf)	0	2	262
3 (updated pdf)	-	0	188

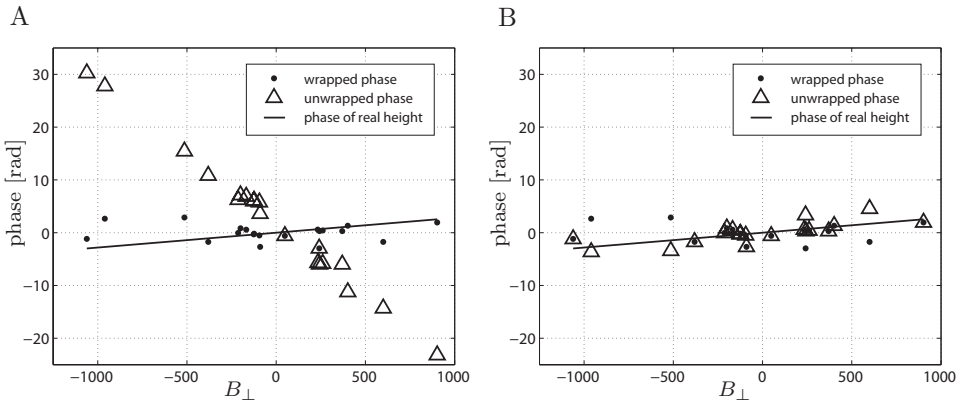

Fig. 4.4. (A) Wrapped and unwrapped phases of a PS whose height was initially wrongly estimated. (B) The unwrapped phase of the same pixel is corrected by updating $\hat{\varphi}(h)$ from a boxcar to the value obtained using indicator kriging. See also fig. 4.5. The phase corresponding to the actual (simulated) height is shown as a solid line.

From the simulations, we conclude that ambiguities estimated erroneously can be corrected using our algorithm.

4.2.4 Tests and results of the new methods with real data

We apply our methods for variance estimation and phase unwrapping to a time series of ERS1/2 images acquired over the Netherlands. We select a small area in the southern Netherlands, that is affected by motion due to water rebound in abandoned coal mines, see chapter 6. The crop we analyze is 15 km×10 km wide and there are at least three different deformation modes: stable areas, and two abandoned mines uplifting at different velocities.

We use the framework of DePSI, which was described in chapter 3. To asses the reliability of our method we study the number of arcs that are rejected by statistical tests. In DePSI, a first order network is built with the most coherent PS. The arcs forming the network are adjusted to a common reference and tested for outliers (Teunissen, 2000b). The goal of this process is to remove spatially inconsistent arcs. Then, a second order network is created by connecting the rest of the PS to the initial network at three different locations, see fig. 4.10A. These three arcs are unwrapped in time and integrated with respect to the initial common reference. Therefore, each second order network PS has three independent solutions. PS with inconsistent—different—solutions are rejected.

Spatial estimation of phase variance with real data

With our method, see section 4.2.1, we estimate the standard deviation of the arcs formed from the PS detected in the test area. The average values per interferogram are plotted against the temporal and perpendicular baseline in fig. 4.6, where the area of the circles scales with the standard deviation. As expected, the variance increased with time and perpendicular baselines, due to temporal and geometrical decorrelation, respectively.

The initial network is composed of 2051 arcs. From this total, the number of accepted arcs is 1909 when we use as variance the value estimated with our method.

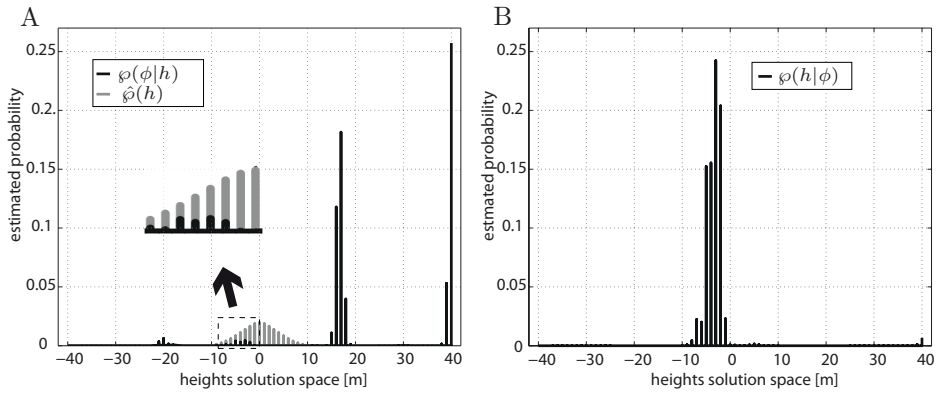

Fig. 4.5. The likelihood of each solution of the selected search space obtained from simulated data. The step search, which was 1 meter, created a discrete distribution (A) For the first run, we assume $\hat{\wp}(X)$ is a boxcar, not shown in the figure. The likelihood of each solution was obtained through $\wp(\phi|h)\hat{\wp}(X)$ and where $\wp(\phi|h)$ is displayed in black. With $\hat{\wp}(X)$ as a boxcar the most likely solution we obtained was 40.4 m. After all PS were unwrapped, we estimated $\hat{\wp}(h)$, shown in gray. The zoom shows also a local maximum in the neighborhood of the real solution (-4.2 m). (B) $\hat{\wp}(h)$ was estimated and incorporated in the estimations with eq. (4.18). The likelihood of each height (displayed in black) changed since $\hat{\wp}(h)$ was not anymore a boxcar. The new $\wp(h|\phi)$ is displayed in black its maximum value gives a new solution of -4.4. m, nearer to the simulated height (-4.2 m).

We compare this number with the results obtained when the variance is estimated using the variance component estimation (VCE) method proposed in (Kampes, 2006), see section 3.4.3. The number of accepted PS using the variance from VCE is 1896. The results are summarized in tab. 4.3. In both cases, we use the Bayesian approach to unwrap the arcs.

We also check the results obtained for the second order network following the same procedure. In the unwrapping process, the observations are first weighed with the variance estimated spatially. Then unwrapping is repeated but now the variance we use is the one obtained in VCE method.

The results of the second order network show that if we weigh the observations using the variance estimated spatially the number of total accepted PS is 5442 and when using the variance estimated with the VCE of Kampes (2006) the number is 5383. Although the differences are not high, the proposed method for variance estimation performed better in terms of accepted arcs and PS.

Bayesian phase unwrapping with real data

We compare the results of our phase unwrapping method with those obtained by the bootstrap estimator (Kampes and Hanssen, 2004) and ensemble coherence maximization (Ferretti et al., 2001) methods, see section 3.5.3. The comparison is performed in two ways. First, we check the number of PS that are accepted by the statistical tests. Second, we inspect the estimated rates of all selected PS.

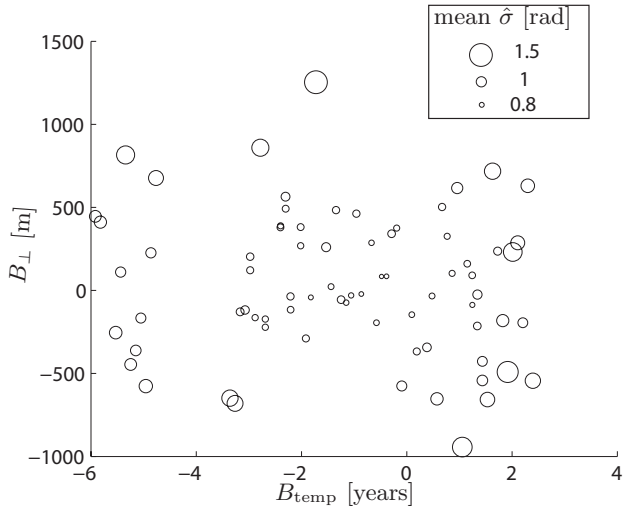

Fig. 4.6. Mean value of the estimated standard deviation for the arcs used in the initial network ($\hat{\sigma}$) plotted versus $B_\perp$ and B_{temp}. The size of the circle depends on the standard deviation.

Comparison with previous methods using statistical tests

We start by unwrapping the first order network and we keep track of the number of accepted arc for each method. We then unwrap the second order network by connecting the remaining PS to the first order network at three different locations.

The number of first order network arcs that survive the test is different for each unwrapping method. Therefore, in order to have a fair comparison we unwrap the second order network using the same first order network for all methods. Table 4.3 summarizes the results of the statistical tests obtained for each unwrapping method. The number of accepted arcs shows that our approach performed the best for both, first and second order networks. The number of accepted arcs with our algorithm is 5442 compared with 4141 obtained with the bootstrap estimator and 3660 with the ensemble coherence maximization.

Comparison with previous methods using estimated rates

We also compare visually the deformation rates estimated with our method for phase unwrapping with the values obtained using the bootstrap estimator and ensemble coherence maximization methods. The model also included height (h) and master contribution (c), but they are not discussed here. We employ the same initial search space for all cases. The initial search space for the velocities was restricted to the interval from -17.5 mm/yr to $+17.5$ mm/yr. The results of the rates from all three methods are displayed in fig. 4.8. From a visual inspection of fig. 4.8, we see that the image with the least spatial noise corresponds to our new method, shown in fig. 4.8A.

The estimates of the bootstrap estimator and ensemble coherence maximization method are plotted against the results obtained by our new approach in fig. 4.7B and C, respectively. After integrating the solutions with respect to a common reference PS, velocity values can be outside the initial search space. If the estimates given by each method were the same the values would lie on a diagonal line with slope one.

Table 4.3. Number of first order network arcs and PS accepted after tests for the proposed method (Bayes), bootstrap estimator (Boot.) and coherence maximization (Period.). The observations were also weighed with the inverse of the variance, estimated by our method (weight=$1/\hat{\sigma}_k^2$) and employing the VCE method of Kampes (2006), (weight=1/VCE). For the coherence maximization method, we did not weigh the observations.

	Bayes weight=$1/\hat{\sigma}_k^2$	Bayes weight=1/VCE	Boot. weight=1/VCE	Period. No weight
Accepted 1st order arcs (Total 2051)	1909	1896	1876	1849
Accepted PS (Total 28704)	5442	5383	4141	3660

Most of the values form a line in figs. 4.7B and C, but some do not. Hence, different solutions were found by our method and the other two. The major differences are grouped in three parts of the plot. They correspond to the three modes of deformation velocities, also visible in the histogram in fig. 4.7A. This shows the influence of $\hat{\wp}(X)$ in the estimation process.

The introduction of $\hat{\wp}(X)$ in the process can affect the estimations in two ways. First, if the PS in question contains significant signal despite the noise, $\hat{\wp}(X)$ will help to find the right solution by avoiding other maxima of $\wp(\phi|h)$, see eq. (4.18). An example of this case is shown in fig. 4.5, as discussed in section 4.2.3. Second, if the PS is completely noisy the $\wp(\phi|h)$ plays almost no role in the estimations, because it is expected to be uniform. Then, the solution is given by the maximum of $\hat{\wp}(X)$. Although it is very likely than the PS in question behaves as its nearby PS, the application of eq. (4.18) with $\hat{\wp}(X)$ carries the risk of assigning an estimate to the noisy PS that is mostly based on the surroundings. In any case, these pixels can be then detected based on spatially consistency tests or estimated noise.

We examined the probability $\wp(\phi|h)$ for some of the PS that had large differences between the estimation obtained by our new approach and the other two methods. We found in all cases that, before including $\hat{\wp}(X)$, there were local maxima near the final solution that was obtained by our method, similar to the situation shown in fig. 4.5. Therefore, we conclude that the differences between the methods here examined are due to the first reason—$\hat{\wp}(X)$ avoids wrong maxima—also proved with the simulations of section 4.2.3.

4.2.5 Summary of the validation and tests

We test the methods of variance estimation and phase unwrapping using simulated and real data. The results show a considerable improvement in the number of correctly unwrapped pixels in the case of synthetic data. With real data, the results are compared with those obtained by two other approaches. Our method shows a significant increase in the number of accepted arcs and PS after statistical tests, with at least 1200 more accepted PS than with the other two methods. From the results obtained from both, simulated and real data, we conclude that the phase variance of PS and the pdf of their model coefficients can be determined spatially, and phase unwrapping can benefit from the two.

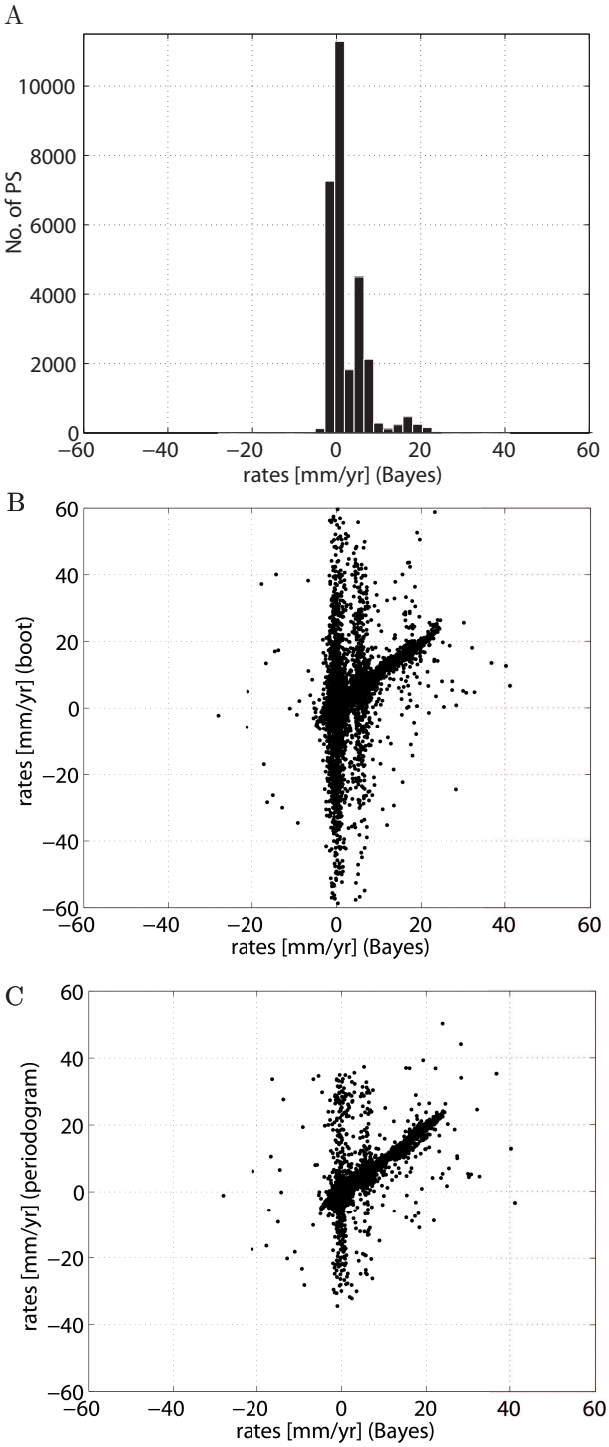

Fig. 4.7. (A) Histogram of the deformation rates estimated using the method here proposed (bayes). (B) Rates estimated by bootstrap estimator (boot) versus our method (bayes). (C) Rates estimated by ensemble coherence maximization (periodogram) versus our method (bayes).

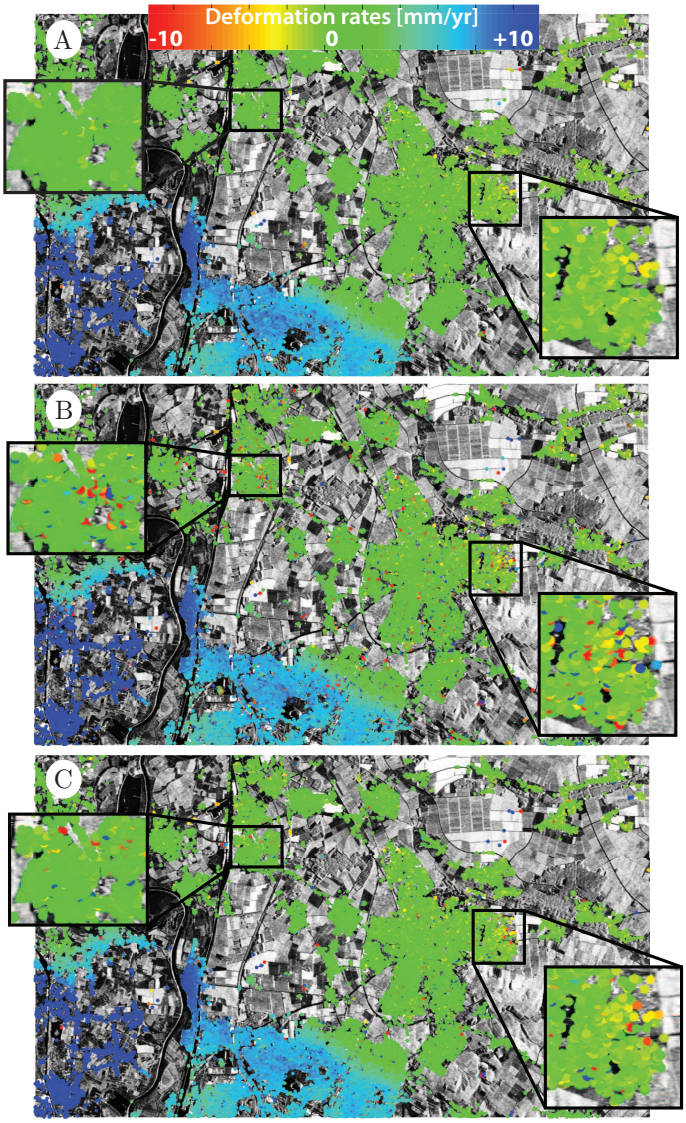

Fig. 4.8. Surface deformation rates estimated with: The method here proposed (A), bootstrap estimator (B) and ensemble coherence maximization (C). Black boxes show zooms of some of the areas where the differences between the methods are the greatest, after visual inspection.

Despite the advantages, our method has some limitations. Since it performs spatial estimations, the approach requires sufficient data density. We also observed that the computational cost of our method was about three to four times higher than the other techniques here considered. This additional cost is caused by the extra spatial operations, which are not performed by the other methods.

4.3 Improvements specific to the reference technique, DePSI

In this section we optimize the work flow of DePSI with the goal of improving the estimation of the spatially correlated noise and to increase the number of PS that are reliably unwrapped.
The main difference between the algorithm flow that we propose and DePSI's (compare fig. 4.9 with fig. 3.6) is the introduction of a second order network with PS that are consistently unwrapped, i.e. their unwrapped solutions survive statistical tests.

The joint first and second order networks being denser than the first order network alone, should improve both the estimation of spatially correlated noise, e.g. atmospheric phase screen, and the final densification that is performed with the remaining PS.

4.3.1 Estimation of spatially correlated noise: the second order network

We use the term spatially correlated noise to refer to a signal that is not correlated in time but is correlated in space. This noise is mainly caused by inaccurate orbits, atmosphere, and processing errors.

At large scales, in the order to tens of km, the spatially correlated noise is produced by inaccurate orbits, ionospheric fluctuations and atmospheric variations due to pressure differences (hydrostatic delay) (Hanssen, 2001). At scales in the order of few km, atmospheric variations caused by differences in the water vapor content are the main source of the spatially correlated noise. At small scales, less than 1 km, the spatially correlated noise is unlikely to have an atmospheric origin (Hanssen, 2001). Instead, it is likely to be caused due to errors during interferometric processing such as the subtraction of the reference DEM or resampling.

Subtracting spatially correlated noise helps phase unwrapping because it reduces phase variability. The reference technique, DePSI, estimates atmospheric variations and orbital errors (phase ramps) using the first order network. This network contains the most reliable PS, but it is sparse due to computer constrains.

Effectively, the adjustment procedure of the first order network requires the inversion of large matrices. Its density when large areas (e.g. 30×30 km^2 and larger) are processed is on average $\sim$4 PS per km^2, with a usual separation between PS in the order of 500 m, although these values are case dependent.

A low density network means that the spatially correlated noise may not be precisely estimated at small scales. Therefore, we optimize the current algorithm to remove also small scale noise by employing a denser network of reliable PS. The densification is performed as suggested in the original technique, see section 3.4.7, with the difference that we aim specifically at forming a second order network of PS that are reliably unwrapped.

We densify the first order network by adding PS that are not selected for the first order network but survive statistical tests for phase unwrapping. Each PS is connected to the first order network at the three nearest locations, see fig. 4.10A. These three arcs are then unwrapped in time. The redundancy of the connections is used to detect inconsistent PS,

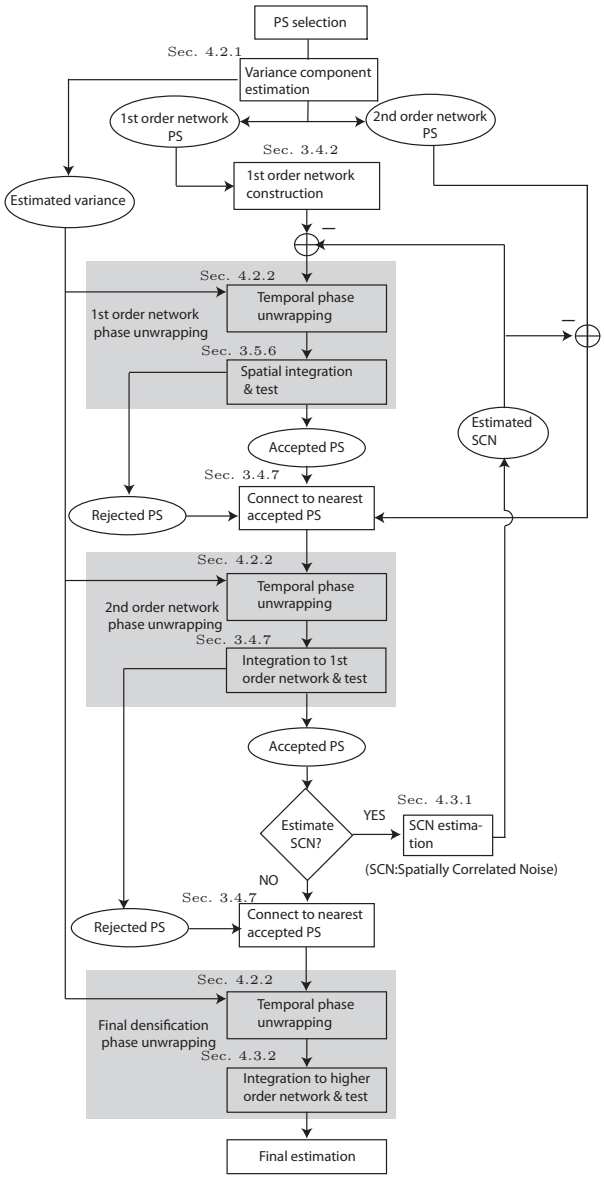

Fig. 4.9. DePSI processing flow optimized for the estimation of spatially correlated noise and the final densification step. The original flow chart is shown in fig 3.6. Rectangles represent processes and ovals represent data. Complex processes are displayed in gray. Rectangles with a dashed frame represent where the reference algorithm has been modified. The corresponding sections are also indicated.

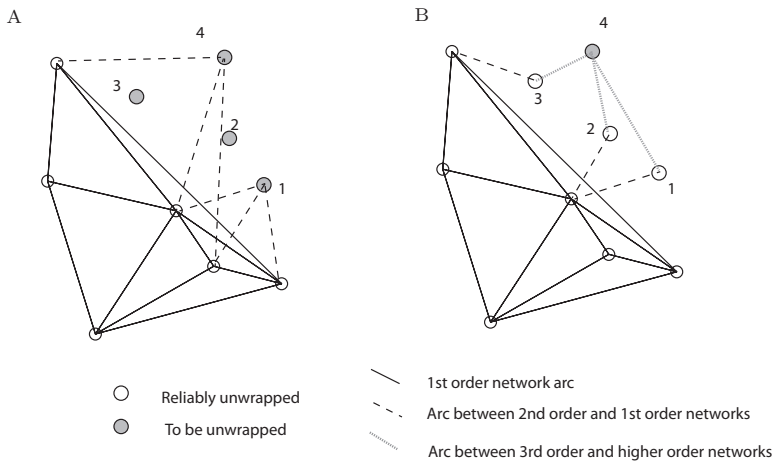

Fig. 4.10. (A) First densification: PS belonging to the second order network (shown in gray) are unwrapped by connecting them to the first order network at three different locations. The figure shows how PS 1 and 4 are connected, the same happens for PS 2 and 3. (B) Final densification: PS 1, 2 and 3 passed the consistency tests they are assumed to be reliable unwrapped. PS 4, which was initially rejected from the second order is unwrapped once again by connecting it to the newly-created dense network of reliably unwrapped PS, i.e., the joint first and second order networks.

which are removed from the second order network. In the example of fig. 4.10, PS 4 does not survive the tests.

Additionally, PS with low ensemble coherence, i.e. high noise, are also rejected. The adjustment and test of the second order network does not increase computer load, because these arcs are treated individually.

Finally, the joint first and second order networks provide a density of observations that can reach 100 of PS per km^2, which therefore improves the spatial estimation of noise.

After the construction of the first and second order networks, the spatially correlated noise is estimated applying the same principles as in the original technique. First and second order networks are unwrapped and adjusted relative to a common reference PS. Their unwrapped phases are then high pass filtered in time to obtain the signal that is not correlated in time. The resulting values are used to estimate the spatially correlated noise per interferogram. Long wavelength signals, e.g., orbit errors, are estimated by fitting a plane to the high-pass filtered phase. The remaining spatially correlated noise is obtained by smooth-interpolated in space.

We then subtract the estimated spatially correlated noise from the original wrapped phases of all detected PS. Since phase variability is reduced, unwrapping errors are expected to decrease. The whole process is repeated from the beginning, i.e. the first and second order networks are re-built, and the phase differences of each arc (without spatially correlated noise) are unwrapped and integrated to a common reference.

Table 4.4. Number of accepted first order network arcs and PS when the spatially correlated noise (SCN) was estimated with a sparse network (second column) and with dense network (third column) for two different test areas.

	SCN from sparse network	SCN from dense network
Area 1		
Accepted 1st order arcs (Total 2051)	1909	1930
Accepted PS (Total 28704)	5442	6001
Area 2		
Accepted 1st order arcs (Total 24602)	22831	23369
Accepted PS (Total 87806)	28026	32440

Tests results

We check the proposed optimization for DePSI on the basis of the number of PS that survived statistical tests after removing the spatially correlated noise. The number of PS that survive the tests is calculated for both cases, DePSI (sparse network for SCN estimation) and the optimized DePSI (dense network for SCN estimation).

Table 4.4 contains the results of this comparison. With the dense network approach, the number of accepted arcs and PS is higher, suggesting that there exist spatially correlated noise at small scales and that it cannot be removed using only the sparse network.

4.3.2 Final densification

To increase the density of reliably unwrapped PS, we add one more iteration to the densification step to the original DePSI workflow, (referred to as final densification–phase unwrapping in fig 4.9).

This step aims at recovering PS that still have relevant information but are rejected during inconsistency checks, probably due to the fact that they are connected to the reference network through long arcs. It is worth recalling that rejection from these networks occurs because there exist inconsistencies in the estimated ambiguity cycles or high differences between modeled and measured phases. Rejection from first and second order networks is likely to be caused by noise or an oversimplified model. A way of reducing these error sources is to decrease the distance between PS, because the variability of any spatially correlated signal will also reduce. For example, deformation of a short arc can be approximated with a linear temporal model, while for long arcs with linear temporal behavior are less likely. Failure can also be caused by unmodeled atmosphere and orbits errors.

The process of recovering initially rejected PS is represented in fig. 4.10. Figure 4.10A shows several PS (1–4) that belong to the second order network and need to be unwrapped. PS numbered from 1 to 3 survive the tests; thus, they belong now to the reliable second order

Table 4.5. Number of PS that are accepted after consistency checks for two different areas. The first column contains the names of these areas (coal field of South Limburg and the Roer Valley Rift System (RVRS), see chapter 2). The second column shows the number of PS that are accepted using the in the densification only the first order network. The third column displays the number of PS that are accepted during the final densification using the dense network approach.

Area	sparse network	dense network
Coal field	32440	55166
RVRS	81435	122740

network. However, PS 4 is rejected from the second order network. We connect PS 4 again to the new and dense reliable network, which also includes PS 1–3. We expect unwrapping errors to be reduced by decreasing the distance between PS (the arcs of PS 4 are shorter in fig. 4.10B than in fig. 4.10A). The processes of unwrapping and testing during the final densification step are the same as for the second order network. We connect the remaining PS to the joint first and second order networks at three nearest locations because this helps to detect inconsistent solutions, see fig. 4.10B.

All three arcs are unwrapped individually. Then they are integrated to a common reference PS assuming that the solutions of the first and second order PS are deterministic. The spatial integration of the estimated ambiguity cycles is thus performed by addition. Since we connect the PS at three locations of the reference network we can use this redundant information (i.e. three solutions) to detect incoherent PS. In fact, the integration of the estimated ambiguity cycles should be path-independent. If the three solutions (integrated ambiguity cycles) are the same we can say that the PS has been consistently unwrapped.

Tests results

To test the proposed dense-network approach, we calculate the number of PS that are consistently unwrapped in the final densification. We compare this value with the number of PS that survive the test when unwrapping is carried out by connecting the PS to the (sparse) first order network.

These tests are performed for two areas, the Roer Valley Rift System and the coal field of southern Netherlands, which are the areas of interest of this dissertation, see chapter 2.

The results of the test are summarized in tab. 4.5. For both areas, the number of PS that survive the tests increases when using the denser network approach that we propose.

The results show an improvement of almost 40% in the number of PS that are consistently unwrapped. As discussed above, the results suggests that reducing the arc length decrease the variability of spatially correlated signal which seems to improve phase unwrapping.

4.4 Long term processes monitoring with PSI

In previous sections, we investigated how the estimation process can be improved for temporal PSI methods by taking advantage of spatially correlated information. This section tackles a different problem: the long term monitoring of deformation signals using PSI.

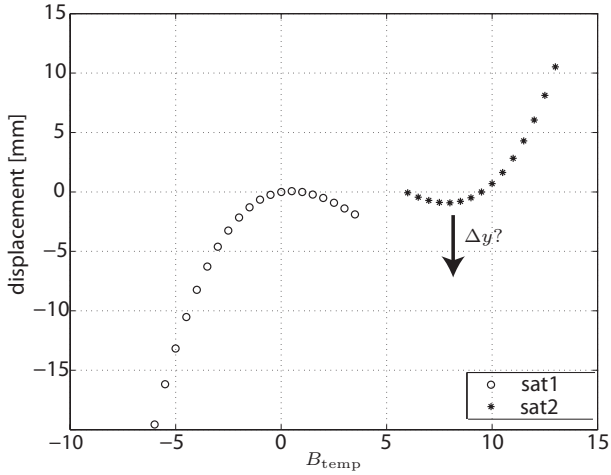

Fig. 4.11. An example of a expected situation when the time series have different time reference (master image). The value Δy needs to be estimated to be able to join the time series.

With PSI techniques, the time span that surface deformation processes are observed is limited by the satellite lifetime, which is usually less than 10 years. However most of deformation phenomena last longer. In order to fully monitor and comprehend the observed signal, acquisitions from different sensors can be merged. This is a complex task for one main reason. PSI methods provide with estimations that are relative in time to one of the acquisitions, i.e. the master or reference image. Therefore, time series acquired by different sensors have different reference images and cannot be directly compared or joint unless they have the same time reference system. In global terms, the operation of translating from one to another reference systems consist of estimating a vertical offset, which is the total deformation that occurs between the two master times. This is depicted in fig. 4.11, where the vertical offset is represented with Δy. We therefore assume that we use the same spatial reference.

To estimate the vertical offset Δy, different strategies can be applied, for example, using additional data such as leveling or GPS measurements. Here, we propose to use least squares to merge PSI time series without any ancillary information. This method treats the time series individually, i.e., per PS, and requires some knowledge of the deformation signal, such as the model that is expected to describe its temporal behavior.

To test the proposed approach, we apply it to the coal mines of southern Netherlands which is one of the areas of interest of this thesis see description in section 2.3. We join PSI time series that are obtained from images provided by ERS1/2 and Envisat to overcome the data in gap spanning from 2001 until the end of 2003. ERS1/2 stopped working nominally in 2001 after the break down of the gyroscopes controlling the satellite attitude. On the other hand, Envisat started nominal acquisitions at the end of 2003. The results are finally compared with in-situ groundwater levels, which are, in principle, the main cause of deformation.

4.4.1 Method for vertical offset estimation

Let us assume that we aim at merging two PSI time series acquired by two different satellites that are indicated with the subscript $\{.\}_{\text{sat1}}$ and $\{.\}_{\text{sat2}}$ where the acquisition time spans do not overlap, similarly as indicated in fig. 4.11. The set of PS that are detected at each satellite periods are denoted to as PS_{sat1} and PS_{sat2}, respectively.

In our method, we first coregister the master images of each stack to improve the relative location of PS detected at different periods. It can happen that PS detected during one of the time periods may not be found in the other period. For that reason, we interpolate spatially the estimated deformation using ordinary kriging. We opt for this method, because it uses the covariance of the deformation and estimates how it changes with distance, (Wackernagel, 1995). Nevertheless, to reduce interpolation error, our method interpolates the estimated deformation for PS_{sat2} at the location of PS_{sat1}.

After interpolation, for any generic location, we obtain two deformation time series for the time spans t_{sat1} and t_{sat2}, which are denoted with the vectors as y_{sat1} and y_{sat2}, respectively.

The vector lengths are given by the number of interferograms created with respect to the master image of each data set, denoted with N_{sat1} and N_{sat2}, respectively.

To join the time series, the deformation is modeled as a function of time, $f(t)$. The same function is used for both time series. However, the second time series include an extra offset because the interferograms are with respect to different master images. The relation between the observations, (deformation time series) and the unknown parameters (coefficients of $f(t)$) are formulated using a Gauss-Markov model:

$$E\{\begin{bmatrix} y_{\text{sat1}} \\ y_{\text{sat2}} \end{bmatrix}\} = \begin{bmatrix} f(t_{\text{sat1}}) & 0 \\ f(t_{\text{sat2}}) & 1 \end{bmatrix} \begin{bmatrix} d \\ \Delta y \end{bmatrix}, \tag{4.26}$$

where t_{sat1} and t_{sat2} are the acquisition times of satellites sat1 and sat2 respectively. The unknowns parameters defining $f(t)$ are included in the vector d. The term Δy is the desired offset, see example in fig. 4.11.

In addition to that, the stochastic model is given by,

$$D\{\begin{bmatrix} y_{\text{sat1}} \\ y_{\text{sat2}} \end{bmatrix}\} = \begin{bmatrix} Q_{y_{\text{sat1}}} & 0 \\ 0 & Q_{y_{\text{sat2}}} \end{bmatrix}, \tag{4.27}$$

The vc-matrices, $Q_{y_{\text{sat1}}}$ and $Q_{y_{\text{sat1}}}$, are obtained from the data. For each satellite period, we estimate a covariance model that describes the average stochastic behavior in time of all detected PS.

The functional model can also be written in a simplified formed:

$$E\{y\} = Ax, \tag{4.28}$$

where y represents the observations, A represents the design matrix and x is the vector of unknowns.

The same can be applied to the stochastic model:

$$D\{y\} = Q_y, \tag{4.29}$$

The matrix Q_y is the vc matrix of the observations, which can be decomposed as

$$Q_y = \sigma^2 R_y, \tag{4.30}$$

where R_y is the cofactor matrix obtained from the covariance model.

The estimated unknowns $\hat{x}$ are obtained with BLUE by:

$$\hat{x} = \left(A^T Q_y^{-1} A\right)^{-1} A^T Q_y^{-1} y, \tag{4.31}$$

and the modeled observations $\hat{y}$ with

$$\hat{y} = A\hat{x}. \tag{4.32}$$

Furthermore, BLUE provides with the variance of the estimates, $Q_{\hat{x}}$ and means of testing the strength of the model through the Overall Model Test (OMT) (Teunissen, 2000b):

$$\text{OMT} = \frac{\hat{e}^T R_y^{-1} \hat{e}}{\sigma^2 (N-u)}, \tag{4.33}$$

where $\hat{e}$ represents the residuals, $\hat{e} = y - \hat{y}$, N the number of observations (interferograms) and u the number of unknowns. Note that for visualization, we have normalized value of OMT by $N - u$, being originally defined as $OMT = \hat{e}^T Q_y^{-1} \hat{e}$ (Teunissen, 2000b).
With the expression given in eq. (4.33), we compare the empirical variance, which is estimated from the residual values, with the variance assigned *a-priori* to the observations σ^2. An OMT value of 2 therefore means that the empirical variance doubles the *a-priori* variance. High values of OMT (e.g. higher than 2) suggest errors in the observed data or that the models (either stochastic or functional) fail to represent the measurements.

4.4.2 Results

We apply this method to the southern Netherlands where the land is deforming due to the effect of water rebound in abandoned coal mines. Chapter 6 analyzes this phenomenon in depth. The time series that we wish to join are obtained by ERS1/2 from April 1992 to December of 2000 and by Envisat from December 2003 to October 2009.

After coregistering the corresponding master images, we interpolate the deformation estimated with Envisat to the locations of the PS detected by ERS1/2. In order to have similar noise levels, the deformation obtained by ERS1/2 is filtered spatially, also using ordinary kriging.

The time series are joined by checking alternatively two different models and selecting the one that fits better the observations. The first model is a third degree polynomial. The second model, in addition to the third order polynomial, includes a breakpoint in 1994, because we expect, for some areas, an acceleration of the motion in this year due to the cease of water pumping, see chapter 6.

The temporal variance function is estimated empirically fitting a Gaussian function to the data that reflect the mean stochastic behavior of about 300 PS located in non-deforming area.

Figure 4.12 displays the OMT obtained for each PS. The eastern side of the processed area show high values for the OMT. As we will see in chapter 6, this area is subject to a strong subsidence during the initial ERS1/2 period which change during the data gap of 2001-2004. Therefore, it is very probable that the functional model, i.e. third degree polynomial and break point, fails to describe the deformation behavior.

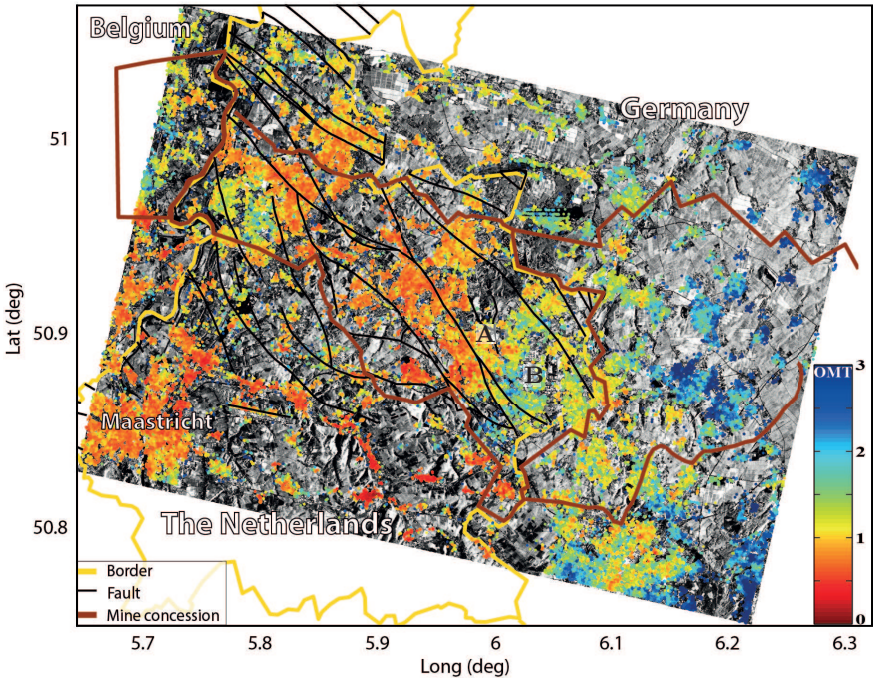

Fig. 4.12. Overall model test, OMT obtained from eq. (4.33). High OMT suggest errors in the observations, or the models, functional or stochastic, fail to represent the data. The letters A and B indicate the location of the time series shown in fig. 4.13.

4.4.3 Time series

Two examples of time series that are connected using our method are shown in fig. 4.13. The master of ERS1/2 stack was acquired in August 1998 and the one of the Envisat stack in February 2007. The time series are displayed along with mine water levels, which are the main cause of deformation in this area, see chapter 6. The estimated offset obtained from the functional model match the behavior expected from the water levels. Furthermore, the low values of the OMT gives us confidence on the results. The estimated error is also indicated in the figure as a gray area. For both cases the estimated offset error is around 4 mm. This value describes the precision of the joined time series, of course, assuming that both models, functional and stochastic, are correct.

4.5 Summary and conclusions

In this chapter, we provided with a method of spatial determination of the noise variance of PS and the pdf of the parameters describing their temporal behavior. Using these two sets of information, we developed a new method for phase unwrapping through Bayesian inference. Our Bayesian approach for phase unwrapping was tested using real and simulated data. In particular, we showed through simulations that the new phase unwrapping method was able to correct time series that were in first instance wrongly unwrapped. The tests also showed improved results when compared with other algorithms. Our method

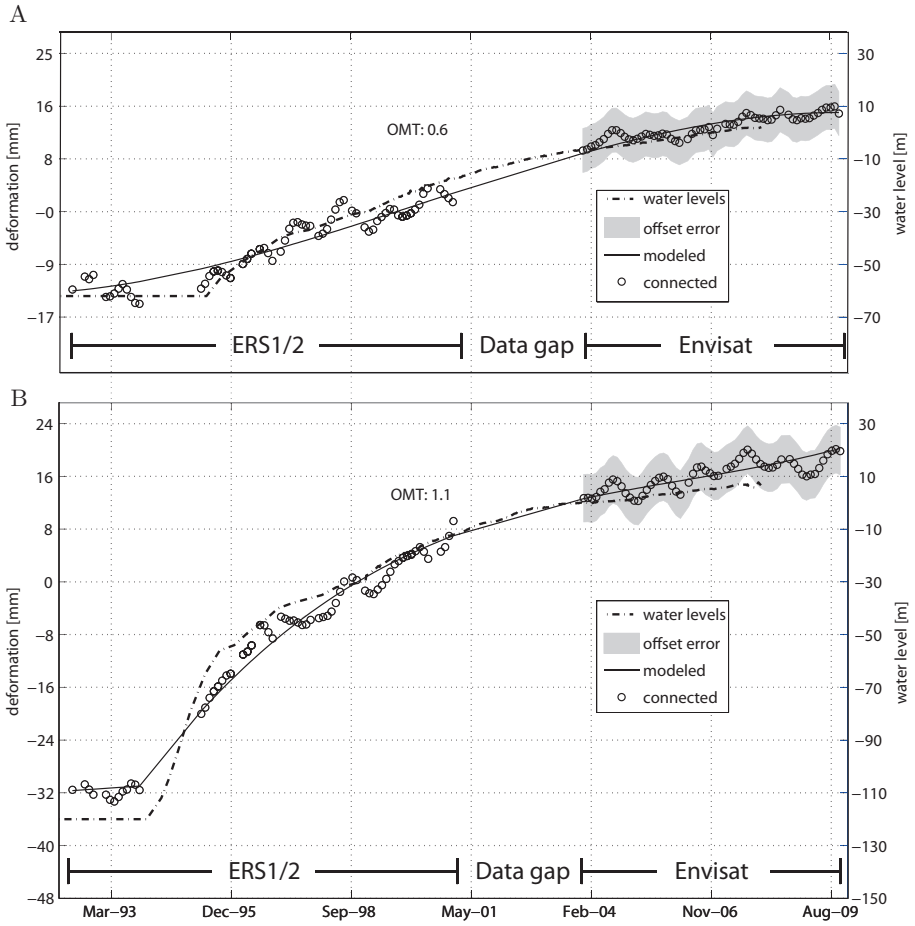

Fig. 4.13. Two examples of joined time series. The results are compared with water levels, because this is the main source of surface displacements in the study area. The location of A and B is indicated in fig. 4.12. The scales of water time series are stretched using the linear relationship we found between the water levels and surface deformation.

increased in the number of PS that survived statistical test performed on the unwrapped solutions.

We also investigated how to optimize the algorithm flow of DePSI, the technique used as reference in this dissertation. The most important variation that we proposed consisted in creating a dense network of reliable PS. This network was used in the estimation of spatially correlated noise and as reference network for the final densification. In both cases, the dense network approach showed an increase on the number of PS that survived statistical tests when compared with the original algorithm.
Finally, we provided a method to join time series obtained by different satellites with the goal of monitoring long term processes. The method was tested and showed good agreement

with in-situ measurements.

In the next chapters, these improvements are applied to study ground displacements associated to geological faults. Chapter 5 is dedicated to study surface deformation in the Roer Valley Rift System area and chapter 6 applies the improved PSI algorithm to the abandoned coal fields of the southern Netherlands.

Chapter 5

Surface Deformation in the Roer Valley Rift System Observed by PSI

5.1 Introduction

Chapter 2 discussed the discrepancies that were found in Neotectonic tectonic rates of the Roer Valley Rift System when they were estimated at short (10-100 yr) and geological (10^5-10^6 yr) time scales. Techniques covering short time scales, such as leveling, measured a subsidence of the Roer Valley Graben with respect to the adjacent blocks in the order of 1 mm/yr, (see, e.g., Groenewoud et al. (1991); Demoulin (2006)). Meanwhile, methods that measured at geological time scales, such as trenching, estimated slip rates one or two orders of magnitude lower (see, e.g., Vanneste et al. (2001); Houtgast and van Balen (2000)).

We can explain the differences between short-time and geological estimates based on three causes. First, geological estimates are erroneous or misinterpreted. Second, short time scales estimates are erroneous or misinterpreted. Third, the tectonic signal changes with time and the rates estimated at geological time scales are the average of the deformation that happens over millions of years.

Studying the error sources of geological estimates is beyond the scope of this dissertation. In any case, based on the reasonable agreement found between different geological time estimates, we focus on analyzing the other two explanations: Errors (or misinterpretation) in short time scale estimates versus a variable tectonic motion.

To investigate this question and to learn more about the Roer Valley Rift System, we apply Persistent Scatterer Interferometry (PSI) to a time series of radar images covering this area. In particular, we use the PSI algorithm developed in this research, which is an optimized version of Delft implementation of PSI, DePSI. Both, the reference algorithm and its optimized version were described in chapters 3 and 4, respectively.

The full set of radar images spans about 18 years, from April 1992 to November 2009, with data gaps in 1994 due to ERS1/2 mission requirements and from January 2001 to December 2003 that was the time interval between a malfunctioning of ERS1/2 gyroscopes and the start of systematic data acquisition by Envisat. We employ 135 focused radar images (also referred to as SLC) in descending mode, 75 were acquired by ERS1/2 and 60 by Envisat. We use the total nominal footprint of these satellites covering an area of around 100×100 km^2 and center in the Roer Valley Rift System, see location in the inset

plot of fig. 5.1.

5.2 Rates in the Roer Valley Rift System area estimated with PSI

This section analyzes linear displacement rates in the Roer Valley Rift System determined from the displacement time series estimated with PSI. For a precise analysis, we need to divide the full data set in three time periods: April 1992 to October 1997, October 1997 to January 2001 and from December 2003 to November 2009. These three time spans are selected for the following reasons. The first period covers from April 1992 (first acquisition) to October 1997, that is the date of closure of coal district of Erkelenz, see location in fig. 5.2. We expect the abandonment of this mine to have an effect on surface displacements; this is a signal that can be confused or mixed with a probable Neotectonic motion. The second studied period starts in October 1997 and ends in January 2001 due to the malfunctioning of ERS1/2 in 2001. Systematic acquisitions of the satellite Envisat did not start until December 2003. We decide not to join ERS1/2 with Envisat time series for rate estimation, because the joining process introduces an error of about 5 mm, see section 4.4, and final estimates would not be accurate enough to study 1 mm/yr signals, as it is expected for the tectonic motion. The last of the studied period therefore spans from December 2003 to November 2009, the date of the last available acquisition at the moment of this research. For the sake of simplification, we round these dates to the closest significant year; thus we denote these three periods as 1992-1997, 1997-2001, and 2004-2010, respectively.

From PSI time series, we produce three velocity maps, one per period. Linear displacement rates and corresponding variances are estimated applying BLUE (Best Linear Unbiased Estimator) (Teunissen, 2000a) to the time series. The residual topography and spatially correlated noise have already been estimated and removed at this stage, see section 3.4.8. In particular, the spatially correlated noise was determined by high pass filtering the unwrapped time series with window of six months, see section 4.3.1.

Linear displacement rates are estimated with a functional model that includes both linear displacements and 1-year periodical signal to take into account a possible seasonal signal. For a given PS, the system of equations to be solved is given by (Kampes, 2006):

$$E\{y\} = \underbrace{\begin{bmatrix} B^1_{\text{temp}} & \sin(2\pi B^1_{\text{temp}}/\tau) & (\cos(2\pi B^1_{\text{temp}}/\tau)-1) & 1 \\ B^2_{\text{temp}} & \sin(2\pi B^2_{\text{temp}}/\tau) & (\cos(2\pi B^2_{\text{temp}}/\tau)-1) & 1 \\ \vdots & & & \\ B^N_{\text{temp}} & \sin(2\pi B^N_{\text{temp}}/\tau) & (\cos(2\pi B^N_{\text{temp}}/\tau)-1) & 1 \end{bmatrix}}_{A} \underbrace{\begin{bmatrix} v \\ D_1 \\ D_2 \\ c \end{bmatrix}}_{x}, \tag{5.1}$$

where y is the vector of displacements in the line-of-sight (LOS) of a PS, B^i_{temp} (with $i = 1, .., N$) is the temporal baseline of interferogram i and N the number of (single master) interferograms of a given period and τ is the period of the signal assumed to be equal to 1 yr. The unknowns are the displacement rate v, the coefficients D_1 and D_2, which relate to the amplitude (D_{season}) of the seasonal signal :

$$D_{\text{season}} = \sqrt{D_1^2 + D_2^2}, \tag{5.2}$$

and to the temporal offset t_0:

$$t_0 = -\text{sign}(D_2)\frac{1}{2\pi}\arccos(\frac{D_1}{D_{\text{season}}}), \tag{5.3}$$

and a constant value c to take into account a vertical offset of the displacement due to the noise of the radar image used as reference.

To determine the precision of the estimated parameters, we first estimate the standard deviation of the displacements from residual values (observed minus modeled displacement):

$$\hat{\sigma}^2 = \frac{\hat{e}^T\hat{e}}{N-u}, \tag{5.4}$$

where $\hat{\sigma}$ is the estimated standard deviation of the displacements of a PS, $\hat{e}$ represents the residuals, $\hat{e} = y - \hat{y}$, N the number of observations (interferograms) and u the number of unknowns, which is equal to four in our case.

The vc-matrix of the observations, Q_y , is assumed to be uncorrelated with diagonal elements equal to $\hat{\sigma}^2$. With Q_y, we estimate the precision of the unknowns:

$$Q_{\hat{x}} = (A^T Q_y^{-1} A)^{-1}, \tag{5.5}$$

where $Q_{\hat{x}}$ is the vc-matrix of the estimated parameters and A is the design matrix defined in the functional model of eq. (5.1). The values of the precision determined as explain above may be underestimated for the locations where the assumed functional model oversimplifies the actual temporal behaviour of the deformation signal.

The estimated linear displacement rates are displayed in figs. 5.1A, B and C for 1992-1997, 1997-2001 and 2004-2010, respectively. The rates are calculated relative to 1 km radius area whose center is marked with a red circle in the figures (located in the center north of the graben). Due to the low displacement rates found in the Roer Valley Graben, the color scale is saturated to increase the contrast between different deforming areas. The same color scale is used to display both line-of-sight (LOS) and vertical rates. The vertical component is determined assuming the observed displacement is only a vertical. Transformation from LOS to vertical is performed by dividing LOS rates by $\cos(\theta)$, being θ the satellite looking angle $\sim 23^o$ for ERS1/2 and Envisat, see section 3.2.1.

For the relatively small rates that we find in the graben area, the transformation from LOS displacements to vertical is almost insignificant. Maximum values of 2 mm/yr in LOS becomes 2.2 as vertical, see fig. 5.1. The standard deviations estimated for these rates are displayed in fig. 5.3.

Period 1992-1997

The rates estimated for this period are displayed in fig. 5.1A. In the Roer Valley Graben area, we detect a deformation signal associated with geological faults. However, this signal cannot be attributed to a tectonic motion, because the results reveal the graben to behave opposite to what is predicted by tectonics. Effectively, most of the Roer Valley Graben uplifts with respect to adjacent horsts. This is particularly visible comparing areas 1 and 2. The differences between the graben and the horst will become more apparent in the study cross sections and time series in sections 5.2.1 and 5.2.2, respectively.
Although most of the graben uplifts, the whole structure does not behave the same. An area in the north-west of the graben, near the zone marked with an A in fig. 5.1A subsides with respect to the Campine Block. However, this subsidence signal seems unlikely to be

produced by a slip in the Feldbiss Fault Zone, because it appears to travers the fault.
The precision estimated for the rates is shown in fig. 5.3A. Although the signal in the graben and the Peel Block is small (with average values that range from +0.5 to +1 mm/yr for the graben and from -0.5 to 0 mm/yr for the horst), the estimated precision is in the order of 0.2 mm/yr, giving us confidence in our results.

Interesting enough, the uplift motion of the graben appears to be bounded by faults. This is observed in the center and south side of the Peel Boundary Fault Zone (areas 1-2 and 3-4). This situation suggests that the signal is related to underground water flow. Different studies (see e.g., Hoffmann (2003); Bell et al. (2008)) have shown how aquifer recharge, which can be a consequence of seasonal rain variations, can produce uplift due to pore pressure increase in aquifers. The geology and therefore aquifer zones of the graben are different to these of the Peel and Campine blocks due to long term tectonic deformation and erosion (Bense, 2004). Furthermore, water flow are strongly influenced by tectonic faults in this area, because they can act as hydrological barrier due to their low permeability (Bense et al., 2003). Therefore, pore pressure differences can be expected between aquifers in both side of the faults, because they are not in hydrologic connection. Pore pressure differences can translate as different deformation rates for horsts and grabens.

Signals that also seem related to water flow appear in other areas near the Roer Valley Graben. The subsidence of the Erkelenz coal district (ECD in fig. 5.1), which is still active in this period is partly caused by groundwater pumping. More specifically, the displacement is the consequence of two processes: underground mining and groundwater pumping that is required to keep a dry working environment (Heitfeld et al., 2002). Water extraction decrease the pore pressure making the surface to subside (Pöttgens, 1985).

Water extraction in German lignite mines, which are located further to the southeast of the graben, see fig. 5.2, has a very strong influence on the displacement field. The mine closest to the graben is the Garzweiler lignite mine (GLM in fig. 5.1), where large amounts of water are pumped out for the mineral extraction (see, e.g., Bense et al. (2003)). Also for this area, displacements are bounded by faults, for the reasons explained above.

To the northeast of the Venlo Block, in the Walsum coal district, we can distinguish the effect of coal production on surface displacements, see area WCD fig. 5.1. As in Erkelenz, the displacement is caused by underground mining and water pumping. However, the large extent of the subsidence area ($\sim$15$\times$15 km^2) suggests that an important part of the detected signal is caused by water pumping. Deformation caused by underground mining is localized straight above the excavated ground with a spatial extension whose radius is about the same that the depth of the mining (Kratzsch, 1983), which in this case, is much less that 7.5 km.
Therefore, the detected signal suggests that large amounts of water are extracted in Walsum, which seems in agreement with Bayera et al. (2009). Once again, this signal appears to be bounded by a fault, in this case, by the Viersen Fault Zone (VFZ in fig. 5.1).

In summary, we detect for this period several areas where water pumping seems to result in surface deformation. Furthermore, these signals correlate with fault location and can be observed at large distances from a probable pump location. As we will see in the next section, the opposite situation, cease of pumping, can result to uplift due to the consequent pore pressure increase. In the same line of though, we explain the uplift signal that we observe in the central and southern part of Roer Valley Graben (areas 1-2 and 3-4) as being produced by pore pressure increase. A possible source of these pore pressure changes is discussed in section 5.3.

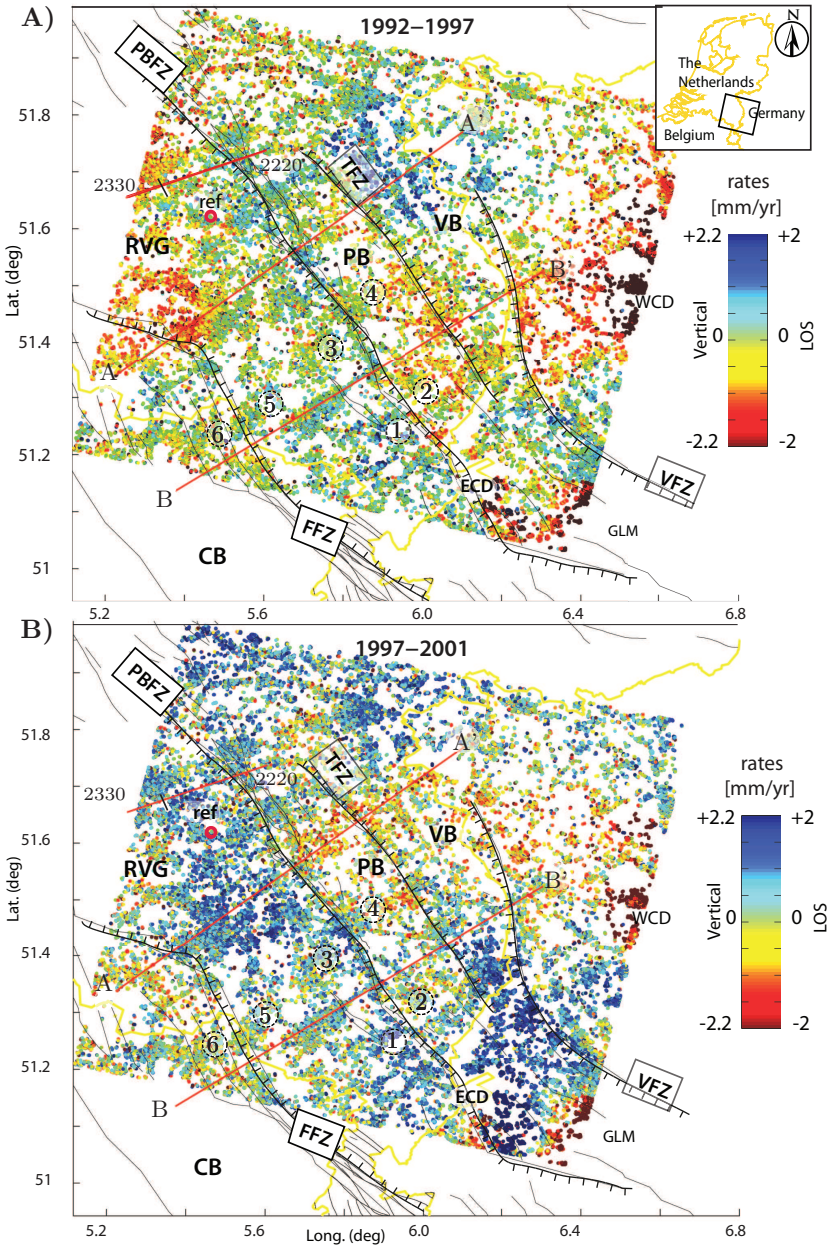

Fig. 5.1. Deformation rates estimated for three periods A) 1992-1997, B) 1997-2001, C) 2004-2010. The color-scale is saturated for visualization. LOS and vertical values are shown with the same color scale.

Period 1997-2001

The uplift motion that affected the Roer Valley Graben in the previous period, is still observed from 1997 to 2001, see fig 5.1B. The motion is also bounded by tectonic faults

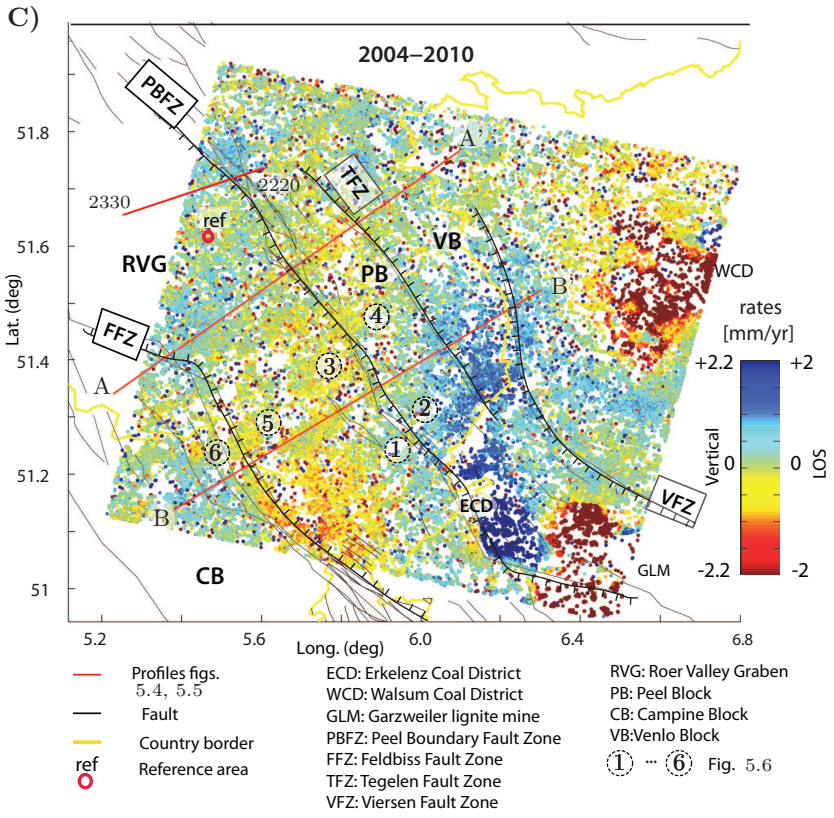

Fig. 5.1. continued

and appears to be more visible in areas 3-4. We explain this signal as we did before: to be caused by pore pressure increase in underneath aquifers. In this period, the motion is more uniformly distributed over the entire graben and with higher rates compared with 1992-1997. On average, the displacement rate of most of the graben is about +1 mm/yr with respect to the Campine Block and the central and northern sides of the Peel Block. The estimated precision, fig. 5.3B, is on average 0.3 mm/yr, for those areas, less than the rates. However, the estimated standard deviations are now larger when compared with previous period because of the smaller number of observations, i.e. interferograms. We use 43 for 1992-1997 and 31 for this period.

Apart from the displacements in the graben we observe other signals, as well. The velocity field shows the southern side of the Peel Block to uplift (relative to the reference area). This signal matches in space and time with the cease of pumping in the Erkelenz Coal District (Oct. 1997) in the southern side of the Peel Block. Therefore, it is very likely that pore pressure increase due to rising mine water[1] leads to surface uplift (Heitfeld et al., 2002; Caro Cuenca and Hanssen, 2011). Similar situations, cease of water pumping leading to surface uplift, have been reported in previous studies for other areas near the graben, e.g., the coal mines of south Limburg (Pöttgens, 1985; Heitfeld et al., 2002) see map in fig. 2.8.

[1]The terms mine water and groundwater are used interchangeably in this chapter.

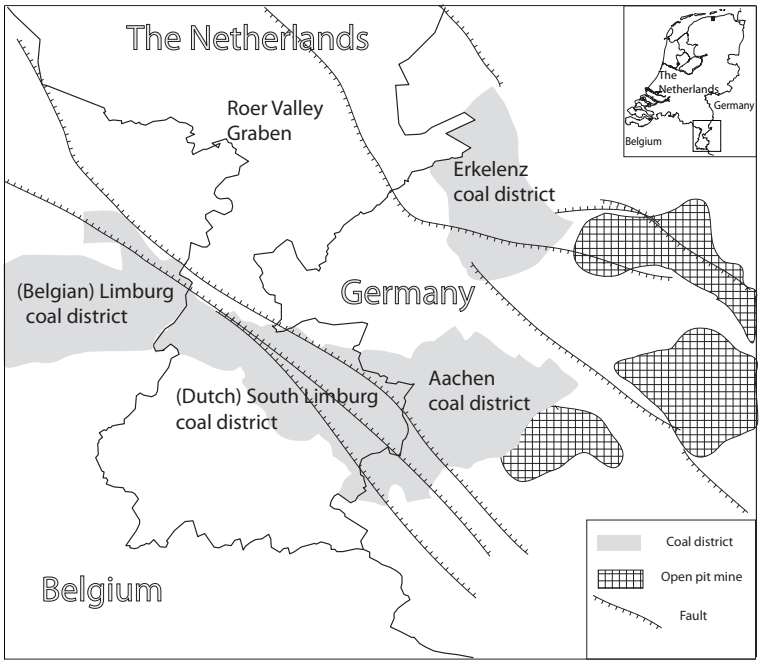

Fig. 5.2. Coal fields adjacent to the Roer Valley Graben, modified after TNO (1999), Heitfeld et al. (2002) and Devleeschouwer et al. (2008). German open pit lignite mines are also shown, as water pumping in these areas may influence the surface motion detected in the graben.

Deformation in the mines of south Limburg is the other signal of interest of this research. Chapter 6 is dedicated to describe this phenomenon as observed by PSI.

In the southern Peel Block, average displacement rates are up to $\sim +10$ mm/yr. The uplift seems to spread north-west, in the direction of the Venlo Block, suggesting the direction of the groundwater flow. This signal reaches a distance of about 30 km away from the center of Erkelenz. However, in the south of the Erkelenz coal district, the signal is bounded by the Peel Boundary Fault Zone. The spatial similarities between the uplift signal found in the graben (mentioned at the beginning of this section) and the uplift in Erkelenz, suggest that they are both produced by similar mechanisms, which seems to be pore pressure increase in underneath aquifers.

Period 2004-2010

In the time span from 2004 to 2010, the behavior of the graben relative to the adjacent horsts changes. A subsidence signal overcomes the uplift motion that was observed in the graben in previous periods, see fig. 5.1C. Maximum subsidence values (with respect to the reference area) appear in the south west of the graben in an area adjacent to the Campine Block (south to areas 5 and 6). The origin of this deformation signal is not clear. Based on previous arguments, it seems likely that the signal is produced by groundwater flow fluctuations. In fact, the Belgian mining industry, which is located in the Campine Block to the south of the study area, stopped groundwater pumping in the 1990's (Devleeschouwer

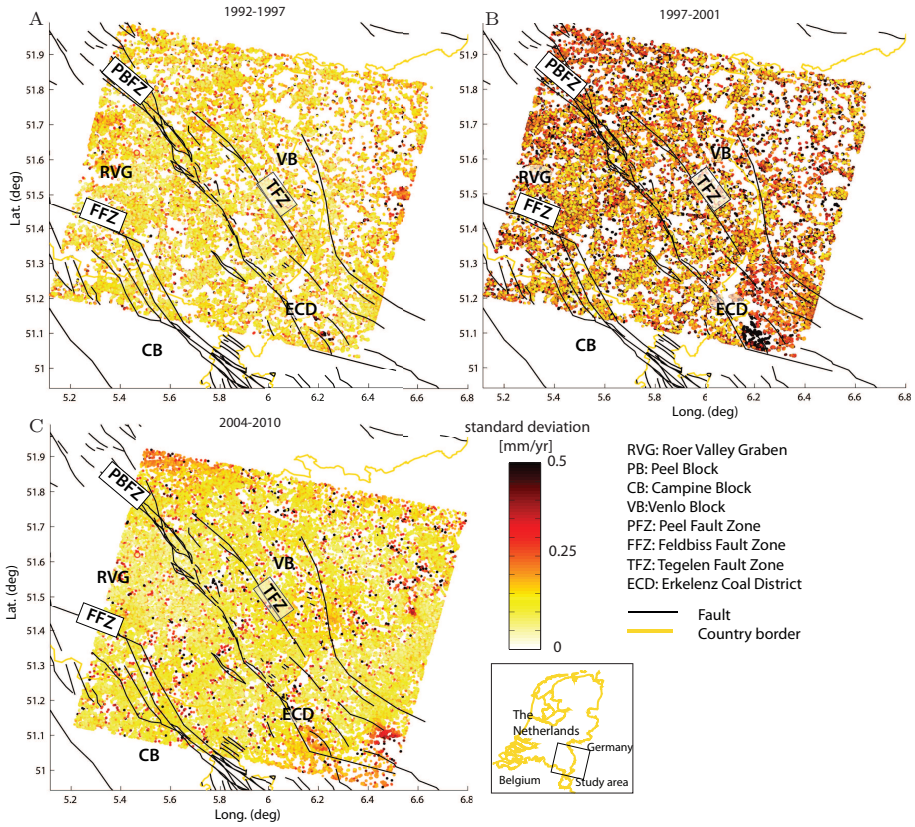

Fig. 5.3. Precision (1σ) estimated for the rates obtained with PSI (see fig. 5.1) for three periods A) 1992-1997, B) 1997-2001, C) 2004-2010. Notice that the ground coverage is slightly different in 2004-2010. Envisat swath is south-east of ERS1/2 acquisitions. The color-scale is saturated for visualization.

et al., 2008). In any case, a tectonic cause, such as a slip in the Feldbiss Fault, cannot be definetly ruled-out.

In other areas, the origin of surface displacements is more evident as we find the motion to correlate with the location of the mining industry.

The area of the Erkelenz coal district, located in the Peel Block, uplifts with respect to the graben. This signal seems very likely to be caused by the water rebound effect described above for the period 1997-2001. Water pumping ceased in this coal mine in 1997. Comparing the current period with the results of 1997-2001, the signal in Erkelenz is now larger in extent and affects now most of the central side of the Peel Block. This suggests that water flows in N-S direction. Due to the water rebound effect the Peel block appears to uplift in the area around Erkelenz, even at distance of 20 km from the presumable pump location. The displacements of the Peel Block with respect to the Roer Valley Graben show maximum uplifting rates near the Erkelenz coal district with average

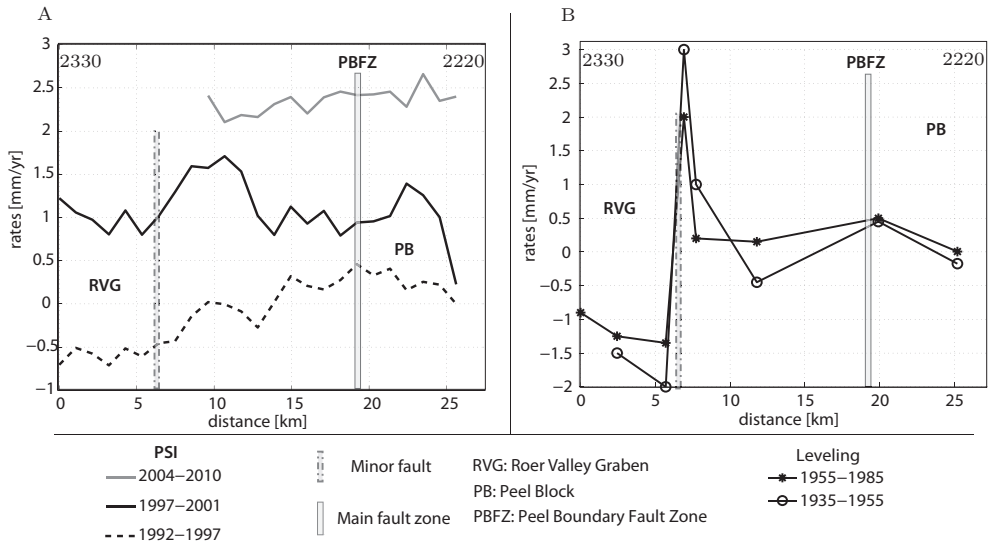

Fig. 5.4. Profile of LOS displacement rates estimated over 1992-1997, 1997-2001 and 2004-2010 across the Peel Boundary Fault Zone between two leveling benchmarks (2330-2220). The location is indicated in fig. 5.1, A) PSI estimates with arbitrary offsets added to each period, B) Leveling estimates (Groenewoud et al., 1991) .

values of around +5 mm/yr.

The other two mining areas that are covered in this data frame (Garzweiler and Walsum indicated as GLM and WCD in fig. 5.1, respectively) still produce large displacement fields, suggesting water pumping continues in the years 2004-2010. Notice that the spatial coverage of this period slightly changed and could give the impression that the subsidence in these mining areas increased in extent.

5.2.1 Profiles

The relative rate difference between the Roer Valley Graben and adjacent horsts becomes more apparent through profile sections. We draw three profiles lines for the rate maps. The profiles cross the main fault zones and their location are indicated with 2330–2220, A-A' and B-B' in fig. 5.1.

The profile values are calculated by grouping in bins the PS that lie at a distance less than 2 km from a desired profile line. The average displacement rates of each bin is then calculated. The results are plotted in figs. 5.4 and 5.5. They include the location of main fault zones displayed as a gray thin box. Vertical offsets are added to each period graph to ease visualization.

In general, we do not observe from the profiles any significant indication of faulting. Although in several occasions we detect spatial variations in the rates associated to main fault zones, this signal seems to be mostly related to groundwater flow. Let us discuss it in more detail.

The profile of fig. 5.4A is drawn between two leveling benchmarks (2330-2220) to be able to compare it with the leveling line of fig. 2.6 where the observed displacement was attributed

to tectonics (Groenewoud et al., 1991; Houtgast et al., 2003). These leveling results were discussed in section 2.2.2, repeated in 5.4B in the form of annual rates for convenience. In fig. 5.4, we also change the location of the Peel Boundary Fault Zone, which seems to be misplaced in fig. 2.6. The original figure displayed the location of what appears to be a minor fault inside the graben, see fig. 2.4.

The large values observed with leveling for this minor fault, are not detected by PSI. Although the leveling line covers a different time period (1926-1987) to InSAR observations (1992-2010), the strong signal is observed with leveling over sixty years, if caused by faulting, should also be observed in the InSAR time frame. The overall pattern does not reveal either any clear correlation with fault location. In the period 1992-1997, the estimated rates increase in the direction of the Peel Block. However, in the location of the Peel Bondary Fault Zone is, we do not detect any considerable gradient in displacements. We detect a similar situation for the periods 1997-2001 and 2004-2010, where we do not observe any significant signal across the Peel Boundary Fault Zone.

The differences between leveling and PSI do not seem related to the fact that the tecniques measure different objects. Meanwhile, leveling benchmarks are located at deep founded objects, PS includes both object types, shallow and deep founded scatterers. To study the influence of the foundation depth on our estimates we perform an initial classification based estimated heights. PS located at a height 6 meters above ground PS are assumed to be at a building rooftop and with deep foundations. PS at a height below this value are assume to be located near the surface. However, we do not find any significant differences between rooftop and ground PS. Therefore, we assume that displacement signal that we observe has an origin deeper than building foundations. Thus, the results reported in this study include all observed PS and do not classify them based on heights.

The profiles of fig. 5.5, being longer, provide a more suitable overview of the motion of the graben. The signal observed in profile A–A', although controlled by faults, cannot be ascribed to tectonics, because it is opposite to expected faulting. In the period 1992-1997, the rates increase in the direction from A to A'. This trend is however not constant and minimum values appear near both fault zones. Although the Peel block uplifts with respect to the Roer Valley Graben (with average rates +0.8 mm/yr), the graben appears also to uplift with respect to the Campine Block, in this case at a rate of around +0.3 mm/yr. In the period 1997-2001, the graben segment of A–A' clearly uplifts with respect to adjacent horsts at a rate of about +1.1 mm/yr. Also in this case, the displacement signal appears bounded by the Feldbiss and Peel Boundary fault zones. In the last period, 2004-2010, although the differences between the graben and horsts decrease we still observe the graben to uplift.

The profile B–B' is near the coal district of Erkelenz, see location in fig. 5.1 and therefore shows the effect of this mine closure after 1997. In this profile, we observe the graben to uplift with respect to both the Peel and Campine blocks at average rates of about +0.7 mm/yr and +0.4 mm/yr, respectively, for the time span 1992-1997. This signal decreases with time and we find that, for 1997-2001, on average the graben segment does not show almost any significant difference when compared to the Peel Block. This is probably a consequence of the cease of pumping in the Erkelenz coal district, which overcomes the uplift signal of the graben that we detect in the period 1992-1997. Comparing the graben with the Campine Block, we find the graben to uplift with values +0.4 mm/yr for 1997-2001. For the period 2004-2010, we detect the Roer Valley Graben to change behavior in the profile B–B'. The graben segment of profile B–B' appears to subside at average values of −0.8 mm/yr and −0.5 mm/yr with respect to the Campine and Peel blocks, respectively. The cause of displacements in the Peel Block and Venlo Graben appears to

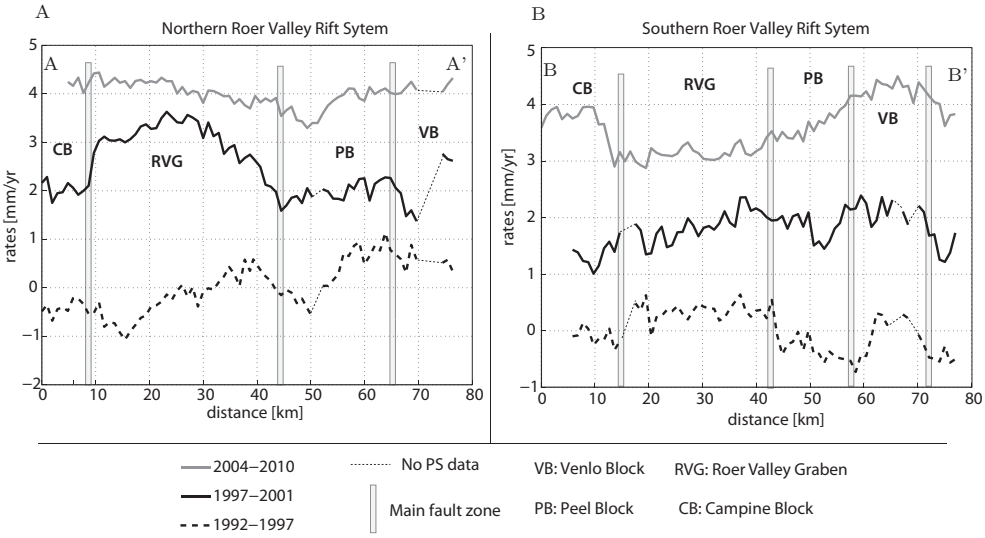

Fig. 5.5. Profile of LOS displacement rates estimated over 1992-1997, 1997-2001 and 2004-2010 across the Roer Valley Rift System, arbitrary offsets added to each period. Profile location is indicated in fig. 5.1.

be groundwater flow. We observe both structures to uplift after the cessation of water pumping in the Erkelenz Coal District, see also fig. 5.1. As discussed in previous sections, the origin of the uplift signal observed in the Campine Block is less clear. Although a slip of the Feldbiss fault could explain the signal, the most likely cause seems to be again fluctuations in the groundwater flow. Belgian mines stopped water pumping in the 1990's and a water rebound effect similar to the one detected in Erkelenz, may spread towards the north of the Campine Block.

5.2.2 Time series

With the goal of observing the global behavior of the graben with time, we combine ERS1/2 and Envisat time series using the algorithm described in section 4.4, assuming the same temporal model (a combination of third order polynomial plus a seasonal model) for all periods.

Since we focus on the relative motion between graben and horsts, we calculate the displacement time series of different areas in the graben with respect to adjacent blocks. The results are shown in fig. 5.6. The time series 1–2 represents the average displacement of area 1, in the Roer valley graben, with respect to area 2, in the Peel Block. The areas are both 1 km radius. Their location are displayed in fig. 5.1. Similarly, time series 3–4, represent the displacement of area 3 (graben) with respect to area 4 (Peel Block), and time series 5–6 shows the displacement of area 5 (graben) with respect to area 6 (Campine Block). Time series values errors represent the average standard deviation of the displacement of each area pair. The error bars of fig. 5.1 show the 1σ value. Linear displacement rates and corresponding precision are also indicated in the figure for each period and studied area. The modeled signal, which includes a linear motion plus periodic effect, is displayed as a solid gray line, with the exception of the data gaps where the model is shown as a dashed

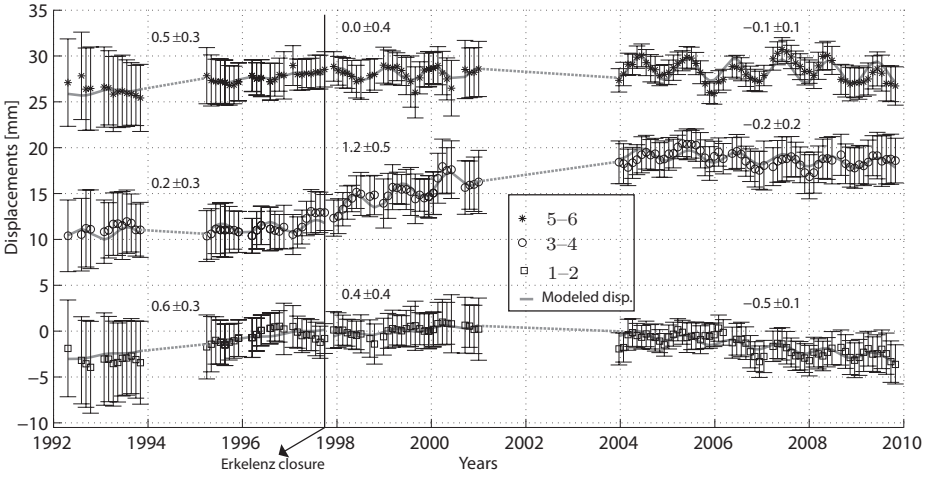

Fig. 5.6. LOS surface displacements in the Roer Valley Graben with respect to the Peel Block (1–2 and 3–4) and the Campine blocks (5–6). Displacements values represent the average of an area of 1 km radius. Error bars (1σ) are obtained from the standard deviation of the estimated displacements inside the 1 km radius area. Model displacements, a combination of linear and seasonal signals, are shown in gray. Linear rates in mm/yr are indicated for each time series and studied period along with its estimated precision.

gray line.

For the time span prior to the year 2001, the Roer Valley Graben appear to be stable or uplift with respect to both the Peel and Campine blocks. The estimated rates for this time span vary from +0.0±0.4 mm/yr to 1.2±0.5 mm/yr. In fig. 5.6 we mark the date of the closure of the Erkelenz coal district (the cease of water pumping in this year should result to uplift in the Peel Block). We observe that the consequent cease of the water pumping slightly affects time series 1–2, which are at about 25 km from Erkelenz, as the vertical motion the graben (area 1) with respect to the horsts (area 2) decreases. On the other hand from the time series 3–4 we observe an increase in the graben rates by the end of 1997. Although the acceleration matches in time with the mine closure it is unlikely that they are connected. We expect the opposite effect, a decrease in the uplifting rates as we see for time series 1–2, because area 4 in the Peel Block is expected to heave.

After 2004, the relative motion between graben and horsts changes to become relatively stable or even behaving opposite as previously described. Two of the areas (3-4 and 5-6) do not show any significant displacement for the graben with rates of -0.1±0.1 mm/yr and -0.2±0.2 mm/yr. However, in the area 1-2, the graben appear to subside. The subsidence of the graben with respect of the Peel block is caused by the pore pressure increase consequence of the abandonment of the Erkelenz coal district, see section 5.2.

In summary, time series confirm what was discussed in previous sections: The behavior of the Roer Valley Graben, that initially is in contradiction to expected tectonics, varies with time as a consequence of variation in the water extraction in the mining industry. The time series also give us confidence in our estimates, because they do not show unwrapping errors (equivalent to a jump of 28 mm) or other noise sources that could indicate an error

in the rate estimations.

5.3 Ground water levels variations as a cause for surface displacements in the Roer Valley Graben

In order to further investigate the driving mechanism behind the displacements observed in the Roer Valley Graben, we calculate the correlation of surface deformation with groundwater levels which are provided in TNO (2010). The water wells are relatively shallow with an average depth of 40 m, and a maximum depth of about 200 m. We determine the correlation coefficient only in the locations where we have both PSI and water level observations. Water values are then interpolated in time at radar acquisition dates, because of the high frequency of water measurements. After that, we interpolate the estimated correlation in a uniform grid to easy visualization and posterior analysis.
The results for each studied period are displayed in fig 5.7. We observe that the correlation with water levels changes with time. The period from 1992-1997 shows the highest correlation values. This suggests that an important part of the displacements observed in this period is caused by pore pressure changes in shallow aquifers. The most likely mechanism driving pore pressure variations in these aquifers is water pumping in the German lignite mines. The mines include the Garzweiler pit and three more extraction areas located to the south. Different studies (van Bracht, 2001; Bense et al., 2003; Bense, 2004) have shown the influence of these mines on groundwater flow at large distances ($\sim$40 km) from the source.

Figure 5.8 (van Bracht, 2001) shows the effect of changes in pumping rates on several aquifers in the graben. The water levels are measured at three different aquifers at a depth of about 20 m for well 1, 100 m for well 2 and 200 m for well 3. Pumping in the lignite mines occurred at a depth of about 200 m and therefore its effect is directly observed in well 3, which corresponds to the same aquifer. Effectively, the decline in water levels in this well (3) is caused by pumping in the lignite mines that propagates through this confined aquifer (van Bracht, 2001). Before 1992, we observe that upper aquifers (wells 1 and 2) are also affected due to the extreme pumping rates, despite the fact of being separated by aquitards. This situation changes in 1992, when the extraction rates decrease. The measurements in well 3, at the same level of pumping, show the water levels of this aquifer to be stable in the long term. In the short term, we observe a periodical signal due to seasonal recharges. In upper aquifers, as indicated by wells 1 and 2 in fig. 5.8, the decrease in pumping rates in 1992 translates in a increase in water levels.

The increase in water levels, and consequent increase in pore pressure, for the aquifers of wells 1 and 2, could explain the uplift signal in the graben from 1992 to 1997. The increase in pore pressure in aquifers 1 and 2 can produce surface uplift, see section 5.2, as the aquifers deform and increase in volume. Based on the correlation and the water levels time series, we conclude that the displacements measured in the Roer Valley Graben for the time span 1992-1997 seems to be controlled mainly by pore pressure increase in shallow aquifers.

However, for the next two periods (1997-2001 and 2004-2010), we do not observe correlation between surface displacement and shallow (less than 200 m deep) ground water variations, see figs. 5.7B and C. The low correlation suggests that pore pressure changes in shallow aquifers are not the source of displacements in this time span (from 1997 to 2010). Nevertheless, pore pressure changes not at shallow but at deep confined aquifers can still be the cause of deformation. In fact underground mining, and required water pumping, in the Roer area can reach depths of 800 m. For example, this is the case of the Erkelenz coal district, whose maximum depth is around 800 m and where water pumping stopped

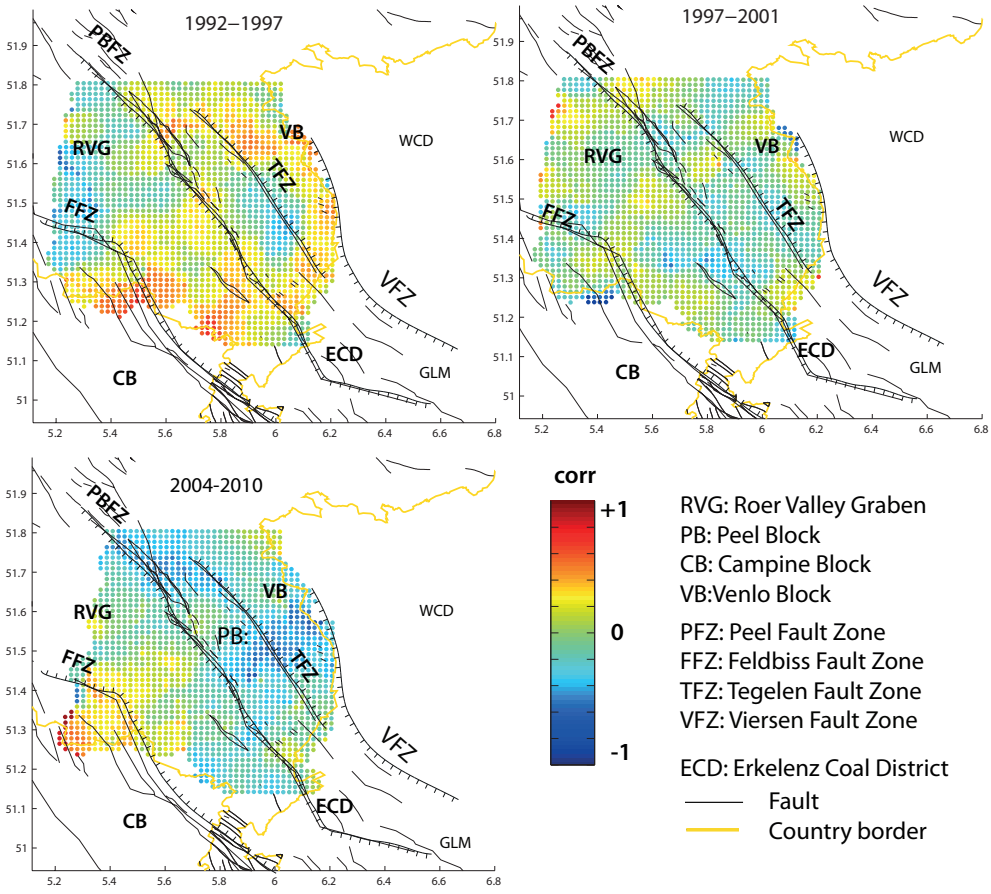

Fig. 5.7. Correlation between underground water levels (average depth of 40 m) and PSI time series. Values initially calculated at well location are spatially interpolated for clarity.

in 1997.

5.4 Fault mapping from rate estimations

In previous sections, we analyzed a displacement signal that appears to be related to pore pressure variations due to water flow and to be bounded by faults. Other deformation signals can be controlled by tectonic faults as well. Examples of these type of phenomena are not only slip events but displacements produced by different fluid flow, not only water. We can observe high deformation gradients across faults in other situations such as gas extraction, oil production or CO2 injection.

Conversely, this information can be also exploited for fault mapping. Places with high displacement gradients give an indication of the presence of a fault. In this section, we

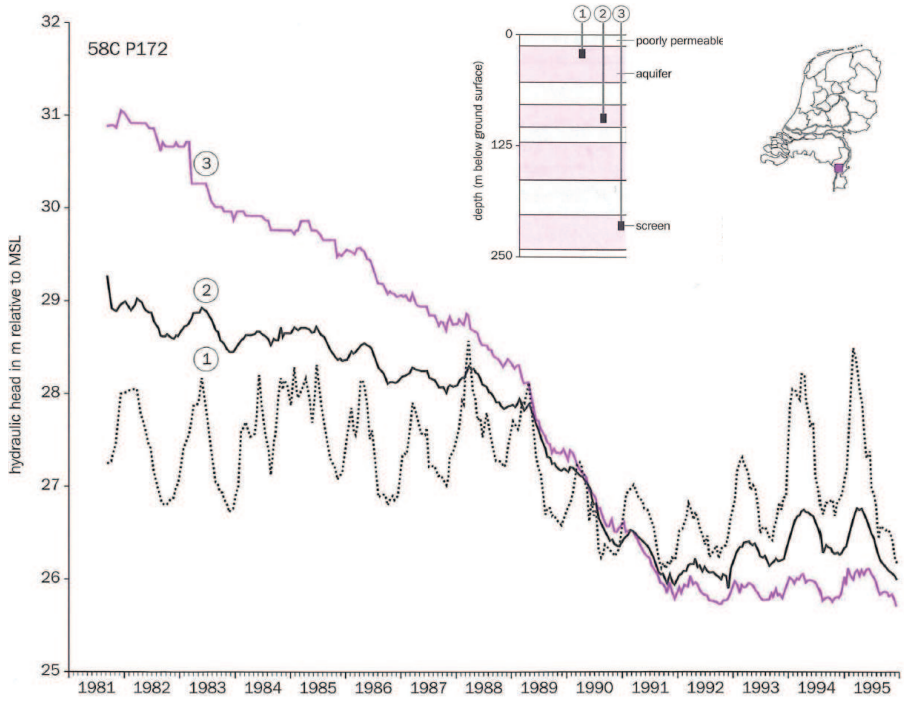

Fig. 5.8. Water levels in a well in the Roer Valley Graben with filters at three aquifers at a depth of 20 m, 100 m and 200 m. Water pumping is performed by lignite mines located at 40 km east of the well. In these mines water is extracted at a depth of ∼200 m, but the effect propagates to upper aquifers. Pumping rates decreased in 1992. Since then water levels appear to be stable for well 3 (200 m deep) or even increase for upper aquifers, from van Bracht (2001).

explore an algorithm that uses the displacement rates observed with PSI for fault mapping.

This method calculates first the mean displacement rate value for two neighboring areas, denoted as v_{block1} and v_{block2}, see fig. 5.9. These means are compared using the Student's test (Fisher, 1925) to decide if the differences can be judged to be significant considering their standard deviations, denoted σ_{block1} and σ_{block2}, respectively. When this is the case, i.e. the means are unlike, we assume that a tectonic fault is the cause of the differences.

The Student's test is given by

$$T = \frac{v_{\text{block1}} - v_{\text{block2}}}{\sqrt{\sigma^2_{\text{block1}} + \sigma^2_{\text{block2}}}}. \tag{5.6}$$

The test T follows a Student's distribution with $n_1 + n_2 - 2$ degrees of freedom being n_1 and n_2 the number of PS inside window 1 and window 2, respectively. A critical value $k_{\frac{\alpha}{2}}$ can be determined based on a desired level of significance α. Since the Student's distribution in eq. (5.6) is double-tailed, to obtain $k_{\frac{\alpha}{2}}$, α must be equally distributed in both sides of the distribution, see fig. 5.9. If $\mid T \mid$ exceeds $\mid k_{\frac{\alpha}{2}} \mid$ the differences between the means

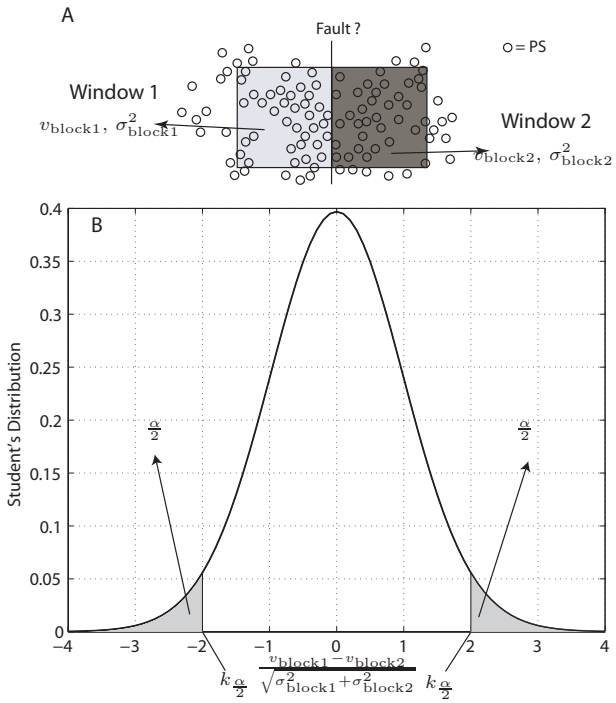

Fig. 5.9. Method for fault mapping. The mean of the rates of two adjacent rectangular windows are compared ($v_{\text{block1}} - v_{\text{block2}}$) to judge if the difference is significant. The ratio of $\frac{v_{\text{block1}} - v_{\text{block2}}}{\sqrt{\sigma^2_{\text{block1}} + \sigma^2_{\text{block2}}}}$ follows a Student's distribution. A critical value can be determined from the desired level of significance α.

$v_{\text{block1}} - v_{\text{block2}}$ are judged significant and assumed to be caused by a fault.

These operations are repeated for window-pairs uniformly distributed over the area of interest. For each window pair location, different orientations are also tested, by rotating the windows around the desired location. In the case where a fault is detected, its orientation is given by the direction perpendicular to the angle where the gradients are maximum.

5.4.1 Fault mapping method applied to the Roer Valley Rift System

We apply the method for fault mapping to the rates estimated with PSI. We select a relatively large level of significance of $\alpha = 35\%$ to decrease type II errors. Type II errors occur when null hypothesis ($v_{\text{block1}} = v_{\text{block2}}$) is accepted when in fact, it is not true ($v_{\text{block1}} \neq v_{\text{block2}}$).
We test with different window sizes, varying from 10×10 km^2 to 4×4 km^2 to take into account variable distance between faults. Window pairs are uniformly distributed all over the study area with spacing of 2 km. We test as well different orientations varying at intervals of 30^o from 0^o to 180^o with respect to north.

The results of the test statistics are shown in fig. 5.10. The places where the differences

between the averages $v_{\text{block1}} - v_{\text{block2}}$ are judged to be significant ($\mid T \mid$ is larger than the critical value) are shown with a colored dot and a black line. It is worth notting that, these locations not only represent the estimated fault location, but also indicate the places where the relative motion between the horst and the graben is judged to be significant.

The colorbar represents the absolute of the differences in the logarithmic scale ($\log|v_{\text{block1}} - v_{\text{block2}}|$), which is used for the sake of visualization. The black lines show the estimated fault orientation using the angle where the difference $|v_{\text{block1}} - v_{\text{block2}}|$ are maximum.

The algorithm estimates fault locations along the Peel Boundary Fault Zone, mainly in the south where large displacements are found. The rest of the Peel Boundary Fault Zone is mapped by our algorithm at scattered locations. In these places the relative motion of the graben with respect to the Peel Block is judged to be significant, given the estimation errors.

The Viersen fault zone seems particularly well mapped especially during 1997-2001. We also detect faults in the Walsum mining area, which were not included in our initial fault map. For the Walsum and Erkelenz coal district areas, our method estimates a cluster of faults that are not realistic but give still a good indication of fault location. These clusters appear due to a strong deformation that affects areas of extension smaller than the window size employed in the algorithm. If the grid spacing is small and the window-pairs cover an area larger than the spatial size of the displacement signal, the test T can be accepted for different nearby window-pairs. For these situations, the algorithm can still be improved, for example, by employing adaptive window sizes to avoid these fault clusters.

5.5 Summary and conclusions

The application of PSI to the Roer Valley Rift System reveals a signal that, although correlates with fault location, it does not seem to relate to tectonics but to underground water flow for two main reasons. First, the initial behavior observed from 1992 to 2001 contradicted tectonics, because the Roer Valley Graben uplifted with respect to adjacent horsts. Second, the displacement field appears to be strongly influenced by pore pressure variations in underneath aquifers that are caused by water flow produced by nearby mining areas.

Therefore, PSI results suggest that the differences on graben slip rates when estimated at short and geological time scales are likely to be caused by pore pressure changes. The effect of groundwater variations on surface displacements was already recognized in Demoulin (2006). However, the estimation of Demoulin (2006) only took into account the three upper aquifers and not deeper ones. Our analysis proves that pore pressure variations at deeper depths can still play an important role in surface deformation. We observe strong surface deformation in places, e.g., the Erkelenz coal district, where water was pumped out at depths of 800 m.

The comparison between PSI estimates and the values provided by other techniques measuring at short time scale (leveling) show large differences. In particular, we compared PSI results with the leveling line 2330-2220, see fig. 5.4. In contrast to leveling, we do not observe major variations in displacement rates near faults. Both results may be complex to compare because the last leveling campaign of fig. 5.4 was in 1987 and the first radar image was acquired 5 years later, in 1992. However, it is very unlikely that the strong signal that was observed with leveling from 1926 till 1987 to be caused by faulting because it completely disappeared in a decade.

Since the number of observations in time and space is much higher in PSI than in leveling,

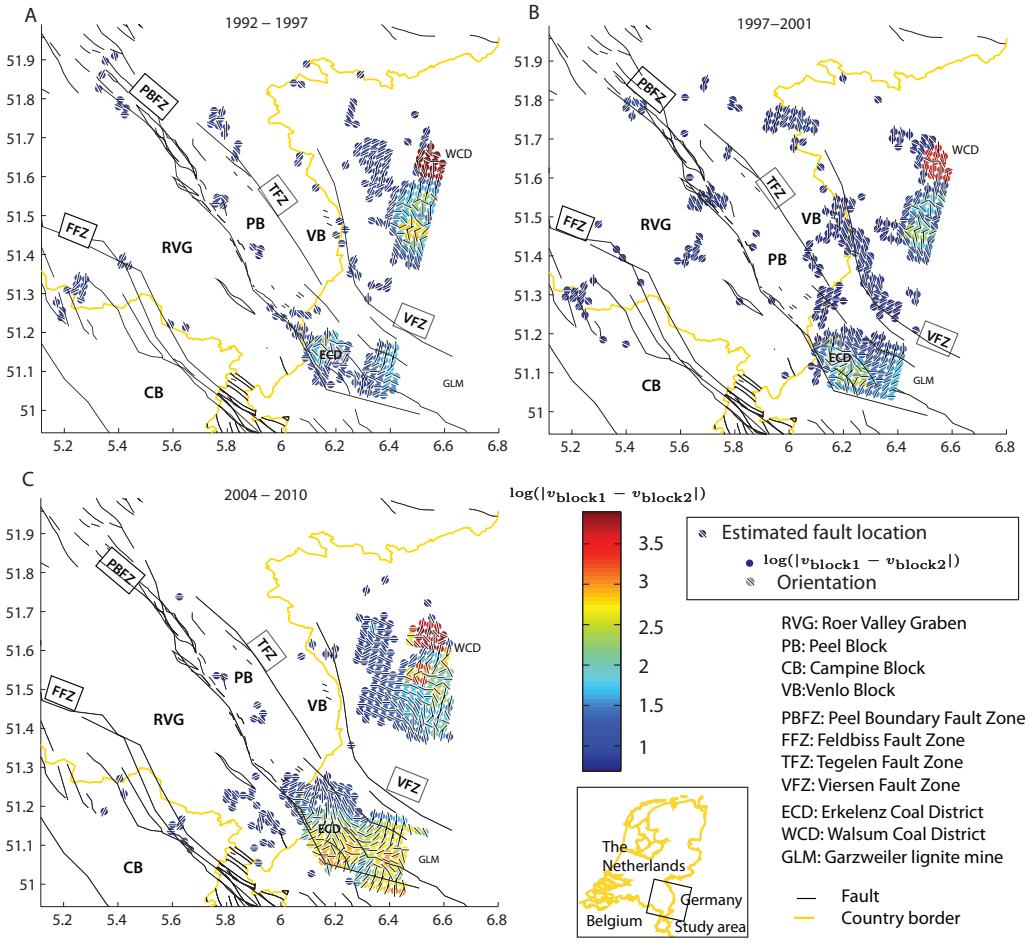

Fig. 5.10. Method for fault mapping applied to the Roer Valley Rift System. The pairs circle with black lines indicate the places where a fault is detected, where the black-and-white lines represent the estimated orientation. The color of the circles represent the log($|\, v_{\text{block1}} - v_{\text{block2}} \,|$). A logarithmic scale is used to be able to display the full range of values of $v_{\text{block1}} - v_{\text{block2}}$.

and we do not find any significant indication of tectonic signal with PSI, the results suggest that the leveling line 2330-2220 does not show a tectonic subsidence but a signal that could be either an erroneous estimate, e.g., caused by outliers, or produced by other phenomenon not related to tectonics, such as underground water flow.

Due to the large influence of other signals, detecting Neotectonic motion at short time scales seems a very complicated task. Surface displacements are very likely to be dominated by displacement signals other than tectonics, which can be one order of magnitude higher than expected slip rates and that appear to be mainly caused by pore pressure changes. Modeling and removing these signals seem essential requirements for faulting rates estimates.

Although, modeling these signals is beyond the scope of this research, we suggest some prerequisites that may be needed for this task. For example, long time series, high density of observations and large coverage are required, as pore pressure variations appear to affect for decades large areas and can vary quickly in space in the presence of tectonic faults. Furthermore, measurements of groundwater levels at different depths, not only shallow, are also needed to model displacements caused by pore pressure changes, as we saw that water pumping at depths deeper than 200 m and 40 km away from the pump resulted in surface displacements.

Apart from the analysis of the displacement field, we investigated in this chapter how to extract fault location from velocity maps, taking advantage of the fact that the displacement field correlated with faults. We provided a method for fault mapping that used the displacement differences of two adjacent areas of predefined size. If the relative motion between these areas were judged to be significant based on test statistics, then a fault was assumed to be detected. We applied it to the Roer Valley Rift System, we saw that our method estimated fault location that matched previously known faults, also when small gradients occurred.

Chapter 6

Surface Deformation in the Dutch Coal Field Observed by PSI

6.1 Introduction

This chapter[1] is dedicated to analyze the results of applying PSI to the coal field of the southern Netherlands. Although, chapter 2 already described the Dutch coal mine industry and its possible effect on surface deformation, let us briefly recall the most relevant facts concerning the land motion in this area.

The southern Netherlands contains one of the largest abandoned mining regions in Europe where the coal was exploited for many centuries. The long-term intensive extraction resulted in a ground subsidence of several meters (Pöttgens, 1985). This was produced by two different causes: mineral extraction and groundwater pumping. The partial collapse of galleries after the actual extraction of coal reduced support of the upper layers producing surface subsidence. Additionally, since this process required dry working environment, groundwater was continuously drained. Water pumping reduced rock pore pressure which also results in subsidence. Jointly with the adjacent coal district of Aachen, Germany, the Dutch and Germany mine industries have affected groundwater levels within an area of 400 km^2 (Wolkersdorfer, 2008).

Water pumping definitely stopped in these mining regions in 1994. Since then, the groundwater in the mines has being rising. In some areas in the west side of the Feldbiss fault, the increase on groundwater levels has already reached 200 m (Wings, 2006; Rosner, 2011). In the Dutch coal mines, groundwater flow is controlled by a subsurface dam system that was put in place when the Dutch mine were abandoned during the seventies to avoid flooding of operational German mines. As a result, the coal fields were divided into a series of water basins with galleries that connected the basins to the only remaining pump in the field. This situation is depicted in fig. 6.1 with the groundwater levels in 1994 also shown [2].
The pump was located in the shaft Beerenbosch II (eastern basin) and was eventually disabled early 1994 (Bekendam and Pöttgens, 1995). The cease of the pumping in this year led to a rapid groundwater level increase. During 1994 it rose from -235 m to −138 m NAP and started to overflow towards the central basin. The profile A–A' in fig. 6.1 shows the overflowing levels and the water regime at the time when the pump in Beerenbosch II was active, (Bekendam and Pöttgens, 1995). Several studies (e.g. Pöttgens (1985); Bekendam

[1] This study was published in the Journal of Applied Geophysics, see Caro Cuenca et al. (2012).
[2] Figure 6.1 was also displayed in chapter 2, repeated here for convenience

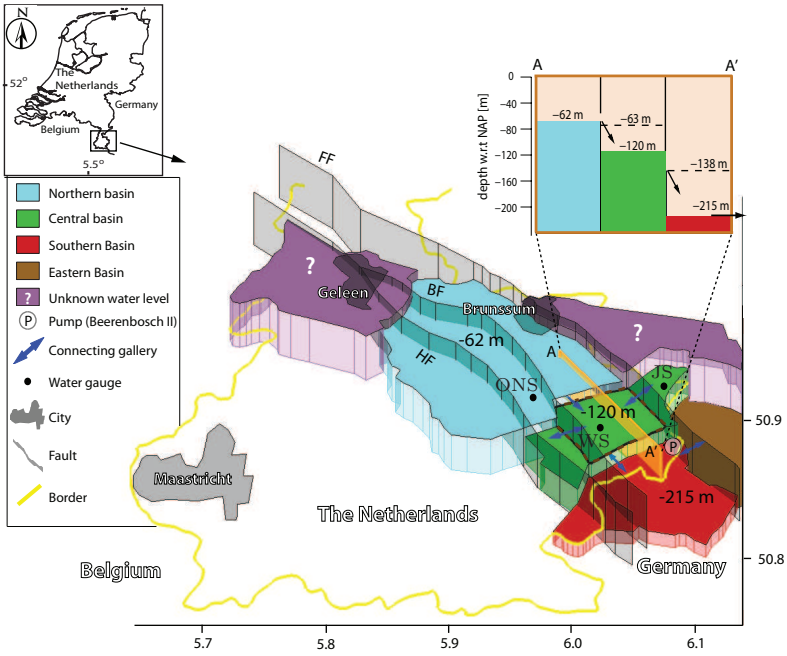

Fig. 6.1. The water basins in the Dutch and German coal regions with water levels as measured in 1994. The plotted thickness indicates the water level whose value is also indicated with respect to the vertical Dutch datum 'NAP', modified after Heitfeld et al. (2007). The profile A–A' shows the hydraulic connections between the northern, the central and southern water basins, modified after Bekendam and Pöttgens (1995).

and Pöttgens (1995); Donnelly and Rees (2001); Heitfeld et al. (2006); Rosner (2011)) have shown that mine water[3] rebound can result in surface uplift. In the Dutch coal mines, the deformation field produced by the groundwater influx is expected to be inhomogeneous, not only because of the network of mining galleries but also due to proximity of faults.

In this chapter, we discuss the results of applying PSI to the coal field of the southern Netherlands to study the effect of groundwater recharge on surface deformation. In particular we apply the extension to PSI that was described in chapter 4.

In section 6.2, we estimate and analyze the total deformation that occurred from 1992 to 2009. We then describe the spatio-temporal behavior of the deformation signal and its relationship with mine water levels in sections 6.2.2 and 6.3, respectively. The last part of the chapter is dedicated to model the volume change suffered by the mines from total surface displacements, see section 6.4.

[3]The terms mine water and groundwater are used interchangeably in this chapter.

6.2 Surface displacements observed by PSI

We processed almost 18 years of radar acquisitions to produce line of sight (LOS) displacement time series. We projected the LOS direction to vertical assuming vertical-only displacements, see section 3.2.1. The whole time span was initially divided into two stacks as provided by the European satellites ERS1/2 and Envisat. These two sets of displacement time series were low pass filtered in time and space to reduce noise. The time series were merged to produce longer time series from April 1992 to October 2009, see section 4.4. The procedure to join time series assumes that the deformation in ERS1/2 and Envisat times can be both described with the same model plus a vertical offset to compensate for the deformation that occurs between the two reference images (one from ERS1/2 and the other from Envisat). The estimated vertical offset is added to Envisat observations to produce the joined time series. The error of this estimated offset (1σ) was $\sim$4 mm or less for 95% of PS.

6.2.1 Cumulative displacements

The total displacement field estimated by PSI for the period spanning from April 1992 to October 2009 is displayed in fig. 6.2. The colored pixels represent those scatterers that are found to be coherent and selected as PS. They mostly relate to urban areas. The background picture is the corresponding time-averaged radar image. Estimated displacements are relative to a 1 km diameter area considered to be stable, centered at the village of Mechelen and displayed with a red circle in fig. 6.2. To reduce the influence of a single scatterer, we average the displacements of the PS inside this area.

Cumulative displacements are estimated by taking the differences of two periods assumed to represent the beginning and the end of the deformation signal. We average the measurements within the last period (June-October 2009) and compare it with the average of the time span from April 1992 to December 1993.
To describe the quality of surface displacements, we estimate the variance as well. The estimated variance is the sum of three terms: the variance of the displacements in the first period, the variance of the displacements in the last period and the (squared) 1σ error of joining ERS1/2 and Envisat time series, (see above). As displayed in fig. 6.3, the estimated standard deviation is around 7 mm or less for 95% of PS, which is rather acceptable because total displacements are one order of magnitude larger for the mining areas.

Figure 6.2 shows that most of the uplifting areas are within the coal field. Displacements are also bounded by faults, in some places, e.g., in Geleen and Brunssum [4] rather abruptly. This occurs when faults act as hydrological barrier, or when faults separate units with significantly different material properties, e.g., aquifers may not be found at the same depth at both sides of the fault.

The profiles shown in fig. 6.4 explore the influence of the faults on the displacement pattern. Note the data gaps in 1994, as a consequence of an orbital change in ERS1, and from 2001 to 2004, which was the time interval between a malfunctioning of ERS2 gyroscopes and the start of systematic data acquisition by Envisat.

In the cities of Geleen and Brunssum, the gradients are 135 mm and 90 mm over a distance of 2.5 km and 1.6 km, respectively, in 18 years. In addition to that, the north of Brunssum

[4] The mine concessions of Maurits and Oranje-Nassau correspond to the cities of Geleen and Brunssum.

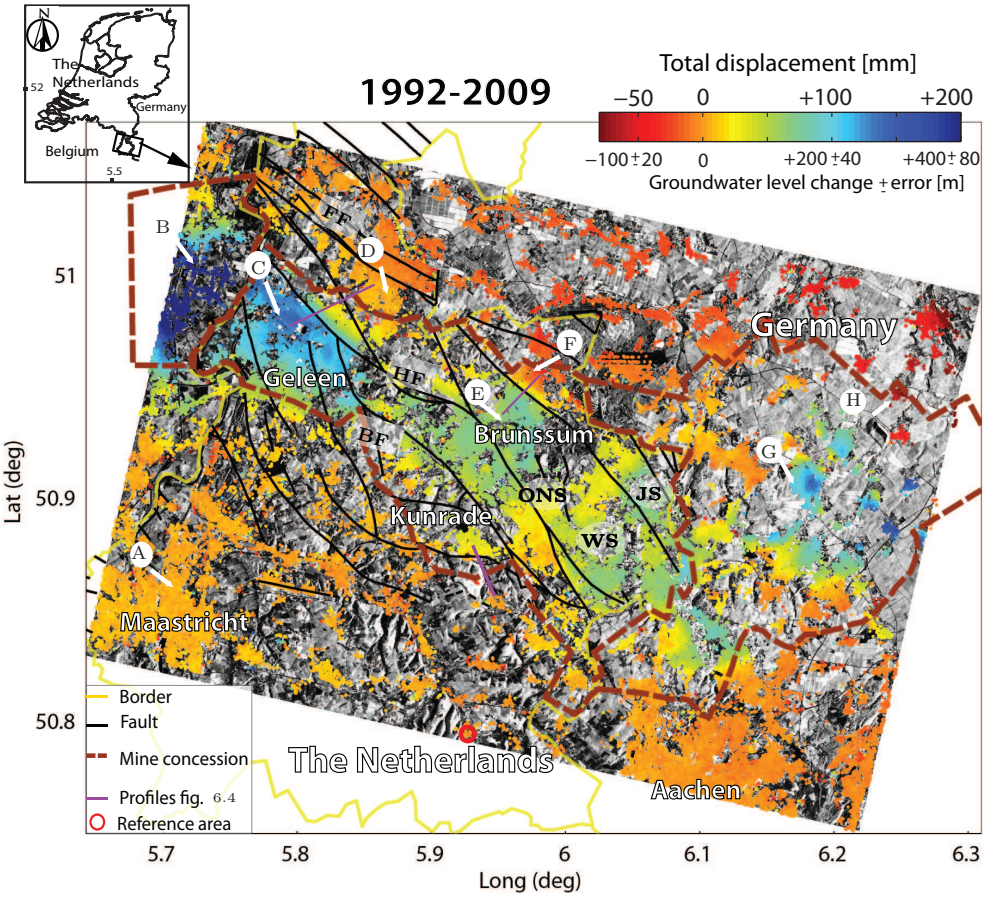

Fig. 6.2. Vertical cumulative displacement from 1992 to 2009 and estimated groundwater level change. A-H show location of fig. 6.5. ONS (Oranje Nassau Shaft), JS (Julia shaft) and WS (Wilhelmina shaft) indicate the location of the places where the water gauges were installed. FF, HF and BF shows the Feldbiss, Heerlerheide and Benzenrade faults, respectively.

is subsiding during the initial years of the time series, probably due to the influence of the open pit mines in Germany, where large amount of groundwater are pumped out (Bense et al., 2003). Further to the east of Brunssum and outside the area observed with InSAR, there are three major lignite mines[5], see fig. 5.2. After 2004, the situation in the north of Brunssum seems stable, which is coherent with the time series described in section 6.2.2.

In 2001, an earthquake swarm of low magnitude (from 1.5 to 3.9) was measured in the surroundings of Kunrade (KNMI, 2010). There were no clear indications that the motion was induced or related to the former mining activities. As can be seen from fig. 6.4C, the uplift in the mining area is relatively moderate compared with the other two profiles. The

[5]Chapter 5 also describes surface displacements caused by these lignite mines in the Roer Valley Graben area

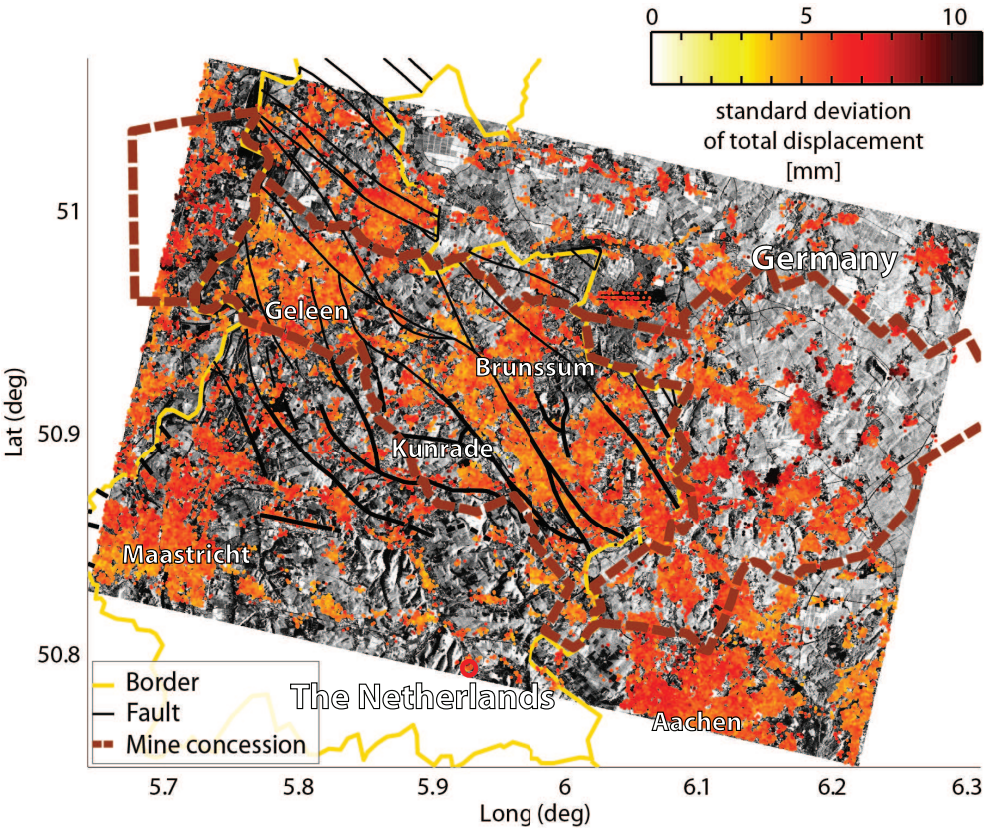

Fig. 6.3. Estimated standard deviation [mm] of cumulative displacements shown in fig. 6.2 (1992-2009).

influence of the fault is still visible; however, we do not detect any significant change in the deformation around the year of the earthquake swarm (2001).

Studying the whole displacement field, we observe that there are no apparent fully stable areas within the limits of the Dutch concessions, minimum uplift rates are around +20 mm. The maximum vertical displacement is registered in Geleen with a value of around +135 mm, equivalent to ∼8 mm/yr. Outside this area, in the Belgian coal field, the uplift reaches values of about +220 mm. In this case, groundwater pumping ceased during the early nineties, (Devleeschouwer et al., 2008).

In Germany, we find two distinct motions with opposite behavior. To the northeast side of fig. 6.2, the land subsides due to the influence of open pit mines, i.e. for the same reasons as in north Brunssum. On the other hand, the area north of Aachen shows a total cumulative displacement of around +75 mm. Again, this corresponds to abandoned coal mines; in this case closed in 1992, (Heitfeld et al., 2002).

In this section we have described the spatial variability of estimated displacements. In the following section we focus on their temporal behavior.

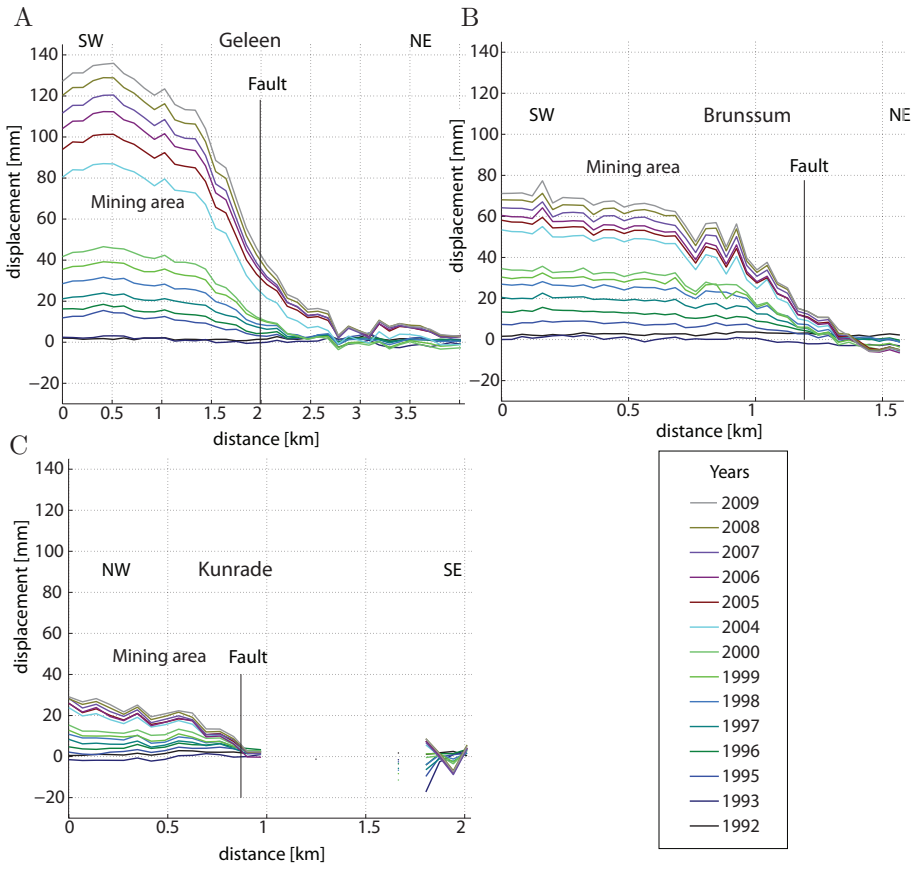

Fig. 6.4. Profile across the faults in the cities of Geleen (A) Brunssum (B) and Kunrade (C), showing yearly average displacements. The annual average is plotted. There are two data gaps in 1994 and from 2001 to 2004, (see text for explanation).

6.2.2 Deformation time series

Eight locations are selected to provide an overview of the displacements in the studied area. The corresponding time series are plotted in fig. 6.5. They were filtered in time and space to reduce noise [6]. ERS1/2 and Envisat time series are merged assuming that deformation signals can be described in time with a 3rd degree polynomial with a break point in 1994. The estimated standard deviation of an observation (PS displacement in a given time) is in the order of 5 mm plus the 1σ error of joining time series ($\sim$4 mm), which only affects the Envisat period. The locations of the time series are shown in fig. 6.2 by the letters A to H. Note that during 1994 and from 2001 to 2004 there were no acquisitions.
As expected, the selected time series show that the most stable areas are located outside the coal fields. The city of Maastricht (time series 6.5A), appears stable when compared

[6] In the time filter, we employed a moving average with a Gaussian window of 4 months. The filter in space was performed with kriging with an exponential variogram that had a range of $\sim$500 m.

with the mining areas. As discussed in section 6.2.1, the central and eastern side of the mine field experience the greatest cumulative uplift.

Time series 6.5B, C and E show the displacements of these areas. They correspond to the mine concessions of Eisden in Belgium, Maurits and Oranje-Nassau in the Netherlands (see, e.g., TNO (1999); van Tongeren and Dreesen (2004)). Time series 6.5B is located in the Belgian coal field and is not in hydrologic connection with the Dutch mines. From 1992 to 1994, time series 6.5B is stable, which is in agreement with the fact that the Belgian water pumps were still active until the early nineties (Devleeschouwer et al., 2008). After that the displacement accelerates very fast and uplifts for the rest of studied period. Time series 6.5C and E show the land displacement of the mine concessions in Geleen and Brunssum, respectively. The time series show stability until 1995, then an initial slow uplifting signal that accelerates around 1997 and 1998 in Brunssum and Geleen, respectively. After the acceleration, the surface starts to uplift almost linearly with time. The acceleration is probably caused by groundwater overflowing between basins. We explore further the hydraulic connection between Geleen and Brunssum areas and the pump in Beerenbosch II in section 6.3. The initial stability of the time series 6.5C (Geleen) suggesting that groundwater pumping influences over large distances.

From series 6.5D and F, we see that PS located outside the concession area and separated from the mining area by tectonic faults are not affected by the uplift, see also fig. 6.4.

Time series 6.5G is located in the German mining area. Here, the coal extraction stopped in 1992 (Heitfeld et al., 2002), but uplift started only after 2001. Presumably, this is because a possible groundwater rebound is compensated by the subsidence caused by groundwater pumping in other mines (the open pit mines) along with the residual subsidence from the mining, i.e. delayed reaction to the extraction, (residual subsidence is treated in, e.g., Blodgett and Kuipers (2002)). Groundwater induced uplift seemed to have taken over in 2004 when this area started to heave.

Time series 6.5H reflects the influence of groundwater extraction required for the operation of the open pit lignite mine located outside the radar images and to north-east of Aachen. The subsidence rate in fig. 6.5H decreased with time from around -10 mm/yr before 2001 to -1 mm/yr after 2004. This suggests that the pumping rate in the open pits mines decreased during this period.
Some of the time series display a periodic annual signal. This is visible in fig. 6.5G and H in particular after 2004. Periodic signals are produced by effects such as surface water variations due to seasonal evaporation and recharge or temperature changes (see e.g. Crosetto et al. (2011), van Leijen and Hanssen (2008) or Caro Cuenca and Hanssen (2008)). The amplitude of the periodic signal does not only depend on the geophysical properties of the signal itself but also on the scattering object (PS). For example, an object with deep foundations (e.g., a tall building) will not be influenced by a shallow seasonal motions. This is probably the cause of the differences between the periodic signal observed by Envisat (after 2004) and ERS1/2 (before 2001). The PS detected by one satellite are usually not the same as detected by another due to changes in terrain with time and differences in the viewing angle. As described above, time series were joined by spatially interpolating Envisat observations to the locations of PS detected by ERS1/2.

In Summary, time series derived from PSI observations show that the areas located within the bounds of the mine concessions appear to be under the influence of mine water recharge after pumping ceased. Time series located outside the mine limits appear to be stable in time. Inside the Dutch coal field, the acceleration experience by the time series seems to be area dependent. In the east part velocities increase around 1994; meanwhile the west areas

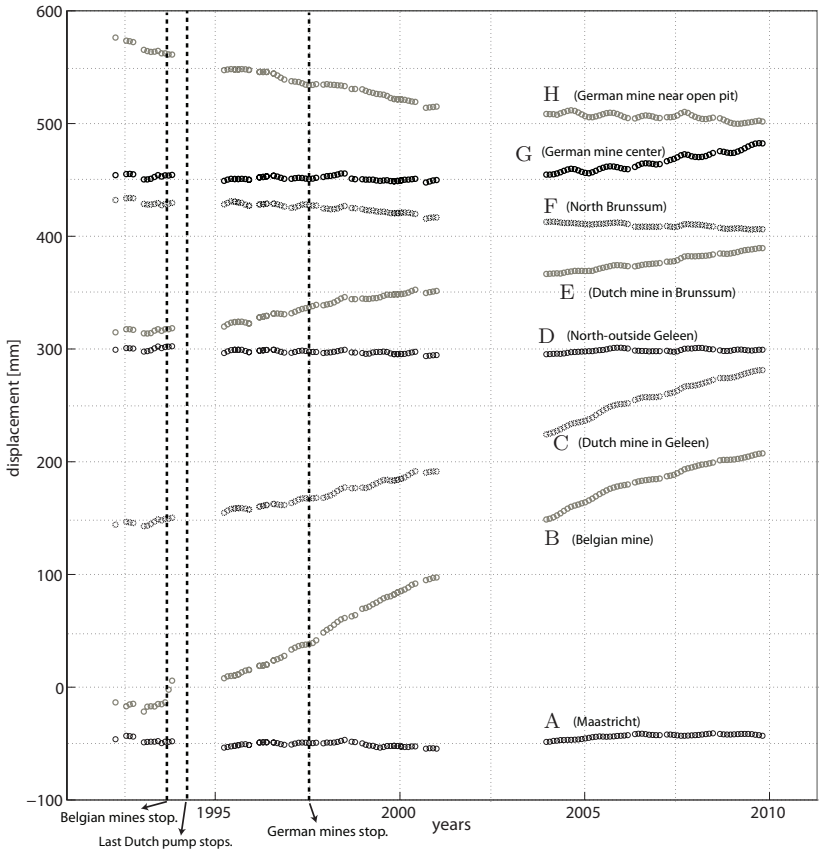

Fig. 6.5. Deformation time series at eight places distributed over the studied area. Their location can be found in fig. 6.2 from the letters A to H. Vertical offsets are added for visualization.

accelerate around 1997-1998. To the east the Dutch coal field, the water extraction that is required in German open pit mines also affects the deformation field producing subsidence.

6.2.3 Groundwater levels compared to estimated displacements

From the results above, it seems that there is a causality between the cessation of pumping and surface uplift. In this section, we investigate this relationship by comparing PS time series with hydraulic heads (groundwater levels) measured at the mine depth.
Figure 6.6 displays the groundwater levels (SoDM, 2007; Rosner, 2011) and corresponding displacements estimated with PSI at three shafts: Julia (JS), and Wilhelmina (WS) in the central basin and Oranje Nassau (ONS) in the northern basin, see location in fig. 6.2. The scale of the groundwater levels is corrected based on the results of a linear regression between surface displacements and water levels. The results show that groundwater levels were constant before 1994. In this year, the pump in Beerenbosch II was dismantled and the mine water started to rise. The small variations of the water level in the Julia shaft,

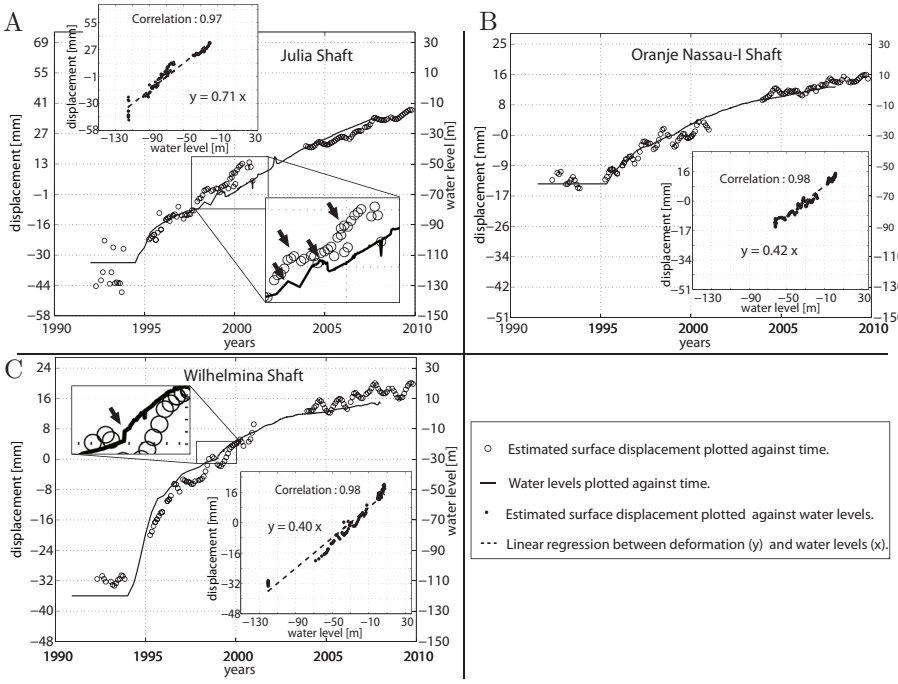

Fig. 6.6. Surface displacements and water levels at A) Julia shaft, B) Oranje Nassau-I Shaft, and C) Wilhelmina shaft. Their locations is indicated in fig. 6.2 with JS, ONS and WS respectively. Water levels are with respect to NAP. The ups and downs of the water level at Julia shaft are due to pumping tests. This is also visible in the Wilhelmina shaft but very slightly showed also as a zoom in.

pointed with arrows in fig. 6.6A, resulted from pumping tests (Heitfeld pers.comm. 2008). This is also visible, albeit very slightly, in the water levels in Wilhelmina, see zoom-in of fig. 6.6C marked also with an arrow. In the Julia shaft, the deformation at the surface seems to react to water level changes with some months delay, as displayed in the zoom-in, fig. 6.6A. Estimating the exact delay is complex as time series could also be affected by a periodic signal related to seasonal changes in surface levels.

In all cases, the groundwater levels show a very high correlation (~ 0.97) with surface deformation, see inset plots in fig. 6.6. However, the correlation does not seem equally high if only the first years of the time series are considered. The only exception is found for the data of the Julia shaft, for dates prior to 1994, see fig. 6.6A, probably due to noise and decreased coherence, leading to uncertainties in the phase ambiguity resolution Hanssen (2001).

Apart from the major signal related to mine water, time series also show periodic variation, clearly visible in figs. 6.6B and C. This was probably caused by a seasonal phenomenon not in connection with deep groundwater, such as the ones explained above.
The inset plots of fig. 6.6 show an almost linear relationship between displacements obtained by PSI and the water levels.

From this, we can estimate the storage coefficient S_{ke} for the central and northern basin. The storage coefficient S_{ke} gives very valuable information on the response of the (fractured) rock to pore pressure changes. This coefficient, usually employed in the analysis of confined aquifers, gives a first approximation of the relationship between water level changes and rock dilatation (Hoffmann, 2003). Groundwater levels in the mines are to directly in contact with the phreatic surface (van Bracht, 2001; Rosner, 2011), i.e. this system can be assumed to be confined. However, saturated conditions, may not be fully met as we deal with an underground mining site with open or collapsed galleries. Nevertheless, as detailed information on the mines is lacking, estimating their storage coefficient can improve our knowledge on the response of the mined ground to pore pressure increase.

When small changes in the effective stress happen, as it is usually the case when they are caused by changes in hydraulic heads (groundwater level), this relationship is linear. Recalling eq. 2.5, storage coefficient is given by,

$$S_{ke} \approx \frac{\Delta z}{\Delta h_{\text{water}}}. \tag{6.1}$$

The storage coefficient S_{ke} states the vertical expansion of the rock Δz for a certain head (groundwater level) change Δh_{water}.

We estimate S_{ke} by assuming that the vertical changes of the disturbed rock are equal to the displacements observed at the surface, (Hoffmann, 2003; Bell et al., 2008). The values are $(0.71 \pm 0.05) \cdot 10^{-3}$, $(0.42 \pm 0.05) \cdot 10^{-3}$ and $(0.40 \pm 0.05) \cdot 10^{-3}$ (dimensionless) for the shafts of Julia, Oranje-Nassau and Wilhelmina mines, respectively.

Groundwater can only be measured at a few places, which are concentrated in the eastern side of the mines. Therefore, there is a serious lack of groundwater records for most of the mines. We propose to solve the lack of information by determining groundwater levels from the estimated storage coefficients and displacements. This is a first order approximation, because we are assuming that the storage coefficients that are estimated at three places in the east side of the mines, are indicative of actual situation in the rest of the concession field. In other words, we hypothesize that storage coefficient anywhere in the mines will remain near the average $0.5 \cdot 10^{-3}$ within the limits of the estimated dispersion of $0.1 \cdot 10^{-3}$. With this approximation ($S_{ke} = 0.5 \pm 0.1 \cdot 10^{-3}$), we determine the groundwater level changes that occurred from 1992 to 2009 from the observed displacements using eq. 2.5. These values are displayed in fig. 6.2, using the same colorbar as for cumulative displacements.

However, we expect major discrepancies between determined and actual groundwater levels at the places where the rock was not disturbed, i.e. where the ground was not mined. The storage coefficient of unmined ground is likely to be below the assumed average $0.5 \cdot 10^{-3}$ outside the dispersion limits and the estimated water level increase we plot in fig. 6.2 is probably underestimated. We expect the storage coefficient to vary from for mined and unmined ground due to the differences in rock porosity. In the production process, as the coal is extracted, the roof layer that separates the rock mass above from the coal seams, breaks and collapses on top of the stowing material (debris), see fig. 6.7. If no stowing has been applied, the roof layer collapses directly on the floor filling the mine opening with rock debris. In this process, the rock porosity of the mined ground increases because changes from being solid to fractured.

Apart from deriving geophysical properties of the mined rock, the comparison between groundwater and surface displacements also reveals that the chronology of events related to groundwater levels appear reflected in PS estimations. In the shafts of Wilhelmina and Julia the groundwater levels started to rise almost simultaneously with the cease of water pumping (1994), and so we observe the corresponding surface deformation. In the shaft of

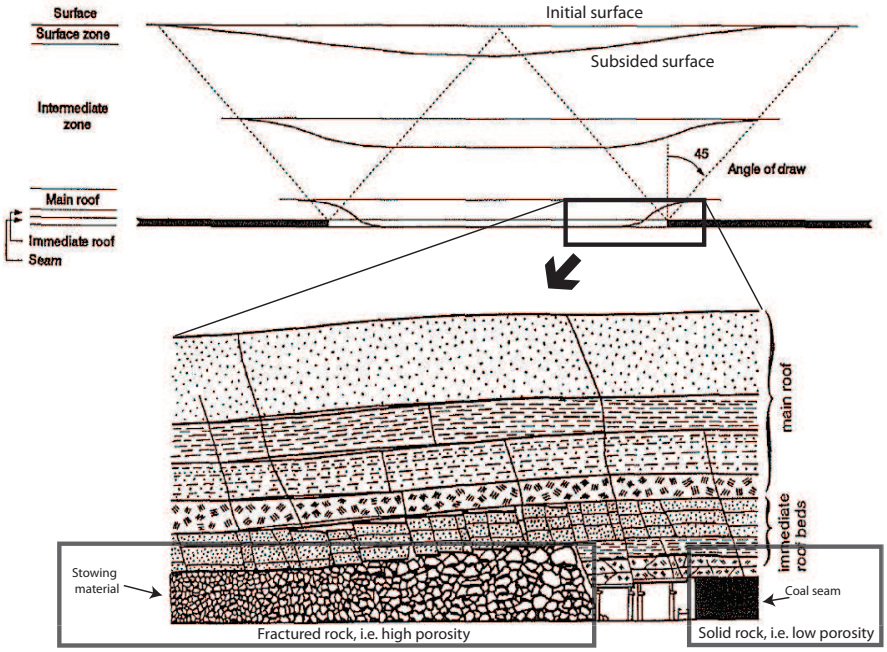

Fig. 6.7. Coal extraction process and its consequence on surface deformation and rock porosity, modified after Kratzsch (1983); Bekendam and Pöttgens (1995).

Oranje-Nassau I, the groundwater levels took a year longer to start rising, and effectively, the surface did not uplift until 1995. In the following, we discuss the evolution of groundwater influx from the observed surface displacements.

6.3 Spatio-temporal evolution of mine water recharge from surface displacements

In section 6.2.3, we demonstrated the high correlation that existed between mine water levels and surface displacements in the Dutch mines. We discussed how groundwater dynamics also reflected in surface displacements. This was particularly visible comparing the groundwater levels in figs. 6.6B and C, for the period from 1994 to 1995. The year 1995 seemed the moment at which the groundwater flowed from the Wilhelmina Shaft to the Oranje Nassau-I Shaft, an event that was also observed in surface displacements. Conversely, we can also use the estimated surface displacements to infer mine water dynamics, even more because groundwater levels can only be measured in a very limited number of places, those ones with physical access.

To study the spatio-temporal evolution of mine water recharge in the Dutch coal field, we draw a profile of yearly cumulative displacements. The results, which are plotted in fig. 6.8, show total displacements from the beginning of the time series (April 1992) to the indicated year. The profile is drawn between Geleen (A) and Beerenbosch II (A') and crosses the

whole Dutch coal field, see location in inset plot of fig. 6.8.

The overall dynamics suggest the mine waters to flow from the southeast to the northwest. From the southern basin, which is where the pump was located (see location in fig. 6.1), the uplift propagates towards the central basin and from here towards the northern basin and the mining area of Geleen, implying the same flowing direction for the groundwater. From the temporal evolution, we observe that the ground appears relatively stable in the whole Dutch coal field for the first years (1992-1993). Then in 1994, when the pump in Beerenbosch II is dismantled, the surface quickly uplifts in the southern basin. Soon after, the groundwater overflows to Wilhelmina, see fig. 6.6. Effectively, the difference in displacements between Wilhelmina Shaft and Beerenbosch II suggest that the overflowing towards the central basin is not immediate after the cease of pumping. This is also confirmed with the time series discussed in section 6.2.3.

The moderate surface deformation signal that we observe in the northern basin before 1996 indicates that the water in this basin is increasing very slowly compared with, e.g., Beerenbosch II. This can be explained if the groundwater in the central basin has not reached an overflowing gallery connecting this with the northern basin. Therefore the conductivity between these two basins is, until this moment, low.

In 1996, we observe an acceleration in the displacements in the central basin that suggests that water is overflowing from the southern basin in this year. High deformation rates are maintained in this basin until 1999, whereafter rates decay with time. On the other hand, the acceleration of the uplift in the mine under Geleen appears in 1998, which probably indicates the time when water overflows from the northern basin.

Comparing the temporal evolution of the basins, we see that surface displacements in the central and southern basins has almost halted at the end of our time series. In the northern basin and the area of Geleen the surface continues to uplift. This suggests that while water level increase in the central and southern basins is now very low, in the northern basins and the Geleen area the water is still rising. This could be related to the natural slope of the carboniferous layers. The depth of this layer increases from east to west see fig. 6.9 (TNO, 1999), which could make the water flow in the observed direction.

Interestingly, the annual cumulative deformations depicted in fig. 6.8 reveal that the confinements of the hydrological units (associated with NE-SW oriented faults) experience very modest uplift rates, less than $\sim$25 mm, or 2–5 times less than the centers of the hydrological units. Geographically, these areas with relatively low uplift rates are situated around Schinnen, between Heerlerheide and Heerlen-north, and around Spekholzerheide. Along the profile of fig. 6.8 this corresponds with distances of 7.5, 16–17, and 22.5 km from the western side of the profile, respectively. It is important to stress that the areas situated directly east and west of these three locations experience the highest relative spatial gradients in uplift velocities, and are therefore probably most susceptible for infrastructural damage at the surface.

6.4 Model of underground volume change

We model the volume change experienced by mining ground due to pore pressure variations with a uniform grid of closely spaced strain sources. Strain sources were defined in section 2.3.2.

Recalling eq.(2.4) , the displacement perpendicular to the surface, d_U, produced by a strain source of finite volume V at the depth D due to a volume change ΔV, is given by (Geertsma

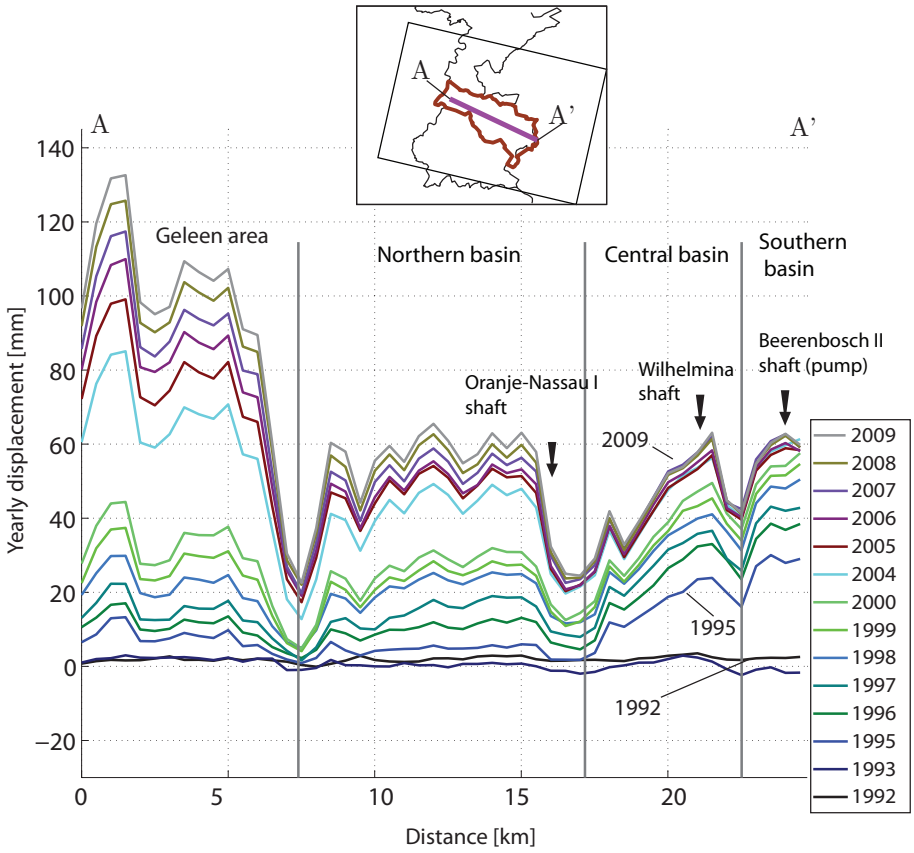

Fig. 6.8. Profile of annual cumulative displacements across the whole Dutch coal field, from Geleen to Beerenbosch II. There are two data gaps in 1994 and from 2001 to 2004, (see text for explanation)

and van Opstal, 1973)

$$d_U(R,0) = -\frac{1}{\pi}(1-\nu)\frac{D}{(R^2+D^2)^{\frac{3}{2}}}\Delta V, \tag{6.2}$$

where R is the radial distance to the nucleus, 0 corresponds to the ground level surface, and ν is Poisson's ratio. Geertsma and van Opstal (1973) related the volume change ΔV to pore pressure changes using the dilatation coefficient d_m

$$d_m = \frac{1}{V}\frac{\Delta V}{\Delta p}, \tag{6.3}$$

which is equivalent to the storage coefficient S_{ke} defined in eq. 6.1.

We model the volume change experienced by mining ground due to pore pressure variations with a uniform grid of closely spaced strain sources. Since water recharge is the cause of

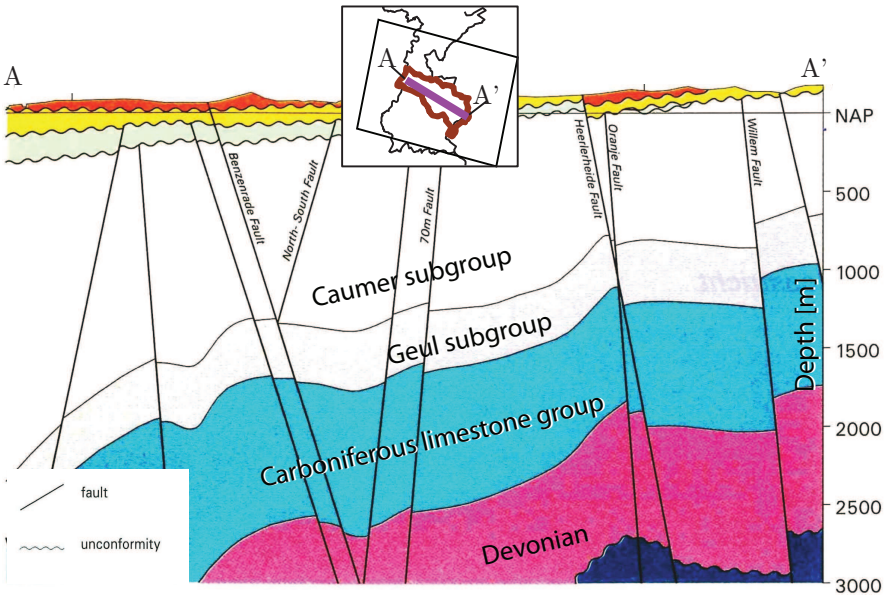

Fig. 6.9. Geological profile of the coal district of South Limburg (TNO, 1999).

the deformation, the strain source depth is taken to be at the water levels with respect to surface, −250 m.

To prevent a solution that is physically impossible, we constrain the sources spatially. We assume that the strain sources form disk-shaped hydrological units (Geertsma, 1973; Pöttgens, 1985). To estimate the radius of the disks, we employ the pressure distribution found for water extraction in reservoirs (Segall et al., 1994). In this case, there exist an exponential decline of the pressure p with distance r with respect to a drainage point:

$$p(r,t) = p_0(t)e^{-(r/r_c)^4}, \tag{6.4}$$

where t is time, p_0 is the maximum pressure change at $r = 0$, and r_c is the characteristic radius of the reservoir, which defines the main area of influence of the pumping.

We assume that the same distribution is valid also for the inverse situation, when pumping stops. The pressure increase is then maximum at the place where the pump was located and decaying exponentially with distance as given by eq. (6.4).
We can also find the distribution of volume change with eqs. (6.3) and (6.4):

$$\Delta V(r) = V d_m \Delta p(r,t) = V d_m \left(p_0(t_2) - p_0(t_1)\right) e^{-(r/r_c)^4} = \Delta V_0 e^{-(r/r_c)^4}, \tag{6.5}$$

where ΔV_0 is the maximum volume change. Essentially, this is equivalent to model the hydrological units as disk-shaped reservoirs.

Since the coal field has different overflowing galleries connecting the water basins, we assume that the distribution of volume change given in eq. (6.5) can happen at different places in the coal field. Therefore, we also estimate the number of disk-shaped reservoirs needed to

modeled the coal field.

6.4.1 Modeled rock dilatation

To model volume increase of the rocks of the Dutch mines, we use eq. (2.4) in combination with eq. (6.5). For the Poisson's ratio we employ the value $\nu = 0.25$ suggested by Bekendam and Pöttgens (1995).
To estimate the number of disk-shaped reservoirs that are required, we first search for the location of local maxima in the deformation field. For the Dutch mines, we find ten local maxima whose locations are displayed in fig. 6.10 as black circles. We therefore model the volume increase experienced by the mined ground as it was equivalent to ten disk-shaped aquifers with increasing pore pressure.

The disks size and location are estimated from the data regardless of the real location of previously active pumps. This means that, although the model fairly represents the volume increase experienced by the mined ground, the disk-shaped units do not necessarily reflect the actual geophysical situation, in the sense that their estimated size and number may not correspond to real circumstances. The unknowns to be estimated are the maximum volume change ΔV_0 and the characteristic radius r_c, per local maxima, yielding 20 unknowns in total. Since eq. (6.5) is not linear a search in the parameter space of r_c is performed.
The estimated volume increase is displayed in fig. 6.10A and the residuals (observed minus modeled displacements) in fig. 6.10B. From the residuals we observe a fair fit of the model for most of the areas with the exception of western lower corner of the Dutch concessions.

The predicted vertical dilatation $\Delta\hat{z}$ is calculated for a uniform grid of volume elements with a posting of $S = 150$ m, based on the ten initial disks, using the estimated volume increase $\Delta\hat{V}$, assuming this is only in the vertical direction:

$$\Delta\hat{z} = \frac{\Delta\hat{V}}{S^2}. \tag{6.6}$$

The estimations show the places with greatest volume change to be concentrated in three different areas revealing the mines which may have the highest storage coefficients.

As discussed in section 6.3, the areas with relatively low vertical dilatation (~ 25 mm) were probably not affected by the coal extraction process, (due to faults) and most likely show the natural expansion of undisturbed rock.
Maximum values of volume increase are found in the western mines, corresponding to the area of Geleen. In this area the vertical dilatation reaches around 135 mm. This can be explained either by a higher dilatation coefficient or by a greater increase in pressure, caused by the increaseder influx of water in this part of the region. Since there is a temporal pattern in the rising of water levels in the different hydrological units, it is more likely that the observed higher uplift rates in the west, for the latest periods, are caused by an increased water flux in the region at those times.

6.5 Summary and conclusions

Surface displacements observed by satellite radar interferometry show unambiguously that most of the abandoned coal fields in the southern Netherlands, Germany and Belgium were rising during the period 1992-2009. The high point density and long observational period enables us to identify and study the deformation behavior, mostly related to water rebound. Displacements of up to +220 mm in 18 years are measured for the mines in

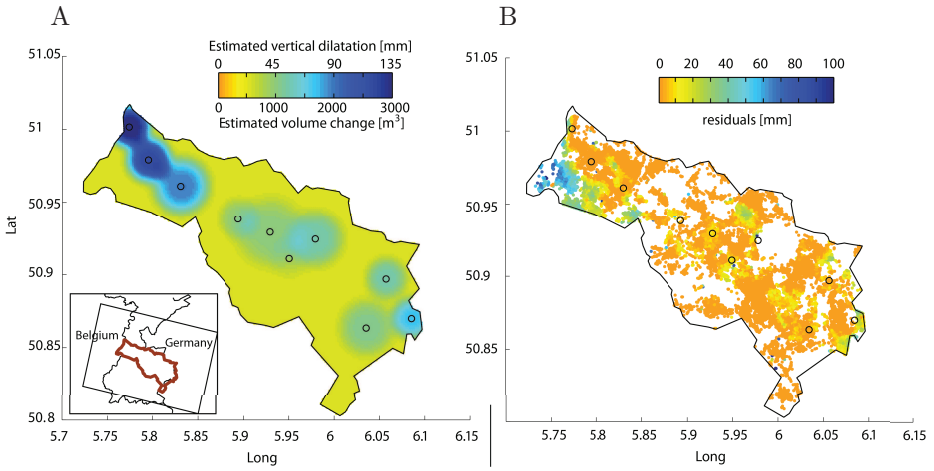

Fig. 6.10. A) Modeled volume caused by pore pressure increase. Estimated vertical dilatation is also displayed and calculated assuming the dilatation is only vertical. B) Residuals obtained after subtracting measured to modeled deformation. The black circles show the location of a local maxima used in during modeling.

Belgium. In the Netherlands a maximum of +125 mm is found in the Dutch western mining area, near Geleen, over the same period. The uplift signal is highly variable in space and time. Spatially, the uplift is strictly confined to areas bounded by faults, both the major NW-SE trending faults parallel to the Roer-Valley Graben, as well as faults orthogonal to this system. Temporally, the uplift rate is initially (1992–1995) greatest in the south-eastern mining area, but around 1999–2004 the process progresses towards the north-western mining areas. Comparing observed surface displacements with mine water levels at three old shafts in the east of the mining area shows that there is a strong correlation. Assuming comparable situations in the entire region, we estimate an average storage coefficient of $0.5 \pm 0.1 \cdot 10^{-3}$, implying that 10 m water level increase results in 0.5 cm of surface uplift. Under these assumptions, we estimated that for the area of Geleen, where the groundwater cannot be directly measured, the groundwater level has risen around 250 ± 50 m from 1992 to 2009. The time series in Geleen suggest that the groundwater is currently still rising.

The temporal progression of the surface uplift suggests complex sub-surface water dynamics. In 1995 the rising water in the southern basin reached the overflowing gallery, connecting it to the central basin, and in 1996 the water reached the northern basin. The PSI displacements show that the water from the northern basin started to overflow towards the Geleen-basin in 1998, when we observe an acceleration in the motion.

A simple model based on a distribution of strain sources and an inverse exponential pressure decline allows for the estimation of volume change based on the surface measures. Pressure and volume changes are indicative for an increased influx of water in a confined basin.

The influence of tectonic faults in the displacement field is clearly visible in the deformation data due to the strong gradients orthogonal to the faults. Apparently, water does not seem to flow freely across a fault. This could be due to the decrease in permeability of the fault zone, perhaps caused by a grinding effect associated with motion along the

fault. Alternatively, faults might separate hydrological units with significantly different properties, e.g., aquifers may be found at different depths at both side of a fault. The strong gradients in uplift rates cause differential motion on relatively short (0.1-1 km) spatial scales. This may inflict strain on buildings and infrastructure.

Although risk assessment is beyond the scope of this study it is worth notting that the results of our analysis identify several areas which seem prone to infrastructure damage.

Chapter 7

Conclusions and Recommendations

The general objectives of this dissertation were formulated in chapter 1 as the following research question:

How to improve PSI for an optimal study of fault-related motion and what do we learn from the application of the improved technique to the southern Netherlands concerning the Roer Valley Graben and the influence of the coal mine industry on surface deformation?

This dissertation discussed the use of Persistent Scatterer Interferometry (PSI) to study fault-related displacements. First efforts were dedicated to improve current PSI algorithms. The major contribution of this study to PSI techniques is a novel method for phase unwrapping.
The new technique was then applied to the southern Netherlands where I focused on studying tectonic motion caused by the Roer Valley Rift System and ground displacements due to mine abandonment. Concerning the Roer Valley Rift system, I detect a deformation signal associated with geological faults. However, I do not find any significant evidence for this signal to be related to tectonics. I interpret the observed deformation to be mostly produced by pore pressure changes in aquifers due to groundwater flow. Pore pressure changes seem to be also the cause of surface deformation in the abandoned mines of the southern Netherlands. PSI results show very high correlation between mine water level and surface displacements.

This chapter answers the main research question by discussing the contributions of this research. At the end of the chapter, some recommendations are given for future work.

7.1 Scientific contribution

7.1.1 PSI optimization

How to optimize the PSI technique to study fault-related displacements?

The optimization of PSI techniques was motivated by the spatial characteristics of the signal that we wished to observe. Fault related displacements were spatially correlated but could change across faults. Furthermore, I also searched to reduce the noise affecting the PS to enable significant estimation of small deformation signals ($\sim$1 mm/yr), such as the expected Neotectonic motion in the Netherlands.

In the process of PSI optimization, see section 4.2, I first focused on phase unwrapping. The method provided in this thesis first estimates correlated information such as the pdf of displacements. Secondly, it uses this information through Bayesian theory to constrain unwrapped solutions. I also investigated how to estimate the noise variance of each PS to weight observations (wrapped phases), and I provided a solution to estimate it spatially. This method is based on the assumption that decorrelation could be spatially correlated. I showed empirically the added value of the approach, which included both Bayesian unwrapping and spatial estimation of noise variance, to observe an increase in the number of PS that were accepted after consistency checks.

This dissertation also studied how to the optimize of the work flow of DePSI, the algorithm used as reference, to reduce the influence of atmospheric noise and to increase the density of PS that were consistently unwrapped, see section 4.3. I proposed to create a dense network of PS that were reliably unwrapped in contrast to the sparse network used in the reference technique. Since the spatially correlated noise term is estimated through spatial interpolation, the estimation improves with a denser network of reliable observations. Effectively, the results showed an increase in the number of PS that passed consistency checks increased after removing the spatially correlated noise with the proposed (dense network) method.

The dense network approach is also used to unwrap PS that were initially rejected because their unwrapping solutions are inconsistent. For this case, I also found an increase in the final number of PS that survived consistency checks, which can be explained due to a decrease in phase variability caused by shorter distances between PS (arc lengths).

To conclude the optimization of PSI for deformation monitoring, I developed an algorithm to join displacement time series covering non overlapping time spans, section 4.4.1. The method combines the time series by estimating a vertical offset due to the deformation occurring between the two master images by assuming that the same geometric model can be applied for both time series. I tested the method in the mines of Limburg and compared the results with groundwater levels variations, which are the main cause of displacements. I found a good agreement between the two, with a correlation of around 0.97. Since the proposed approach uses BLUE, the model can be tested and the precision of the estimated vertical offsets can be determined.

7.1.2 Surface motion in the Roer Valley Rift System

What do we learn about the Roer valley Rift System from the displacements measured by PSI?

PSI reveals the area of Roer Valley Rift System to be affected by a signal that seems to be mostly related to groundwater flow fluctuations rather than to faulting. The results show the graben to uplift with respect to adjacent horsts during large part of the studied period, which is opposite to predicted by tectonics. In this area, I also observe strong surface displacements caused by water extraction required in the mining industry and mine water rebound after the cease of water pumping. Thus, the deformation signal that is observed in the Roer Valley Rift System appears to be the consequence of pore pressure variations in aquifers; variations that are mainly caused by water pumping and/or aquifer recharge.

Based on that, it seems that an important part of the differences between slip rates estimated in geological and short time scales is caused by underground water variations. In fact, surface deformation produced by underground water variations could have an apparent behavior similar to tectonics. For example, if water is pumped within the graben and

aquifers are discontinuous across the faults, the graben would appear to subside relative to adjacent blocks.

With the high observation frequency (usually once every 35 days) and a long time span of about 18 yr provided by InSAR, the temporal behavior of the deformation signal in the Roer Valley Rift System was studied with unprecedented detail. The analysis reveals a signal with large temporal variability. If this signal is not studied over a long time span and is not sampled at a sufficient frequency its analysis can be aliased. For the period 1992-2001, the Roer Valley Graben appears to uplift relative to adjacent horsts with the rates values in the order of +1 mm/yr. However, for the time span 2004-2010, the signal changed sign and the Roer Valley Graben subsided with respect to adjacent horsts at an average rate of -1 mm/yr. I showed that the signal found for this last period was largely related to the cease of water pumping in nearby mines. The time span of 18 yr contributed to a better understanding of the origin of the deformation. The fact that the graben was uplifting for the initial periods already suggested that the nature of the observed signal could not be tectonics. The coverage of the radar images (100×100 km) contributed to identifying mine water pumping as the most probable cause of deformation in this area.

7.1.3 Surface motion in the abandoned mines of the southern Netherlands

What do we learn about the influence of coal mine industry in surface deformation in the southern Netherlands from the displacements measured by PSI?

The application of PSI to the coal fields of the southern Netherlands show the abandoned mines to be uplifting. The high correlation found between deformation time series and mine water level fluctuations suggests that the major contribution to surface uplift in this area is pore pressure increase caused by rising mine waters. From this high correlation, I inferred underground water dynamics from time series estimations. The results showed the water to flow in E-W direction. More precisely, in 1994, when the last pump in the Dutch coal field stopped operating, groundwater levels started to rise and the ground in the above area began to uplift. This motion propagated from east to west, towards the mines that were in hydrological connection with the pump. I found an acceleration in the uplift in western Dutch mines in 1998, which suggested the moment when the water overflowed to this areas.

The signal observed in the mining districts is area dependent. The total values range from 20 to 140 mm for the studied period from April 1992 to November 2009. Local maxima are found in the mined areas, i.e. at the surface above fractured rocks. The variability of cumulative deformation seems to be caused by differences in rock porosity, which increased during the coal extraction as the rock was fractured or by a greater increase in pressure, caused by the rising influx of water in this part of the region. The areas that were not disturbed during coal production, due to faults, experienced the most moderate uplift (∼20 mm). The signal experienced the largest gradients in the direction normal to faults. Displacements bounded by faults could be caused by an impermeable fault acting as a barrier or because the medium in which the water flow is not continuous across the fault.

The added value of PSI when applied to the abandoned coal fields is evident. PSI allows us monitoring surface displacements and to study the temporal evolution of the mines with very high detail. Thanks to the high density of observations we are able to highlight the areas that are sensitive to deform under pore pressure fluctuations and to observe the influence of the faults on surface deformation. For example, studying the mines in Limburg, I observed how tectonic faults bounded the deformation, producing gradients of ∼5 cm/km for the time span of 18 yrs.

From the detailed information that PSI provided on surface displacements, it can be concluded that this technique improves the monitoring of coal mine induced displacements and that PSI can help to mitigate and plan hazards situations derived from large gradients in the deformation field.

7.2 Recommendations

7.2.1 PSI

As discussed above, in the optimization of PSI algorithms I developed a method for phase unwrapping that extracts and uses spatially correlated information. Although I proved the value of this approach, the method depends on PS density. The number of detected PS is usually fair for most of the Dutch territory due to its high urban density. For other areas, for example places with dense vegetation or seasonal snow cover, detecting coherent scatterers is not trivial. Using pixels that are coherent during part of the studied period can help to overcome this limitation. New trends in time series InSAR now aim at extracting information not only from PS but also distributed scatterers see e.g. Hooper (2008),Ferretti et al. (2011) and Goel and Adam (2011). These new methods combine the merits of PSI with other time series techniques, namely small baselines (SB), to improve the observation density.

The estimation of atmospheric artifacts and other spatially correlated noise such as orbital errors is also an area that can be further improved. I approached the problem in a classical manner, i.e., employing the information contained in the radar images, namely unwrapped phases and filtering them in time. In this research, I had long time series and well sampled in time, so the estimates of the spatially correlated noise were in principle precise at least for most of the interferograms. For situations when the measurement frequency is low or very irregular or when the deformation signal changes fast in time, the method used in PSI for spatially correlated noise estimations needs to be improved. For example, atmospheric signals can be estimated by combining different sources available information, such as atmosphere estimates obtained from PSI, GPS and weather models. Furthermore, the differences in vertical displacements estimated from PSI and other geodetic tools (e.g., GPS and leveling) can also be employed to estimate spatially correlated noise. All these techniques have limitations but the combination of all can definitely help mitigating atmosphere and orbital errors. Merging different techniques is however a complex task. The fact that InSAR provides with double differences requires that the same spatial and temporal reference should be available for all different observations, something that is not always possible. In this case, assumptions such as a valid interpolation in space and time may be needed.

7.2.2 The Roer Valley Rift System

Concerning the Roer Valley Rift System, and although a very plausible explanation was given for the displacements based on relationship with underground water levels, the proof for the source of the pore pressure variations still not fully satisfying. Part of the signal is probably produced by the mining industry, but other sources, such as natural changes of the aquifers or regional water use, could have also existed.

The estimation of Neotectonic motion at short time scales remains a complicated task, as surface displacements are very likely to be dominated by displacement signals other than tectonics. I observed that the major contributor seemed to be related to pore pressure changes. The estimations suggested at least two sources of pore pressure changes to af-

fect the Roer Valley Graben: water pumping in the lignite mines in Germany and water rebound in the abandoned coal mines. The estimation of slip rates requires to model and remove these signals. The results of my study suggest that long time series, high density of observations and large coverage are needed to estimate such processes, as pore pressure variations appear to affect for decades large areas and can vary quickly in space in the presence of tectonic faults. Measurements of groundwater levels at different depths, not only at shallow aquifers, are also needed to model displacements from pore pressure changes, as we saw that water flow at a depth deeper than 200 m resulted in surface deformation.

7.2.3 Coal mine induced displacements in the southern Netherlands

The monitoring of land deformation of the Dutch coal mines can be further improved with the combination of PSI results with other geodetic techniques. Leveling or GPS can be used to constrain large scale patterns, or to provide observations where PSI does not detect stable scatterers. Monitoring fast processes derived from mine abandonment, such as sinkhole formation, requires satellites with short visiting time. For example, TerraSAR-X with a revisit time of 11 days, can contribute to detect fast deforming areas, or the future satellite Sentinel-1, which will be launch in 2013, will be able to provide with an image every 6 days, by combining ascending and descending modes.

Detecting and monitoring local deformation phenomena, such as building collapse, may need an optimized strategy different than the one suggested in this thesis. The assumption of spatially correlated displacements may not be valid for this case. Developing a method aiming at detecting low-noise scatterers with anomalous deformation behavior will, in principle, aid the monitoring of these situations.

Appendix A

Used software tools

The interferograms of this thesis were generated using Doris (Kampes et al., 2003). The steps we performed to create the interferograms are briefly described in the following bullet points; Doris terminology is indicated within brackets (Kampes et al., 2011):

- Read the header of the SLC master image, and extract relevant parameters (M_READFILES).
- Retrieve the precise Delft orbital data records with the getorb package (M_ORBITS). Satellite precise orbits are provided by the Delft University of Technology, (Scharroo and Visser, 1998), and by ESA (European Space Agency) .
- Extract and crop the data from the master SLC (M_CROP).
- Oversample of the master crop (M_OVS).
- Read the header of the SLC slave image, and extract relevant parameters (S_READFILES).
- Retrieve the precise Delft orbital data records with the getorb package (S_ORBITS).
- Extract and crop the data from the slave SLC (S_CROP).
- Oversample of the slave crop (S_OVS).
- Compute an initial translation between master and slave from precise orbits (COARSEORB).
- Improves the initial translation between master and slave using the correlation between the amplitude of the master and slave (COARSECORR).
- Compute translation vectors using the results of COARSECORR over the total image on sub-pixel level (FINE).
- Estimate a mapping function from the results of FINE (COREGPM).
- Resample the slave image according to mapping function of COREGPM (RESAMPLE).
- Compute the (complex) interferogram (INTERFERO).
- Compute the reference phase of the ellipsoid to be subtracted from the interferogram (COMPREFPHA).
- Subtract the reference phase of the ellipsoid from the interferogram (SUBTRREFPHA).
- Compute the reference phase of a DEM to be subtracted from the interferogram (COMPREFDEM). We used the DEM provided by the SRTM mission (Farr et al., 2007).
- Subtract the reference phase of the DEM from the interferogram (SUBTRREFDEM).

Interferogram stacks were produced using bash scripts, mainly developed by P. Marinkovic.

The main contributors to the original DePSI algorithm were F. van Leijen, P. Marinkovic and G. Ketelaar. However, many other people in the radar group of Geoscience and Remote Sensing Department of TUDelft did contribute as well.

The new algorithm, see chapter 4 was implemented by the author of this thesis using Matlab and then coupled to DePSI. The main functions of the combined software are briefly described next with function name indicated in brackets:

- Read the parameter input by the user (ps_readinput_parameters).
- Selection of PS (ps_selection).
- Spatial estimation of the variance (estima_spa_std).
- Build the first order network (ps_network). Temporal unwrapping and network adjustment are also performed with this function.
- Build the second order network (ps_densification_psc). Temporal unwrapping and test (Densification of the first order network with PS whose unwrapping solutions pass statistical tests unwrapped) are also performed within this function.
- Temporal filtering of first and second order network unwrapped phases (psc2_filtering).
- Estimation of atmosphere and orbital errors using first and second order networks (psc2_atmo_kriging).
- Perform the final densification step with PS that were rejected from first and second order networks (ps_densification).
- Estimate the desired parameters from unwrapped (integrated) phases (ps_final_estimation).

Appendix B

Used SAR data

The following tables give a summary of the data sets used in this research for the two areas of interest.

For the Roer Valley Rift system area, see chapter 5, we used the data described in tables B.1 and B.2.

To study the mines of south Limburg, see chapter 6 we employed the data described in tables B.2 and B.3. These data sets corresponds to the same track as for the Roer Valley rift system, but shifted 17 frames.

Table B.1. ERS1/2 data over the Roer Valley Rift system area (track 380 and frame 2567).The columns indicate orbit number, date, of acquisition, perpendicular baseline $B_\perp$ w.r.t. master image (first row), and Doppler centroid difference w.r.t. master image Δf_{DC}.

orbit Nr	date	$B_\perp$	Δf_{DC}	orbit Nr	date	$B_\perp$	Δf_{DC}
17268	**09-AUG-1998**	**0**	**0**	**17268**	**09-AUG-1998**	**0**	**0**
01236	16-JUL-1995	-87.1	-25	16266	31-MAY-1998	384.6	-44
01737	20-AUG-1995	127.7	33	16767	05-JUL-1998	-566.7	-103
02739	29-OCT-1995	854	34	17769	13-SEP-1998	-137.4	-14
03240	03-DEC-1995	-214.3	23	18270	18-OCT-1998	-349.7	-18
04032	23-APR-1992	-61.2	-256	19272	27-DEC-1998	-333.5	-42
04743	17-MAR-1996	399.4	64	19406	01-APR-1995	-638.5	-237
05244	21-APR-1996	486.5	-3	19773	31-JAN-1999	-34.6	-65
05535	06-AUG-1992	-69.7	-250	19907	06-MAY-1995	-665.4	-278
05745	26-MAY-1996	-109.3	17	20274	07-MAR-1999	-641.6	-52
06036	10-SEP-1992	440.1	-244	20408	10-JUN-1995	-126.5	-290
06537	15-OCT-1992	415.6	-244	20775	11-APR-1999	496.2	-32
06747	04-AUG-1996	277.1	29	20909	15-JUL-1995	-112.2	-275
07248	08-SEP-1996	-280.7	13	21276	16-MAY-1999	327.3	-58
07749	13-OCT-1996	-39.7	0	21410	19-AUG-1995	207.7	-255
08040	28-JAN-1993	-244.3	-225	21777	20-JUN-1999	113	-48
08250	17-NOV-1996	1245.5	19	21911	23-SEP-1995	-158.2	-255
08541	04-MAR-1993	121.3	-207	22278	25-JUL-1999	615	-30
09042	08-APR-1993	819.9	-275	22779	29-AUG-1999	-926.4	-58
09252	26-JAN-1997	267.8	-12	22913	02-DEC-1995	-165.9	-231
09543	13-MAY-1993	-441.5	-242	23280	03-OCT-1999	160.6	17
09753	02-MAR-1997	27.1	-36	23781	07-NOV-1999	-77.3	34
10044	17-JUN-1993	-359.8	-258	24282	12-DEC-1999	-24.9	15
10254	06-APR-1997	486.1	-51	24416	16-MAR-1996	386.3	-279
10545	22-JUL-1993	-164.3	-252	24783	16-JAN-2000	-412.5	-22
10755	11-MAY-1997	-51.5	-28	24917	20-APR-1996	558.3	-257
11046	26-AUG-1993	-562	-246	25284	20-FEB-2000	-643.9	238
11256	15-JUN-1997	-69.4	-66	25418	25-MAY-1996	2.5	-259
11547	30-SEP-1993	231.1	-244	25785	26-MAR-2000	713	298
11757	20-JUL-1997	-35.8	-32	26286	30-APR-2000	246.7	243
12048	04-NOV-1993	681.5	-237	26420	03-AUG-1996	387.4	-243
12258	24-AUG-1997	464.7	44	26787	04-JUN-2000	-186.8	420
12759	28-SEP-1997	-19.4	4	28290	17-SEP-2000	287.4	318
13761	07-DEC-1997	298.8	-10	28791	22-OCT-2000	-182.1	311
14262	11-JAN-1998	-186.6	-37	29292	26-NOV-2000	635.4	-41
14763	15-FEB-1998	97.2	-29	29793	31-DEC-2000	-530	-296
15264	22-MAR-1998	89.3	13	43955	11-DEC-1999	-209.9	-268
15765	26-APR-1998	345.5	-23	44456	15-JAN-2000	-524.4	-267

Table B.2. Envisat data over the Roer Valley Rift system area (track 380 and frame 2567). Same notation as before.

orbit Nr	date	$B_\perp$	Δf_{DC}	orbit Nr	date	$B_\perp$	Δf_{DC}
25985	18-FEB-2007	0	0	25985	18-FEB-2007	0	0
09452	21-DEC-2003	-129.5	23	25484	14-JAN-2007	701	3
09953	25-JAN-2004	429.2	23	26486	25-MAR-2007	646.4	-12
10454	29-FEB-2004	-406.2	22	26987	29-APR-2007	-145	-4
10955	04-APR-2004	893.7	18	27488	03-JUN-2007	52.2	0
11456	09-MAY-2004	-626.1	19	27989	08-JUL-2007	22.7	0
11957	13-JUN-2004	147.2	37	28490	12-AUG-2007	-16.1	-5
12458	18-JUL-2004	182.7	17	28991	16-SEP-2007	562.6	-6
12959	22-AUG-2004	40.9	21	29492	21-OCT-2007	-93.4	3
13460	26-SEP-2004	-781.9	24	29993	25-NOV-2007	262.9	3
13961	31-OCT-2004	249.9	25	30494	30-DEC-2007	-285.5	3
14462	05-DEC-2004	291.6	26	30995	03-FEB-2008	207.5	-6
14963	09-JAN-2005	-872.6	19	31496	09-MAR-2008	-92.8	-1
15464	13-FEB-2005	-247.9	23	31997	13-APR-2008	452.4	6
15965	20-MAR-2005	-734.9	23	32498	18-MAY-2008	-30.1	9
16466	24-APR-2005	377.5	25	32999	22-JUN-2008	230.3	1
16967	29-MAY-2005	28.9	22	34001	31-AUG-2008	278	-9
17468	03-JUL-2005	629.9	29	34502	05-OCT-2008	-30.6	-4
17969	07-AUG-2005	-40.6	18	35003	09-NOV-2008	133.1	-10
18470	11-SEP-2005	-105.1	21	35504	14-DEC-2008	-236.7	-2
18971	16-OCT-2005	-45.7	-8	36005	18-JAN-2009	289.6	3
19472	20-NOV-2005	417.8	-5	36506	22-FEB-2009	36.5	0
19973	25-DEC-2005	434.5	3	37007	29-MAR-2009	776.4	-15
20474	29-JAN-2006	-773.6	-15	37508	03-MAY-2009	-83	-5
20975	05-MAR-2006	205.1	-4	38009	07-JUN-2009	190.4	3
21977	14-MAY-2006	-56.6	-6	38510	12-JUL-2009	139.2	14
22478	18-JUN-2006	119.9	0	39011	16-AUG-2009	77.6	-8
22979	23-JUL-2006	733	-3	39512	20-SEP-2009	629.5	-7
23480	27-AUG-2006	668	-1	40013	25-OCT-2009	16.6	-14
23981	01-OCT-2006	-666.8	-1				
24482	05-NOV-2006	-539.3	-3				
24983	10-DEC-2006	367.2	2				

Table B.2. ERS1/2 data over the mining area of the southern Netherlands (track 380 and frame 2584). Same notation as before.

orbit Nr	date	$B_\perp$	Δf_{DC}	orbit Nr	date	$B_\perp$	Δf_{DC}
17268	**09-AUG-1998**	**0**	**0**	**17268**	**09-AUG-1998**	**0**	**0**
01236	16-JUL-1995	-93	-24	16767	05-JUL-1998	-574.7	-109
01737	20-AUG-1995	121.2	34	17769	13-SEP-1998	-145.8	-10
02739	29-OCT-1995	859.1	30	18270	18-OCT-1998	-366.8	-19
03240	03-DEC-1995	-222.3	27	19272	27-DEC-1998	-342.4	-46
04032	23-APR-1992	-54.6	-254	19406	01-APR-1995	-648.1	-238
04743	17-MAR-1996	389.1	71	19773	31-JAN-1999	-34	-62
05244	21-APR-1996	491.4	-13	19907	06-MAY-1995	-679.5	-285
05535	06-AUG-1992	-70.7	-252	20274	07-MAR-1999	-653.2	-53
05745	26-MAY-1996	-116	4	20408	10-JUN-1995	-129.1	-297
06036	10-SEP-1992	445.7	-244	20775	11-APR-1999	502.4	-32
06537	15-OCT-1992	410.4	-245	20909	15-JUL-1995	-118.3	-278
06747	04-AUG-1996	268.8	30	21276	16-MAY-1999	326.1	-58
07248	08-SEP-1996	-288.5	10	21410	19-AUG-1995	202.9	-259
07749	13-OCT-1996	-42.5	-2	21777	20-JUN-1999	102.4	-51
08040	28-JAN-1993	-254.2	-226	21911	23-SEP-1995	-164	-261
08250	17-NOV-1996	1253.7	22	22278	25-JUL-1999	616.7	-32
08541	04-MAR-1993	109.8	-204	22779	29-AUG-1999	-942.9	-61
09042	08-APR-1993	815.6	-276	22913	02-DEC-1995	-172.7	-231
09252	26-JAN-1997	260.5	-12	23280	03-OCT-1999	161.1	23
09543	13-MAY-1993	-446.2	-247	23781	07-NOV-1999	-86.7	27
09753	02-MAR-1997	22.9	-33	24282	12-DEC-1999	-25.6	18
10044	17-JUN-1993	-361.4	-261	24416	16-MAR-1996	379.2	-278
10254	06-APR-1997	484	-50	24783	16-JAN-2000	-427.4	-18
10545	22-JUL-1993	-166.6	-250	24917	20-APR-1996	565.3	-268
10755	11-MAY-1997	-54.9	-28	25284	20-FEB-2000	-657.2	232
11046	26-AUG-1993	-576.3	-243	25418	25-MAY-1996	-36.3	-261
11256	15-JUN-1997	-73.3	-69	25785	26-MAR-2000	717.4	329
11547	30-SEP-1993	226	-241	26286	30-APR-2000	236.9	278
11757	20-JUL-1997	-29.5	-32	26420	03-AUG-1996	381.9	-247
12048	04-NOV-1993	676.6	-238	26787	04-JUN-2000	-182	432
12258	24-AUG-1997	461.8	49	28290	17-SEP-2000	286.6	338
12759	28-SEP-1997	-21.3	3	28791	22-OCT-2000	-194.8	295
13761	07-DEC-1997	286.6	-5	29292	26-NOV-2000	630.2	-8
14262	11-JAN-1998	-195.1	-35	29793	31-DEC-2000	-543.6	-311
14763	15-FEB-1998	84	-27	43454	06-NOV-1999	90.3	-244
15264	22-MAR-1998	84.4	18	43955	11-DEC-1999	-214.9	-270
15765	26-APR-1998	341.5	-25	44456	15-JAN-2000	-541.8	-265
16266	31-MAY-1998	375.3	-45				

Table B.3. Envisat data over the mining area of the southern Netherlands (track 380 and frame 2584). Same notation as before.

orbit Nr	date	$B_\perp$	Δf_{DC}	orbit Nr	date	$B_\perp$	Δf_{DC}
25985	18-FEB-2007	0	0	25985	18-FEB-2007	0	0
09452	21-DEC-2003	-132	26	24983	10-DEC-2006	360.6	-1
09953	25-JAN-2004	418.1	27	25484	14-JAN-2007	690	3
10454	29-FEB-2004	-413.7	31	26486	25-MAR-2007	636	-14
10955	04-APR-2004	891.7	18	26987	29-APR-2007	-143.6	-7
11456	09-MAY-2004	-635.3	29	27488	03-JUN-2007	50.5	3
11957	13-JUN-2004	150.7	43	27989	08-JUL-2007	-23.3	0
12458	18-JUL-2004	182.3	20	28490	12-AUG-2007	-20.6	-1
12959	22-AUG-2004	39.4	25	28991	16-SEP-2007	550.6	-6
13460	26-SEP-2004	-778.3	31	29492	21-OCT-2007	-96.8	0
13961	31-OCT-2004	254.8	27	29993	25-NOV-2007	253.6	5
14462	05-DEC-2004	286.1	29	30494	30-DEC-2007	-287.6	-1
14963	09-JAN-2005	-871.7	24	30995	03-FEB-2008	199.4	-3
15464	13-FEB-2005	-257.7	27	31496	09-MAR-2008	-98.1	-4
15965	20-MAR-2005	-730	26	31997	13-APR-2008	441.5	3
16466	24-APR-2005	386.8	29	32498	18-MAY-2008	-31.6	2
16967	29-MAY-2005	26.4	29	32999	22-JUN-2008	226.7	-2
17468	03-JUL-2005	635.9	28	34001	31-AUG-2008	267	-10
17969	07-AUG-2005	-47.5	22	34502	05-OCT-2008	-31.9	-6
18470	11-SEP-2005	-93.3	29	35003	09-NOV-2008	125.4	-11
18971	16-OCT-2005	-42.6	-8	35504	14-DEC-2008	-237.6	-3
19472	20-NOV-2005	412.7	-5	36005	18-JAN-2009	282.4	0
19973	25-DEC-2005	420.2	2	36506	22-FEB-2009	36.3	0
20474	29-JAN-2006	-781.2	-8	37007	29-MAR-2009	767.8	-17
20975	05-MAR-2006	191.9	3	37508	03-MAY-2009	-83	-5
21977	14-MAY-2006	-55.2	-5	38009	07-JUN-2009	191.8	5
22478	18-JUN-2006	120.4	-2	38510	12-JUL-2009	131.9	-12
22979	23-JUL-2006	744.3	-6	39011	16-AUG-2009	72.8	-5
23480	27-AUG-2006	664.4	-4	39512	20-SEP-2009	620	-4
23981	01-OCT-2006	-664.6	0	40013	25-OCT-2009	14.4	-8
24482	05-NOV-2006	-546.8	-3				

Bibliography

Adam, N., B. M. Kampes, and M. Eineder (2004). Development of a scientific persistent scatterer system: Modifications for mixed ERS/ENVISAT time series. In *ENVISAT & ERS Symposium, Salzburg, Austria, 6–10 September, 2004*, pp. 9.

Amiri-Simkooei, A. R. (2007). *Least-Squares Variance Component Estimation. Theory and GPS applications*. Ph. D. thesis, Delft University of Technology, Delft, the Netherlands.

Anderson, E. M. (1936). The dynamics of the formation of cone-sheets, ring-dykes, and caldron subsidence. *Proceedings of the Royal Society of Edinburgh 56*, 128–157.

Bähr, H. and R. Hanssen (2010). Network adjustment of orbit errors in sar interferometry. In *Advances in the Science and Applications of SAR Interferometry, 'FRINGE09', Frascati, Italy, 30 Nov-4 Dec 2009*, pp. 8 pp.

van Balen, R. T., R. Houtgast, and S. A. P. L. Cloetingh (2005). Neotectonics of the Netherlands: a review. *Quaternary Science Reviews 24*, 439–454.

Bamler, R. and R. Hanssen (1997). Decorrelation induced by interpolation errors in InSAR processing. In *International Geoscience and Remote Sensing Symposium, Singapore, 3–8 Aug 1997*, pp. 1710–1712.

Bamler, R. and P. Hartl (1998). Synthetic aperture radar interferometry. *Inverse Problems 14*, R1–R54.

Bamler, R. and H. Runge (1991). PRF-ambiguity resolving by wavelength diversity. *IEEE Transactions on Geoscience and Remote Sensing 29*(6), 997–1003.

Bayera, P., E. Duranb, R. Baumannc, and M. Finkelb (2009). Optimized groundwater drawdown in a subsiding urban mining area. *Journal of Hydrology 365*(1-2), 95–104.

Bekendam, R. F. and J. J. Pöttgens (1995). Ground movements over the coal mines in southern Limburg, The Netherlands and their relation to rising mine waters. In A. I. Johnson (Ed.), *Proceedings of the fifth international symposium on land subsidence (FISOLS'95), The Hague, The Netherlands, 16–20 Oct 1995*, Rotterdam, pp. 3–12. Balkema.

Bell, J. W., F. Amelung, A. Ferretti, M. Bianchi, and F. Novali (2008). Permanent scatterer InSAR reveals seasonal and long-term aquifer-system response to groundwater pumping and artificial recharge. *WATER RESOURCES RESEARCH 44*, W02407.1–W02407.18.

Bense, V. F. (2004). *The hydraulic properties of faults in unconsolidated sediments and their impact on groundwater ow a study in the Roer Valley Rift System and adjacent areas in the Lower Rhine Embayment*. Ph. D. thesis, Vrije Universiteit Amsterdam, Amsterdam, the Netherlands.

Bense, V. F., R. T. van Balen, and J. J. de Vries (2003). The impact of faults on the hydrogeological conditions in the Roer Valley Rift System: an overview. *Netherlands Journal of Geosciences / Geologie en Mijnbouw 82 (1)*, 41–54.

Berardino, P., G. Fornaro, R. Lanari, and E. Sansosti (2002). A new algorithm for surface

deformation monitoring based on small baseline differential SAR interferograms. *IEEE Transactions on Geoscience and Remote Sensing 40*(11), 2375–2383.

Bergen, F. van., H. J. M. Pagnier, and P. C. H. van Tongeren (2007). Peat, coal and coalbed methane. In T. E. Wong, D. A. J. Batjes, and J. de Jager (Eds.), *Geology of the Netherlands*, pp. 265–282. Amsterdam: Royal Netherlands Academy of Arts and Sciences.

van den Berg, M., W. Groenewoud, G. Lorenz, P. Lubbers, D. Brus, and S. Kroonenberg (1994). Patterns and velocities of recent crustal movements in the Dutch part of the Roer Valley rift system. *Geologie en Mijnbouw 73*, 157–168.

Biggs, J., T. Wright, Z. Lu, and B. Parsons (2007). Multi-interferogram method for measuring interseismic deformation:Denali Fault, Alaska. *Geophysical Journal International 170*, 1165–1179.

Blodgett, S. and J. R. Kuipers (2002). Underground hard-rock mining: Subsidence and hydrologic environmental impacts. Technical report, Center for Science in Public Participation, Bozeman, MT, USA.

van Bracht, M. J. (2001). *Made to measure: Information requirements and groundwater level monitoring networks*. Ph. D. thesis, Vrije Universiteit Amsterdam, Amsterdam, The Netherlands.

Calais, E., N. d'Oreye, J. Albaric, A. Deschamps, D. Delvaux, J. Déverchère, C. Ebinger, R. W. Ferdinand, F. Kervyn, A. S. Macheyeki, A. Oyen, J. Perrot, E. Saria, B. Smets, D. S. Stamps, and C. Wauthier (2008). Strain accomodation by slow slip and dyking in a youthful continental rift, East Africa. *Nature 456*(doi:10.1038/nature07478), 783–788.

Camelbeeck, T., M. van Camp, D. Jongmans, O. Francis, and T. van Dam (2002). Comment on nature of the recent vertical ground movements inferred from high-precision leveling data in an intraplate setting: Ne Ardenne, Belgium by A. Demoulin and A. Collignon. *Journal of Geophysical Research 107(B11)*, 2281.

Camelbeeck, T., K. Vanneste, P. Alexandre, K. Verbeeck, T. Petermans, P. Rosset, M. Everaerts, R. Warnant, , and M. van Camp (2007). Relevance of active faulting and seismicity studies to assessments of long-term earthquake activity and maximum magnitude in intraplate northwest Europe, between the Lower Rhine Embayment and the North Sea. *(Special papers) Geological Society of America 425*, 193–224.

Caro Cuenca, M. and R. Hanssen (2008). Subsidence due to peat decomposition in the Netherlands, kinematic observations from radar interferometry. In *Fifth International Workshop on ERS/Envisat SAR Interferometry, 'FRINGE07', Frascati, Italy, 26 Nov-30 Nov 2007*, pp. 6 pp.

Caro Cuenca, M. and R. Hanssen (2011). Radar time series analysis applied to study surface motion in the abandoned coal mines of Wassenberg. In *GeoMonitoring11*.

Caro Cuenca, M., A. J. Hooper, and R. F. Hanssen (2011). A new method for temporal phase unwrapping of persistent scatterers InSAR time series. *TGARS doi:10.1109/TGRS.2011.2143722*.

Caro Cuenca, M., A. J. Hooper, and R. F. Hanssen (2012). Surface deformation induced by water influx in the abandoned coal mines in Limburg, the Netherlands observed by satellite radar interferometry. *Journal of Applied Geophysics*.

Chen, C. W. (2001). *Statistical-cost network-flow approaches to two-dimensional phase unwrapping for radar interferometry*. Ph. D. thesis, Stanford University.

Chen, C. W. and H. A. Zebker (2000). Two-dimensional phase unwrapping using statistical models for cost functions in nonlinear optimization. *Journal of the Optical Society of America A. 18*, 338–351.

Cloetingh, S., T. Cornu, P. A. Ziegler, and F. Beekman (2006). Neotectonics and intraplate continental topography of the northern Alpine Foreland. *Earth-Science Reviews 74*, 127–

196.

Cloetingh, S., P. Ziegler, F. Beekman, P. Andriessen, L. Matenco, G. Bada, D. Garcia-Castellanos, N. Hardebol, P. Dèzes, and D. Sokoutis (2005). Lithospheric memory, state of stress and rheology: Neotectonic controls on Europe's intraplate continental topography. *Quaternary Science Reviews 24*(3-4), 241–304.

Colesanti, C., A. Ferretti, F. Novali, C. Prati, and F. Rocca (2003). SAR monitoring of progressive and seasonal ground deformation using the Permanent Scatterers Technique. *IEEE Transactions on Geoscience and Remote Sensing 41*(7), 1685–1701.

Costantini, M. (1998). A novel phase unwrapping method based on network programming. *IEEE Transactions on Geoscience and Remote Sensing 36*(3), 813–821.

Counselman, C. C. and S. A. Gourevitch (1981). Miniature interferometer terminals for earth surveying: ambiguity and multipath with the Global Positioning System. *IEEE Transactions on Geoscience and Remote Sensing 19*(4), 244–252.

Crosetto, M., O. Monserrat, C. Bremmer, R. Hanssen, R. Capes, and S. Marsh (2008). Ground motion monitoring using SAR interferometry: Quality assessment. *European Geologist submitted*, 7.

Crosetto, M., O. Monserrat, M. Cuevas, and B. Crippa (2011). Spaceborne differential sar interferometry: Data analysis tools for deformation measurement. *Remote Sensing 3*(2), 305–318.

Cumming, I. and F. Wong (2005). *Digital Processing Of Synthetic Aperture Radar Data: Algorithms And Implementation*. New York: Artech House Publishers. ISBN 1580530583.

De Zan, F. and F. Rocca (2005). Coherent processing of long series of SAR images. In *International Geoscience and Remote Sensing Symposium, Seoul, Korea, 25–29 July 2005*.

Dehghani, M., M. J. V. Zoej, I. Entezam, A. Mansourian, and S. Saatchi (2009). InSAR monitoring of progressive land subsidence in Neyshabour, northeast Iran. *Geophysical Journal International 178*, 47–56.

Demoulin, A. (2006). Slip rate and mode of the Feldbiss normal fault (Roer Valley Graben) after removal of groundwater effects. *Earth and Planetary Science Letters 245*, 630–641.

Devleeschouwer, X., P. Y. Declercq, M. Dusar, and A. Debien (2008). Contrasting ground movements revealed by radar interferometry over abandoned coal mines (Campine, Belgium). In *Fifth International Workshop on ERS/Envisat SAR Interferometry, 'FRINGE07', Frascati, Italy, 26 Nov-30 Nov 2007*, pp. 8 pp.

Dezes, P., S. M. Schmid, and P. A. Ziegler (2004). Evolution of the European Cenozoic Rift System: Interaction of the Alpine and Pyrenean orogens with their foreland lithosphere. *Tectonophysics 389*, 1–33.

Donnelly, L. J. (2000). Reactivation of geological faults during mining subsidence from 1859 to 2000 and beyond. *Transactions of the Institution of Mining and Metallurgy section A, 109*(3), 179–190.

Donnelly, L. J. and J. G. Rees (2001). Tectonic and mining induced fault reactivation around Barlaston on the Midlands Microcraton, North Staffordshire, UK. *QJEGH 34*(2), 195–214.

van Eck, T., L. Ahorner, and H. Paulssen (1993). The earthquake of the century in northwestern Europe: The Roermond, the Netherlands, earthquake of April 13, 1992. *Earthquakes and Volcanoes 24*(1), 15–26.

Eineder, M. and N. Adam (2005). A maximum-likelihood estimator to simultaneously unwrap, geocode, and fuse SAR interferograms from different viewing geometries into one digital elevation model. *IEEE Transactions on Geoscience and Remote Sensing 43*(1), 24–36.

Farr, T. G., P. A. Rosen, E. Caro, R. Crippen, R. Duren, S. Hensley, M. Kobrick, M. Paller,

E. Rodriguez, L. Roth, D. Seal, S. Shaffer, J. Shimada, J. Umland, M. Werner, M. Oskin, D. Burbank, and D. Alsdorf (2007). The shuttle radar topography mission. *Rev. Geophys. 45*, 33.

Ferretti, A., A. Fumagalli, F. Novali, C. Prati, F. Rocca, and A. Rucci (2011). A new algorithm for processing interferometric data-stacks: SqueeSAR. *IEEE Transactions on Geoscience and Remote Sensing 0196-2892*, 1–11.

Ferretti, A., C. Prati, and F. Rocca (1999). Monitoring terrain deformations using multitemporal SAR images. In *CEOS SAR Workshop, ESA-CNES, Toulouse, France, 26-29 October 1999*, pp. 4 pp.

Ferretti, A., C. Prati, and F. Rocca (2000). Nonlinear subsidence rate estimation using permanent scatterers in differential SAR interferometry. *IEEE Transactions on Geoscience and Remote Sensing 38*(5), 2202–2212.

Ferretti, A., C. Prati, and F. Rocca (2001). Permanent scatterers in SAR interferometry. *IEEE Transactions on Geoscience and Remote Sensing 39*(1), 8–20.

Fialko, Y., D. Sandwell, M. Simons, and P. Rosen (2005). Three-dimensional deformation caused by the Bam, Iran, earthquake and the origin of shallow slip deficit. *Nature 435*, 295–299.

Fisher, R. A. (1925). Applications of Student's distribution. *Metron 5*, 90–104.

Gabriel, A. K. and R. M. Goldstein (1988). Crossed orbit interferometry: theory and experimental results from SIR-B. *Int.J. Remote Sensing 9*(5), 857–872.

Geertsma, J. (1973). A basic theory of subsidence due to reservoir compaction: the homogeneous case. *Verhandelingen van het Koninklijk Nederlands geologisch mijnbouwkundig Genootschap 28*, 43–62.

Geertsma, J. and G. van Opstal (1973). A numerical technique for predicting subsidence above compacting reservoirs, based on the nucleus of strain concept. *Verhandelingen van het Koninklijk Nederlands geologisch mijnbouwkundig Genootschap 28*, 63–78.

Geluk, M. C., E. J. T. Duin, M. Dusar, R. H. B. Rijkers, M. W. van den Berg, and P. van Rooijen (1994). Stratigraphy and tectonics of the roer valley graben. *Geologie en Mijnbouw 73*, 129–141.

Ghiglia, D. C. and M. D. Pritt (1998). *Two-dimensional phase unwrapping: theory, algorithms, and software*. New York: John Wiley & Sons, Inc.

Goel, K. and N. Adam (2011). Deformation estimation in non-urban areas exploiting high resolution sar data. In *Advances in the Science and Applications of SAR Interferometry, 'FRINGE11', Frascati, Italy, 19-23 Sep 2011.*

Goldstein, R. M., H. A. Zebker, and C. L. Werner (1988). Satellite radar interferometry: Two-dimensional phase unwrapping. *Radio Science 23*(4), 713–720.

Gölke, M., S. Cloetingh, and D. Coblentz (1996). Modelling of stress patterns along the mid-Norwegian continental margin, 62 to 68 n. *Tectonophysics 266*, 33–53.

González, P. J. and J. Fernandéz (2011). Error estimation in multitemporal InSAR deformation time series, with application to Lanzarote, Canary Islands. *Journal of Geophysical Research 116*, B10404.

Groenewoud, W., G. K. Lorenz, F. J. J. Brouwer, and R. E. Molendijk (1991). Geodetic determination of recent land subsidence in The Netherlands. In A. I. Johnson (Ed.), *Land subsidence; proceedings of the fourth international symposium on land subsidence*, pp. 463–471. IAHS Publ. no. 200.

Hanssen, R. and R. Bamler (1999). Evaluation of interpolation kernels for SAR interferometry. *IEEE Transactions on Geoscience and Remote Sensing 37*(1), 318–321.

Hanssen, R. F. (2001). *Radar Interferometry: Data Interpretation and Error Analysis*. Dordrecht: Kluwer Academic Publishers.

Heitfeld, K. H., M. Heitfeld, P. Rosner, H. Sahl, and K. Schetelig (2002). Mine water

recovery in the coal mining district of aachen impacts and measures to control potential risk. In *Uranium in the Aquatic Environment. Heidelberg (Springer)*, pp. 1027–1036.

Heitfeld, M., M. Mainz, and M. M. H. Schetelig (2006). Ground heave induced by mine water recovery. In *Eurock 2006: multiphysics coupling and long term behaviour in rock mechanics*, pp. 315–320.

Heitfeld, M., P. Rosner, and J. Boger (2007). Metingen mijnwaterstand 1994-2009 (mine water measurements 1994-2009, in dutch). Technical report, Ingenieurbüro Heitfeld-Schetelig GmbH (IHS).

Herrmann, F., C. Jahnke, F. Jenn, R. Kunkel, H. Voigt, J. Voigt, and F. Wendland (2009). Groundwater recharge rates for regional groundwater modelling: a case study using GROWA in the Lower Rhine lignite mining area, germany. *Hydrogeology Journal 17*(8), 2049–2060.

Hoffmann, J. (2003). *The application of satellite radar interferometry to the study of land subsidence over developped aquifer systems*. Ph. D. thesis, Stanford University.

Hooper, A. (2006). *Persistent Scatterer Radar Interferometry for Crustal Deformation Studies and Modeling of Volcanic Deformation*. Ph. D. thesis, Stanford University.

Hooper, A. (2008). A multi-temporal InSAR method incorporating both persistent scatterer and small baseline approaches. *Geophysical Research Letters 35*, L16302.

Hooper, A. (2010). A Statistical-Cost approach to unwrapping the phase of InSAR time series. In *Advances in the Science and Applications of SAR Interferometry, 'FRINGE09', Frascati, Italy, 30 Nov-4 Dec 2009*, pp. 6 pp.

Hooper, A., P. Segall, and H. Zebker (2007). Persistent scatterer interferometric synthetic aperture radar for crustal deformation analysis, with application to Volcan Alcedo, Galapagos. *Journal of Geophysical Research 112*, B07407.

Hooper, A. and H. Zebker (2007). Phase unwrapping in three dimensions with application to InSAR time series. *Journal of the Optical Society of America A. 24*, 2737–2747.

Hooper, A., H. Zebker, P. Segall, and B. Kampes (2004, December). A new method for measuring deformation on volcanoes and other non-urban areas using InSAR persistent scatterers. *Geophysical Research Letters 31*, L23611, doi:10.1029/2004GL021737.

Houtgast, R. F. and R. T. van Balen (2000). Neotectonics of the Roer Valley Rift System, the Netherlands. *Global and Planetary Change 27*, 131–146.

Houtgast, R. F., R. T. van Balen, and C. Kasse (2005). Late quaternary evolution of the Feldbiss fault(Roer Valley Rift System, The Netherlands) based on trenching, and its potential relation to glacial unloading. *Quaternary Science Reviews 24*, 489–508.

Houtgast, R. F., R. T. van Balen, C. Kasse, and J. Vandenberghe (2003). Late quaternary evolution and postseismic near surface fault displacements along the Geleen fault (Feldbiss Fault Zone-Roer Valley Rift System, The Netherlands) based on trenching. *Geologie en Mijnbouw 82(2)*, 177–196.

Just, D. and R. Bamler (1994). Phase statistics of interferograms with applications to synthetic aperture radar. *Applied Optics 33*(20), 4361–4368.

Kampes, B. M. (2006). *Radar Interferometry: Persistent Scatterer Technique*. Remote Sensing and Digital Image Processing, vol.12. Dordrecht: Springer Verlag.

Kampes, B. M. and R. F. Hanssen (2004). Ambiguity resolution for permanent scatterer interferometry. *IEEE Transactions on Geoscience and Remote Sensing 42*(11), 2446–2453.

Kampes, B. M., R. F. Hanssen, and Z. Perski (2003). Radar interferometry with public domain tools. In *Third International Workshop on ERS SAR Interferometry, 'FRINGE03', Frascati, Italy, 1-5 Dec 2003*, pp. 6 pp.

Kampes, B. M., R. F. Hanssen, F. van Leijen, and M. Arikan (2011). Delft object-oriented radar interferometric software user's manual and technical documentation. Technical

report, Delft University of Technology, Delft.

Ketelaar, V. B. H. (2009). *Satellite Radar Interferometry, Subsidence Monitoring Techniques*. Remote Sensing and Digital Image Processing, vol.14. Dordrecht: Springer Verlag.

KNMI (2010). Aardbevingen bij voerendaal en kunrade (2001).

Kooi, H., P. Johnston, K. Lambeck, C. Smither, and R. Molendijk (1998). Geological causes of recent ($\sim$ 100 yr) vertical land movement in the Netherlands. *Tectonophysics 299*, 297–316.

Kratzsch, H. (1983). *Mining subsidence engineering*. Berlin and New York: Springer-Verlag.

van Leijen, F. J. and R. F. Hanssen (2008). Ground water management and its consequences in Delft, the Netherlands as observed by persistent scatterer interferometry. In *Fifth International Workshop on ERS/Envisat SAR Interferometry, 'FRINGE07', Frascati, Italy, 26 Nov-30 Nov 2007*, pp. 6 pp.

van Leijen, F. J., R. F. Hanssen, P. S. Marinkovic, and B. M. Kampes (2006). Spatio-temporal phase unwrapping using integer least-squares. In *Fourth International Workshop on ERS/Envisat SAR Interferometry, 'FRINGE05', Frascati, Italy, 28 Nov-2 Dec 2005*, pp. 6 pp.

Lorenz, G. K., W. Groenewoud, F. Schokking, M. W. van den Berg, J. Wiersma, F. J. J. Brouwer, and S. Jelgersma (1991). Interim-rapport over het onderzoek naar bodembeweging in Nederland. Technical report, Rijks Geologische Dienst, Ministerie van Verkeer en Waterstaat, Rijkswaterstaat, Meetkundige Dienst en Directie Noordzee.

Marinkovic, P., G. Ketelaar, F. J. van Leijen, and R. F. Hanssen (2008). InSAR quality control: Analysis of five years of corner reflector time series. In *Fifth International Workshop on ERS/Envisat SAR Interferometry, 'FRINGE07', Frascati, Italy, 26 Nov-30 Nov 2007*, pp. 8 pp.

Massonnet, D., K. Feigl, M. Rossi, and F. Adragna (1994). Radar interferometric mapping of deformation in the year after the Landers earthquake. *Nature 369*, 227–230.

Massonnet, D. and K. L. Feigl (1998). Radar interferometry and its application to changes in the earth's surface. *Reviews of Geophysics 36*(4), 441–500.

Mattar, K. E., P. W. Vachon, D. Geudtner, A. L. Gray, I. G. Cumming, and M. Brugman (1998). Validation of Alpine glacier velocity measurements using ERS tandem-mission SAR data. *IEEE Transactions on Geoscience and Remote Sensing 36*(3), 974–984.

Messing, F. A. M. (1988). *De Mijnsluiting in Limburg*. Leiden, the Netherlands: Martinus Nijhoff.

Michon, L. and R. T. van Balen (2005). Characterization and quantification of active faulting in the Roer valley rift system based on high precision digital elevation models. *Quaternary Science Reviews 24*, 455–472.

Michon, L., R. T. van Balen, O. Merle, and H. Pagnier (2003). The cenozoic evolution of the roer valley rift system integrated at a european scale. *Tectonophysics 367*, 101–126.

Mogi, K. (1958). Relations between eruptions of various volcanoes and the deformations of the ground surfaces around them. *Bulletin of the Earthquake Research Institute, University of Tokyo 36*, 99–134.

Mora, O., R. Lanari, J. J. Mallorqui, P. Berardino, and E. Sansosti (2002). A new algorithm for monitoring localized deformation phenomena based on small baseline differential SAR interferograms. pp. 1327–1239.

Moreira, A., G. Krieger, I. Hajnsek, S. Riegger, E. Settelmeyer, D. Hounam, and M. Werner (2004). Tandem-x: A terrasar-x add-on satellite for single-pass sar interferometry. In *International Geoscience and Remote Sensing Symposium, Anchorage, Alaska, 20–24 September 2004*.

Nitti, D. O., R. F. Hanssen, A. Rece, F. Bovenga, and R. Nutricato (2010). Impact of

dem-assisted coregistration on high-resolution sar interferometry. *IEEE Transactions on Geoscience and Remote Sensing* (10.1109/TGRS.2010.2074204).

Odijk, D. (2002). *Fast precise GPS positioning in the presence of ionospheric delays*. Ph. D. thesis, Delft University of Technology.

Paganelli, F. and A. Hooper (2008). Deformation at Fogo volcano, Cape Verde, detected by persistent scatterer InSAR. *EGU General Assembly 2008, Vienna 10*, EGU2008–A–07819.

Perissin, D. (2006). *SAR super-resolution and characterization of urban targets*. Ph. D. thesis, Politecnico di Milano, Italy.

Perissin, D. and C. Prati (2008). Comparison between sar atmospheric phase screens at 30 by means of ers and envisat data. In *International Geoscience and Remote Sensing Symposium, Boston MA, USA, 6–11 July 2008*.

Perissin, D. and F. Rocca (2006). High accuracy urban DEM using permanent scatterers. *IEEE Transactions on Geoscience and Remote Sensing 44*(11), 3338–3347.

Perski, Z., R. Hanssen, A. Wojcik, and T. Wojciechowski (2009). InSAR analysis of terrain deformation near the Wieliczka salt mine, Poland. *Engineering Geology 106*(doi:10.1016/j.enggeo.2009.02.014), 58–67.

Pöttgens, J. J. E. (1985). Bodemhebung durch ansteigendes Grubenwasser. In *The Development Science and Art of Minerals Surveying, Proceedings VIth International Congress, International Society for Mine Surveying, Harrogate, United Kingdom*, Volume 2, pp. 928–938.

Prati, C. and F. Rocca (1990). Limits to the resolution of elevation maps from stereo SAR images. *Int. J. Remote Sensing 11*(12), 2215–2235.

Puysségur, B., R. Michel, and J. P. Avouac (2007). Tropospheric phase delay in InSAR estimated from meteorological model and multispectral imagery. *Journal of Geophysical Research in press*.

Rietveld, H. (1984). Land subsidence in the netherlands. In *Third International Symposium on Land Subsidence, Venice*.

Rijkswaterstaat, D. I. D. (2011). nlhist.out (historical leveling data of the Netherlands).

Rosner, P. (2011). *Der Grubenwasseranstieg im Aachener und Sdlimburger Steinkohlenrevier. Eine hydrogeologisch-bergbauliche Analyse der Wirkungszusammenhnge*. Ph. D. thesis, Germany.

Samiei-Esfahany, S. (2008). Improving persistent scatterer interferometry for deformation monitoring; (case study on the Gardanne mining site). Master's thesis, Delft University of Technology.

Samson, J. (1996). Coregistration in SAR interferometry. Master's thesis, Faculty of Geodetic Engineering, Delft University of Technology.

Scharroo, R. and P. Visser (1998). Precise orbit determination and gravity field improvement for the ERS satellites. *Journal of Geophysical Research 103*(C4), 8113–8127.

Schunert, A., M. Even, U. Srgel, and K. Schulz (2010). Detection of localized surface deformation using a modified stamps algorithm. In *Advances in the Science and Applications of SAR Interferometry, 'FRINGE09', Frascati, Italy, 30 Nov-4 Dec 2009*, pp. 6 pp.

Segall, P., J.-R. Grasso, and A. Mossop (1994). Poroelastic stressing and induced seismicity near Lacq gas field, southwestern France. *Journal of Geophysical Research 99*(B8), 15423–15438.

SoDM (2007). Monitoring waterstanden in mijnschachten (internal report). Technical report, Staatstoezicht Op De Mijnen (Dutch: State Supervision of Mines), The Netherlands.

Stimson, G. (1998). *Introduction to Airborne Radar, 2nd Edition (IEE Radar Series)*. Raleigh: SciTech Publishing Inc. ISBN 1891121014.

Sturkell, E., P. Einarsson, F. Sigmundsson, A. Hooper, B. G. Ofeigsson, H. Geirsson, and H. Olafsson (2010). Katla and Eyjafjallajkull volcanoes. *Developments in Quaternary Science 13*, 5–21.

Talebian, M., E. J. Fielding, G. J. Funning, M. Ghorashi, J. Jackson, H. Nazari, B. Parsons, K. Priestley, P. A. Rosen, R. Walker, and T. J. Wright (2004). The 2003 Bam (Iran) earthquake - rupture of a blind strike-slip fault. *Geophysical Research Letters 31*.

Teunissen, P. J. G. (1988). *Towards a Least-Squares Framework for Adjusting and Testing of both Functional and Stochastic Models*, Volume 26 of *Mathematical Geodesy and Positioning series*.

Teunissen, P. J. G. (1994). Least-squares estimation of the integer GPS ambiguities. In *Publications and annual report 1993*, Number 6 in LGR-Series, pp. 59–74. Delft geodetic computing centre.

Teunissen, P. J. G. (2000a). *Adjustment theory; an introduction* (1 ed.). Delft: Delft University Press.

Teunissen, P. J. G. (2000b). *Testing theory; an introduction* (1 ed.). Delft: Delft University Press.

Teunissen, P. J. G. (2006). On InSAR ambiguity resolution for deformation monitoring. *Artificial Satellites 41*(1), 17–22.

Teunissen, P. J. G., P. J. de Jonge, and C. C. J. M. Tiberius (1995a). The LAMBDA-method for fast GPS processing. In *GPS Technology Applications, Bucharest, Romania, Sep 26-29*.

Teunissen, P. J. G., P. J. de Jonge, and C. C. J. M. Tiberius (1995b). A new way to fix carrier-phase ambiguities. *GPS World*, 58–61.

Teunissen, P. J. G. and C. C. J. M. Tiberius (1994). Integer least-squares estimation of the GPS phase ambiguities. In *International Symposium on Kinematic Systems in Geodesy, Geomatics and Navigation, Banff, Alberta, Canada, Aug 30 – Sept 2, 1994*.

TNO (1999). *Geological Atlas of the Subsurface of The Netherlands, Map Sheet XV, Sittard-Maastricht,Netherlands Institute of Applied Science*. National Geological Survey, Utrecht: TNO.

TNO (2010). Dinoloket. Website: http://www.dinoloket.nl/.

van Tongeren, P. C. H. and R. Dreesen (2004). Residual space volumes in abandoned coal mines of the Belgian Campine basin and possibilities for use. *Geologica Belgica 7*(3-4), 157–164.

Usai, S. (1997). The use of man-made features for long time scale insar. In *International Geoscience and Remote Sensing Symposium, Singapore, 3–8 Aug 1997*, pp. 1542–1544.

Usai, S. (2001). *A New Approach for Long Term Monitoring of Deformations by Differential SAR Interferometry*. Ph. D. thesis, Delft University of Technology.

Usai, S. and R. F. Hanssen (1997). Long time scale insar by means of high coherence features. In *Third ERS Symposium-Space at the Service of our Environment, Florence, Italy*, pp. 225–228.

Vanneste, K. and K. Verbeeck (2001). Paleoseismological analysis of the Rurrand fault near Jlich, Roer Valley graben, Germany: Coseismic or aseismic faulting history? *Netherlands Journal of Geosciences / Geologie en Mijnbouw 80*, 159–169.

Vanneste, K., K. Verbeeck, T. Camelbeeck, E. Paulissen, M. Meghraoui, F. Renardy, D. Jongmans, and M. Frechen (2001). Surface-rupturing history of the Bree fault scarp, Roer Valley graben: Evidence for six events since the late Pleistocene. *Journal of Seismology 5*, 329–359.

Wackernagel, H. (1995). *Multivariate Geostatistics: An Introduction with Applications*. Berlin: Springer-Verlag.

Westen, J. M. J. (1971). Statistisch overzicht van productie, bezetting en prestaties van de

Limburgse steenkolenmijnen. *Geologie en Mijnbouw 50*, 311–320.

Wings, R. (2006). Aktuelle Entwicklungen im niederlndischen Altbergbau aus Sicht der Staatstoezicht op de Mijnen. In *Altbergbau-Kolloquium, Aachen, Germany*, pp. 49–58.

Wolkersdorfer, C. (2008). *Water Management at Abandoned Flooded Underground Mines Fundamentals, Tracer Tests, Modelling, Water Treatment*. Frankfurt am Main, Germany: Springer Berlin Heidelberg.

Wright, T., E. Fielding, and B. Parsons (2001). Triggered slip: observations of the 17 August 1999 Izmit (Turkey) earthquake using radar interferometry. *Geophysical Research Letters 28*(6), 1079–1082.

Yue, H., G. Liu, R. Hanssen, R. Wang, and X. Zhong (2008). Coal mine land subsidence monitoring using spaceborne InSAR data; a case study in Fengfeng, Hebei province, China. *International Journal of Remote Sensing submitted*, 14.

Zebker, H. A. and J. Villasenor (1992). Decorrelation in interferometric radar echoes. *IEEE Transactions on Geoscience and Remote Sensing 30*(5), 950–959.

Ziegler, P. A. (1992). European cenozoic rift system. *Tectonophysics 208*, 91–111.

Zijerveld, L., R. Stephenson, S. Cloetingh, E. Duin, and M. Van den Berg (1992). Subsidence analysis and modelling of the Roer Valley Graben (SE Netherlands). *Tectonophysics 208*(1-3), 159–171.

About the Author

Miguel Caro Cuenca was born in Seville (Spain) December 31st 1975. He studied Fundamental Physics in the University of Granada (1993-1999) and Physics with Computing in Edinburgh Napier University, (1999-2000). From 2000 to 2001, he did his MSc in Microwave Communications in the University of Portmouth, England. In 2002 he worked as a developer in France Telecom Formation in Paris. He joined Thales Nederland in 2004 until 2006 where he worked as researcher under the Marie Curie programme. During 2006-2011 he worked on his PhD in Radar Interferometry (InSAR) in the Delft University of Technology (TUDelft). This thesis covers his PhD study. In 2011-2012 he worked as researcher on the combination of InSAR and other geodetic techniques to measure displacements in the whole of the Netherlands, also for TUDelft. Currently he occupies a position as researcher at the Netherlands Organisation for Applied Scientific Research (TNO).

Index

$B_{\parallel}$, 26
$B_{\perp}$, 27
atmospheric delay
    ionosphere, 29
    long wavelength, 29
    short wavelength, 30
    vertical stratification, 30

ambiguity cycle, 43
atmospheric delay, 29
atmospheric phase screen, 39

Bam earthquake, 27
baseline, 26
    parallel, 26
    perpendicular, 27
Bayes
    Bayesian inference, 54
    Bayesian phase unwrapping, 54, 61
    rule, 54
BLUE, 46, 73
bootstrap estimator, 46

Campine Block, 5
coherence, 31
coregistration, 23

decorrelation, 31
DePSI, 35
displacement vector, 27
distributed scatterer, 33
Doppler centroid, 29
Doppler frequency, 29
double differences, 37

ensemble coherence maximization, 43
Erkelenz coal district, 78, 80, 84, 93

fault reactivation, 21
Feldbiss Fault Zone, 5
final estimation, 40
first order network, 37–40

Garzweiler lignite mine, 80
Gaussian distribution, 55

height ambiguity, 27

indicator kriging , 56
InSAR, 23, 24, 29
    limitations, 32
interferogram, 24

LAMBDA, 44
lignite mines, 80, 83, 100
line-of-sight,satellite, 27
look angle, 26
Lower Rhine Graben, 7

Neotectonics, 5
noise, 31
    coregistration, 31
    interpolation, 32
    thermal, 31
normalized amplitude dispersion, 35

open pit lignite mines, *see* lignite mines
orbital errors, 29, 38
Overall Model Test, 47, 73

Peel Block, 5
Peel Boundary Fault Zone, 5
perpendicular baseline, 27
persistent scatterer, 33
    selection, 35
persistent scatterer interferometry, PSI, 33
phase unwrapping, 25, 38, 41
    temporal, 42
    Bayesian, 54
    spatio-temporal , 42
PS, *see* persistent scatterer

reference phase, 26
residual topography, 32
Roer Valley Graben, 5, 7
Roer Valley Rift System, 5, 7

SAR, 23
seasonal model, 78
second order network, 40, 47
side-lobes, 37, 41
signal to clutter ratio, SCR, 35
spatially correlated noise, 66
spatio-temporal consistency, 41
squint angle, 29, 31
STC, *see* spatio-temporal consistency
storage coefficient, 20, 112
strain source, 19
Student's test, 91
subpixel position, 28
surface displacements, 27
Synthetic Aperture Radar, *see* SAR

topographic phase, 26, 32

uniaxial compression coefficient, d_m , 20
Upper Rhine Graben, 7

variance

arc, 53
spatial, 50
variance component estimation, 37
VCE, *see* variance component estimation
Venlo Graben, 5

Walsum coal district, 80
water rebound, 18
wrapped phase, 25

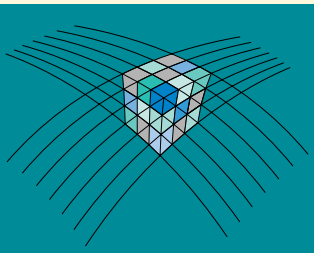

KONINKLIJKE NEDERLANDSE
AKADEMIE VAN WETENSCHAPPEN